UNIVERSITY OF SOUTHAMPTON

Automatic Detection and Analysis of Internal Waves on SAR Images

by

David Simonin

Submitted for the degree of Doctor of Philosophy

Faculty of Engineering, Science and Mathematics
School of Engineering Sciences
Aerospace Engineering

June 2005

UNIVERSITY OF SOUTHAMPTON

ABSTRACT

Faculty of Engineering, Science and Mathematics
School of Engineering Sciences

Aerospace Engineering

Doctor of Philosophy

Automatic Detection and Analysis of Internal Waves on SAR Images

by David Simonin

Internal waves features, like all mesoscale oceanographic features, are an important aspect of the ocean circulation. They are responsible for an important energy transfer mechanism, and have many implications in oceanographic engineering developments. Currently the extraction of internal waves information from satellite images is usually done from the human interpretation of the grey tone pattern visible in the images, which is a subjective, labour-intensive and time consuming task.

In this research a new method for the automatic detection of internal waves' signatures present in SAR images has been developed. The automatic detection technique uses two different approaches. One is based on wavelet transform and statistical texture descriptors. The classifications have been implemented using principal component analysis, the K-Nearest Neighbour technique and the multi-layer perceptron. The second approach is based on shape discrimination. The geometry, orientation and position of the different edges found within the image are used to distinguish the presence of internal waves. Along with a reduction in man power and analysis time, this new technique offers the means to analyse internal waves. Data sets of internal waves based on a number of criteria can easily be created. The users can then use the information to study the internal wave's dynamics or the internal wave conditions in a given place, which could be of value for offshore development.

The results of the research outlined in this thesis have demonstrated that the combination of either textural analysis with classifier or edge geometry analysis can provide the recognition and a primary analysis of internal wave signatures. This technique would therefore provides an appropriate starting point for the development of an operational recognition tool.

Table of Contents

List of Tables

List of Figures

Notations and abbreviations

Notations

$D(d, \theta)$	Inter-pixel deplacement with a orientation θ and a distance d
d	Distance of the inter-pixel deplacement
g	High-pass filter
h	Low-pass filter
I	Image intensity
k	nearest neighbour
M	Modulus
P	GLCM
(u, v)	Surface velocity
θ	Orientation of the inter-pixel deplacement
θ	Smooth function
ρ	Density
ψ	Wavelet

Abbreviations

CORR	Correlation
ENT	Entropy
GLCM	Gley level co-occurrence matrix
HOMOG	Local homogeneity
IW	Internal wave
NIW	Non-internal wave
PCA	Principal component analysis
STFT	Short time fourier transform
WT	Wavelet transform

Acknowledgements

This work would not have been possible without the continual assistance and support of many people. First and foremost, I thank my supervisors, Dr. Adrian Tatnall and Prof. Ian Robinson, for several years of advice, discussion and motivation. I am grateful for their dedication to the task of reading through the many drafts I have produced. Without their help, constant encouragement and support, this work would not have been possible.

I thank Dr Hugh Lewis for his assistance and valued help in the coding aspect of this work. I would especially like to thank Dr José Da Silva for his valuable suggestion and his interest in this research.

I would like to thank the staff and the students of the Aerospace Engineering Department for their support and friendship. Special thanks to Gareth, Steffen, George, Mark, Frank and to the french corner represented by Etienne and Jean-Baptiste.

Finally, I would like to thank and show my gratitude to Pascale for her encouragement, understanding, and determination to see this thesis completed.

Chapter 1

Introduction

Satellite technology and remote sensing technique have come a long way from the early launch in 1957 of Sputnik 1 and the early aerial photographs, with the first meteorological satellite TIROS 1 in 1960. Today they are commonplace. From the mid 70s the investment in satellite remote sensing of the earth's environment has grown very rapidly to become a significant commitment in space programs. The oceanography community had their share of this growth since 1978 when Seasat, the first satellite specifically designed for ocean observation, carried the first synthetic aperture radar (SAR).

1.1 Motivation and objectives of this study

Since these early days remote sensing has become a powerful tool for the oceanography community with a wide range of sensors onboard satellites. These sensors include multispectral instrumentation such as Seawifs, which measure the ocean colour giving information about the primary production, and thermal sensors such as AVHRR which provide us with the sea surface temperature. Microwave imaging radar such as the Synthetic Aperture Radar (SAR), which can measure sea roughness, are especially attractive because they operate independently of cloud cover, and solar illumination. The SAR measurement is predominantly due to scatter from gravity capillary and short gravity waves [1]. This first mission with Seasat produced surprising results. Along with widespread images of surface waves and swell, the SAR was able to provide the first remote-sensing information about oceanic internal waves.

Internal Waves, like all mesoscale oceanographic features, have a significant influence

[1] A wave disturbance in which buoyancy (or reduced gravity) acts as restoring force.

on ocean circulation. They are responsible for an important energy transfer mechanism. The identification and understanding of internal waves provides oceanographers with important information on dynamical processes occurring within the ocean. Furthermore internal Waves are an important factor to consider during the development of oceanographic engineering design. They are responsible for the deterioration of offshore platforms and can have a serious impact on acoustics propagation. For every one of the implications it is necessary to understand and model this phenomenon. However the modelling of the internal waves propagation is difficult, because of their non-linear nature and the large amount of information needed.

SAR images provide one of the best sources of information to study internal waves. However mainly due to data policy, processing costs, and manpower restrictions, only about 10% of the acquired images have ever been processed. Furthermore the information extraction from the data processed, is done by the interpretation of the grey tone patterns visible in the images, which is a very labour intensive and subjective task.

To date no automatic method for the recognition of oceanic features exists, therefore, the major novelty and the aim of the work lies in the automatic extraction and analysis of internal wave signature from SAR imagery. This research will focus in the creation an automatic recognition framework to move from a subjective manual detection of the internal wave toward a computed interpretation of the grey scale level of the images. Such detection will ease the work load as well as decrease the cost of the processing by reducing the manpower. The new framework will allow a classification of very large numbers of SAR scenes in order to identify possible internal waves signatures along with a means to infer primary information from such waves (i.e. period, type of signature, direction of propagation). The increase in information available from this new technique will be a valuable tool to increasing our understanding of internal waves, their importance in the oceanic circulation and better modelling and prediction applied to offshore developments.

1.2 The outline of the thesis

This chapter continues with a brief introduction on internal waves and their signature on SAR images. The amount of information available within internal waves and their

impact on offshore engineering will be discussed in the rest of this chapter. The second chapter will outline the difficulty, and consequently the strategy chosen, for the recognition task. This thesis continues with chapters three, four and five which look at the segmentation methods that were introduced in the second chapter as part of the strategy used. Chapter three describes the multi-resolution analysis designed to extract the internal wave signature. Then chapters four and five, look at the possibility of using the information inferred from the previous step in order to characterize the presence of the signature. Chapter six presents two classifications techniques. Finally chapter seven presents a discussion on the strategy and the accuracy of the detection tool is quantified.

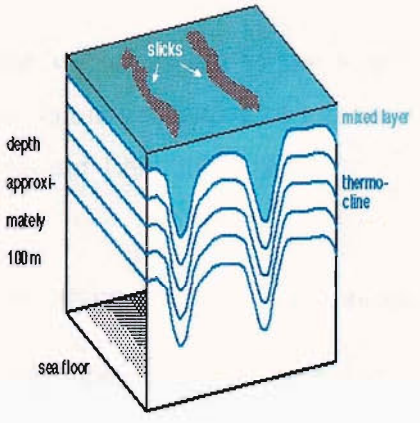

Figure 1.1: 3-D presentation of an internal wave [64]

1.3 Internal waves

Internal waves are progressive oscillations of constant density surface within a body of a stratified fluid (figure 1.1) with periods ranging from sub-inertial (i.e. less than the local Coriolis period) to the local buoyancy frequency (N). In the marine environment, they traditionally occur during the summer when the warm atmospheric conditions lead to a rise in the thermocline (figure 1.2). Many works discuss the generation of the internal waves, but it is commonly assumed that the internal waves present at the shelf sea are generated by baroclinic flow on the shelf break at each tidal cycle (eg: Fu 1984 [26] and Apel 1976 [3]) see Figure 1.3. Then the internal waves propagate mainly inshore as a group of rank order solitons and in some images with an inter-packet interval of 12.5h,

implying their tidal origin [4], [6].

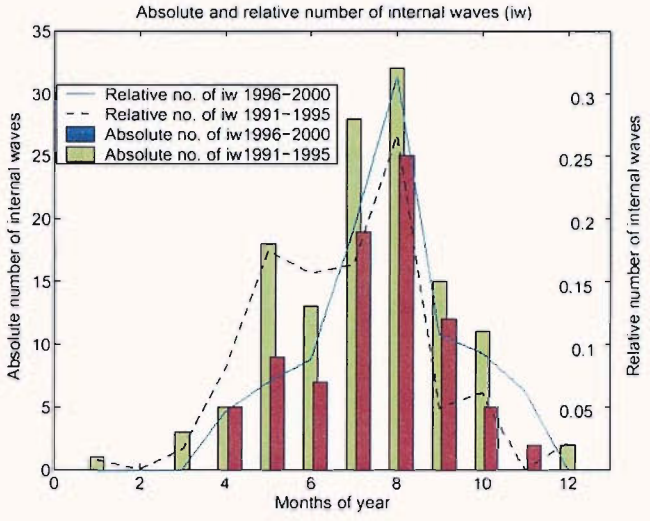

Figure 1.2: Absolute and relative (in respect to the acquired images) temporal distribution of internal waves. The annual variation of internal waves is exemplified for the two time periods of 1991-1995 and 1996-2000 [23].

The principal features of those internal waves can be summarized as [54]:

- The waves are found in groups or packets with 4 to 10 crests per group.
- The crests are often parallel to the bottom topography or radiate out as if they were coming from a point.
- One crest only may look like a shear in a SAR image; therefore an internal wave train is defined as several solitons moving in the same direction.
- The wavelength between crests is between several hundred metres and several kilometres, and usually decrease from the leading wave in a packet to the trailing edge.
- The crests are usually tens to hundred of kilometres long and decrease in length towards the rear of the wave group.
- These waves appear either as dark in a light background, as light in a dark background or as dark and light bands in the intermediate case. Dokken [23] found in his survey along the coast of Norway, that 60% of the signatures were bright in a dark background and 40% of the signature were dark in a bright background.

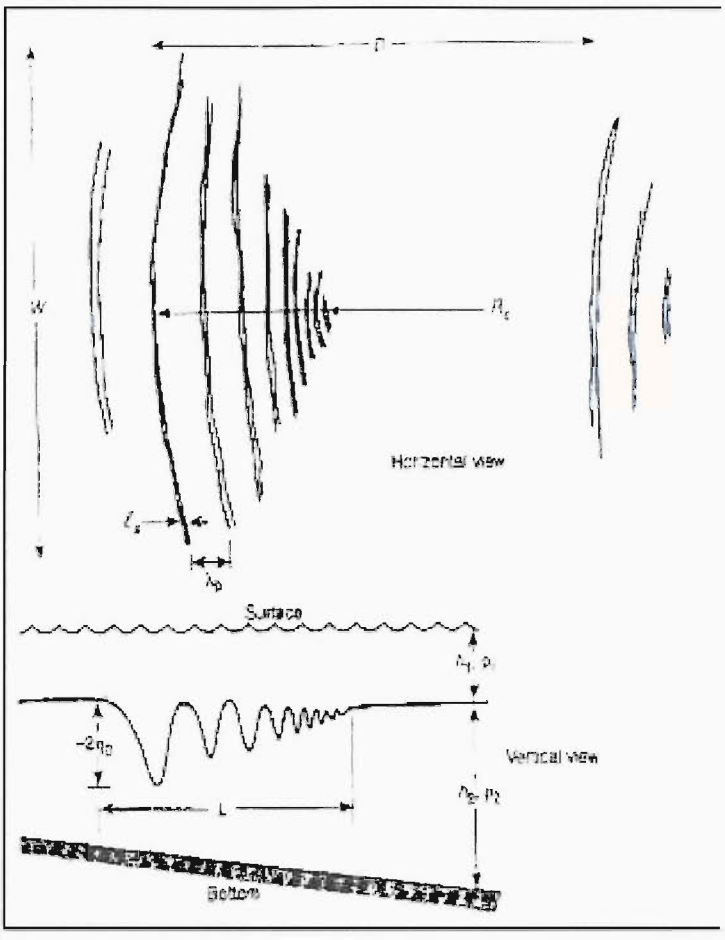

Figure 1.3: baroclinic dispersion [3]

1.3.1 Internal wave dynamics

Internal waves have frequencies that span the range from the maximum Brunt-Väisälä (buoyancy frequency) to the local Coriolis frequency of the water column. Internal waves arise as possible modes of oscillation in the presence of stratification, where the restoring force for the oscillation is provided by vertical density stratification. The motions of these waves can be derived from the momentum equation [2].

$$\frac{\delta u}{\delta t} - fv = -\frac{1}{\rho_0}\frac{\delta p'}{\delta x} \tag{1.3.1}$$

$$\frac{\delta v}{\delta t} + fv = -\frac{1}{\rho_0}\frac{\delta p'}{\delta y} \tag{1.3.2}$$

$$\frac{\delta w}{\delta t} = -\frac{1}{\rho_0}\frac{\delta p'}{\delta z} - \frac{\rho'}{\rho_0} \tag{1.3.3}$$

From equations 1.3.1 1.3.2 and 1.3.3 we can obtain a simple description of the motion of a stratified fluid [2].

$$\frac{\delta^2 w}{\delta^2 t} + N^2 w = -\frac{1}{\rho_0}\frac{\delta^2 p'}{\delta z \delta t} \qquad (1.3.4)$$
$$with \qquad N^2 = -\frac{g}{\rho^0}\frac{d\rho_0}{dz}$$

where w is the vertical velocity, g is the gravity acceleration ρ is constant density, and N(z) the Brunt-Vaisala frequency that represents the stratification in the ocean. The Brunt-Vaisala frequency is usually maximum for maximum mean density (ρ) gradient of the thermocline and decreases both above and below this level as the water becomes more homogeneous. If N^2 is assumed to be constant with a negligible earth rotation effect ($f = 0$) one can obtains an expression with w alone.

$$\frac{\delta^2}{\delta t^2}\left(\nabla^2 w\right) + N^2 \nabla_h^2 w = 0 \qquad (1.3.5)$$

where w is the amplitude of the vertical velocity and the subscript h indicates a gradient in the horizontal direction. The elementary modes of motion for small disturbances can be sought in the following form

$$w\left(x, z, t\right) = w(z)\exp^{i(kx-\sigma(k)t)} \qquad (1.3.6)$$

Where k is the horizontal wavenumber vector and n the frequency. $w(z)$ describes the mode structure and is subject to the boundary conditions at the surface ($z = 0$) and bottom ($z = h$). By substituting Eq.1.3.6 into Eq.1.3.5 one obtains the fundamental equation obeyed by $w(z)$ [51]

$$\frac{\delta^2 w(z)}{\delta z^2} + \left[\frac{N^2(z)}{\sigma^2} - 1\right] k^2 w(z) = 0 \qquad (1.3.7)$$
$$with \qquad N^2 = -\frac{g}{\rho^0}\frac{d\rho_0}{dz}$$
$$\sigma = \text{the internal wave frequency}$$

In the simple case of $N(z)$ is constant, Eq.1.3.7 represents the classic oscillator equation and its solution, satisfying the boundary conditions can be easily found to be

$$w(z) = A\sin\frac{n\pi}{h}z \qquad n = 1, 2, 3, ... \qquad (1.3.8)$$

where n is the mode order, A the amplitude and h the depth. From the above, the vertical velocities and displacements for the basic IW mode (n=1) has a maximum in the middle of the water column while for higher modes there will be several maxima

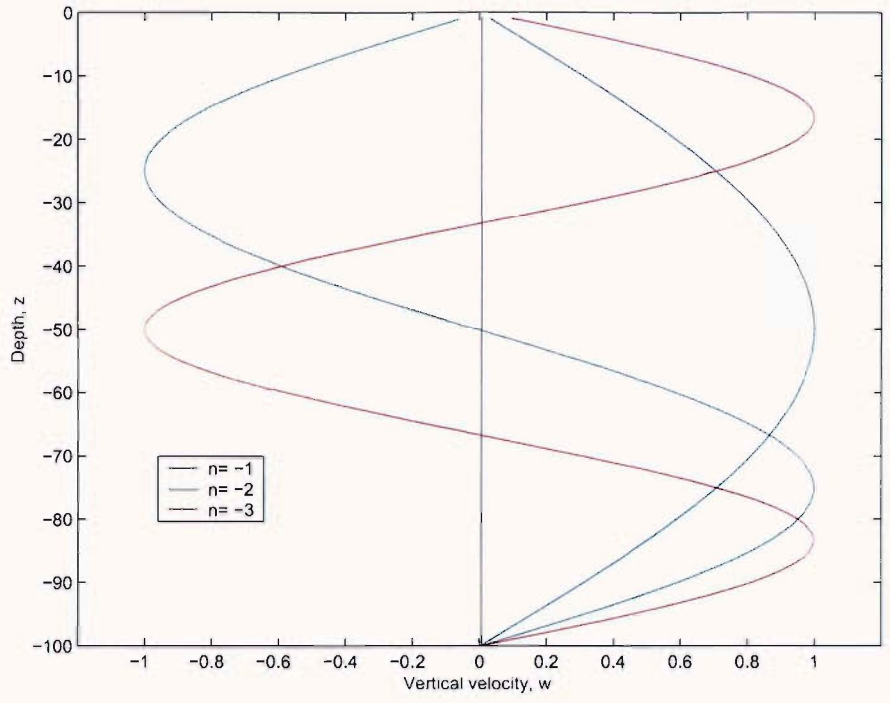

Figure 1.4: Distribution of vertical velocity w in the lower three internal wave modes for a constant N buoyancy profile

at different depths (see figure 1.4). In the general case $N = N(z)$, the mode structure is similar to that illustrated previously . Namely the maximum of the basic mode will correspond to the maximum of $N(z)$ and for higher order modes ($n > 1$) the number of maxima is equal to n (number of modes) with these being outside the thermocline. Non-linear IWs can propagate in the form of solitary waves, which can be described by the KdV[2] equation ([2] [48] [61]). The solution of the KdV equation [47] has the form of a pulse that results from the balance between non-linearity and dispersion. The vertical motion of tides forced by barotropic tidal flow over topography (e.g. a shelf break) leads to the displacement of the thermocline and consequently generates internal tidal waves (ITWs). These waves propagate away from the generation point along the thermocline and can be described by the KdV equation. Wavelengths are typically of 20-30km and the propagation is with tidal periodicity. It has been shown that short period internal solitary waves (ISWs) appear on profiles of ITWs with wavelengths 0.5-1Km.

[2]Kroteweg-de Vries

1.3.2 The importance of internal waves

Oceanography: The importance of internal waves is now being recognized a major phenomenon in a number of fields of oceanographic sciences and monitoring. The Meridional overturning circulation (MOC) is a vital element of the ocean circulation and a key indicator of climate change in models [42]. Theory and model of ocean circulation suggest that the MOC requires of the order of $2 \times 10^{12} W$ [44] [27] of power to intensely warm the abyss. Without this deep mixing, the ocean would turn in few a thousand years, into a basin of cold salty water. The water sinking at high latitude would cover the entire abysses without any mean to rise (via advection) again at low latitude. The mixing cannot really be the result of solar radiation as the ocean is an inefficient heat engine. Instead Monk and Wunsch [44] suggest that the mixing has to be the result of mechanical forces such as the tide and wind. The tidal energy is commonly assumed to mix the shallow ocean shelf, but part of this energy is dissipated in the form of internal tidal waves (1 TW). The mixing induced by the internal waves occurs in the form of turbulence away from the sea floor and in most cases as turbulence patches through scattering by topography. The vertical mixing induced by internal waves in regions of large topographic variation is believed to be an essential aspect in maintaining the ocean circulation [44]. However there is a lot of topography in the ocean (over half a million seamounts in the pacific alone) and very few measurements exist that can to explain the mechanisms involves and the real importance of internal wave in stirring the deep ocean.

In the upper layer, internal waves and the vertical mixing that they induce, when they propagate onto the continental shelf are vital for marine life. Large vertical displacements induces by such waves modulate the light available. The localised mixing of surface and subsurface masses can result in an intense shear with important consequences for the transport and dispersion of various ecosystem constituents within the water column (i.e. nutrient and heat) [33].

Offshore engineering: A large part of offshore oil and gas fields are in deep water, which involve cables, long and fragile structures such as the riser pipes and drill columns. They are therefore vulnerable to internal waves in many ways. Internal waves usually concentrate their energy into packet which arrive roughly twice a day (tide generated). The danger of such bursts of energy is that they can create horizontal motions near the

surface applying load directly to the platform itself. The safety and the structural integrity of the structure can be compromised if the design did not account for such forces. The vertical motions induced by the internal waves could create additional problems: the different risers and cable which connect the sea bed to the platform are subject to the bending moments induced by the wave. It has been reported that an internal wave packet was responsible for displacing oil platforms as much as 200 metres in the horizontal direction and 10 metres in the vertical direction. It therefore not surprising to learn that internal waves are cited in the design guidelines of the Department of Energy (1990) as a potential source of difficulty for deep-water operations.

The implications extend as far as the submarine community. Internal waves have serious impact on acoustics propagation. Just as the atmosphere turbulence can make stars to twinkle, so variation in the ocean structure cause fluctuations in sound propagation. The main causes of these fluctuations are internal waves when operating with typical sonar frequency. The internal waves can in extreme events even prevent a signal from being detected. Clearly this is of a great interest for the naval and submarine communities. Speculations on the loss of the USS thresher in 1969 have suggested that the prime suspect was an internal wave that carried the submarine rapidly deeper than its crush depth.

1.3.3 Measuring the internal waves

Conventional methods (ships) to detect and measure internal wave properties are expensive and limited to the collection of data over a fairly localised region. However, many applications such as the modelling on which forecasts and now casts are based are not sufficiently precise without incorporating ocean data. The use of remote sensing data when combined with additional knowledge such as the tidal properties and a limited number of in-situ observations improves the accuracy of internal wave models. Without the wide area data provided by the spaceborne sensors, forecasts are not accurate enough for offshore operations management. The availability of satellite instruments also reduces the requirements for in-situ instrumentation. Spaceborne sensors data potentially represent a very large cost savings over conventional techniques. Indeed, an effective and reliable forecasting service could not be envisaged without such data.

Because internal waves interact with the sea surface and modulate the surface wind

waves, they modify the surface roughness pattern. These changes in surface roughness enable the Synthetic Aperture Radar (SAR), which is a roughness sensor to image the presence of an internal wave [1][3].

1.4 Synthetic Aperture Radar

The term 'radar' was coined in the 1930s and is an abbreviation for Radio Detection And Ranging. Radar is an instrument that transmits pulses of radio waves and detects the echo. The information received depends on the viewing angle, the polarization and the properties of the return signal from the scattering target. Due to the relatively long wavelength in microwave, the signal is able to penetrate undisturbed through clouds. The signal is also independent of sunlight since it is an active instrument; it both transmits and receives its own signal.

With real aperture radar the beamwidth and angular resolution of radar's antenna is determined by its dimensions, expressed in relation to the wavelength used. Synthetic Aperture Radars (SAR) overcome this limitation. They manage to achieve considerably better angular resolution by exploiting the movement of the platform and therefore synthesizing a large antenna.

1.4.1 Imaging process

The rectangular antenna of the radar is aligned with respect to the platform line of flight in such way as to direct a narrow beam side ways and downward onto the target (Earth's surface) see figure 1.5. Imagery is built up from the time delay and strength of the backscatter signal.

As the incidence angle of a SAR is oblique to the local mean of the sea surface, there is no specular reflection except when very high sea states occur. It is therefore assumed that Bragg reflection is the primary mechanism for backscattering radar pulses [68]. For a radar emitting radio waves of a wavelength λ_R, the sea surface waves which will contribute to the scattering are those with a wavelength close to λ_s where:

$$\lambda_s = \frac{\lambda_R}{2\sin\theta} \tag{1.4.1}$$

and θ being the incidence angle of the sensor.

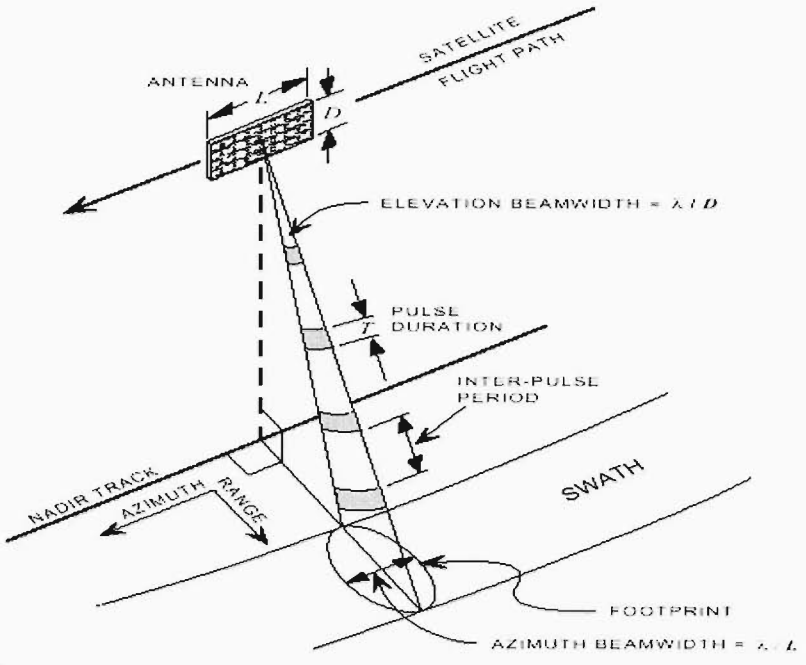

Figure 1.5: SAR ground pattern

Backscatter

The geometry and electrical features of a target, e.g. the dielectric constant, are the main characteristics that effect backscattering [9]. The geometry is defined by parameters such as slope and roughness, see figure 1.6. The dielectric constant of a material depends, among other variables, on its water content, temperature and salinity. The constant contains a real part, the permittivity, and an imaginary part, which is a loss term. The permittivity is a measure of how easily the energy of a radar signal passes across a dielectric interface. The imaginary part describes how much energy is absorbed in the volume once it passes across the interface. Major contrast in permittivity between two media leads to large surface scattering. If the contrast is low, the energy is transmitted across the interface and will be available for scattering and absorption in the volume. Radar cross section [3] besides the medium characteristics, σ^0 depends on wavelength, polarisation and the incident angle of the radar signal [39]. The longer the wavelength of a signal, the deeper the signal penetrates the material. The microwave wavelengths are in the range of 0.001 - 1 m which correspond to the frequencies between 0.3 - 300 GHz.

The incidence angle plays a crucial role in backscattering. The impact of the incidence

[3]Radar cross section is the measure of a target's ability to reflect radar signals in the direction of the radar receiver, i.e. it is a measure of the ratio of backscatter power per steradian (unit solid angle) in the direction of the radar (from the target) to the power density that is intercepted by the target.

angle in combination with roughness can be seen in figure 1.6. For small incidence angles, less than 20^o, specular reflections from facets dominate the returned signal. In the case of incidence angles between 20^o and 70^o, the dominating mechanism of the reflected signal is the Bragg scattering. Bragg scattering is a mechanism in which the reflected signal is in resonance with the incident wave.

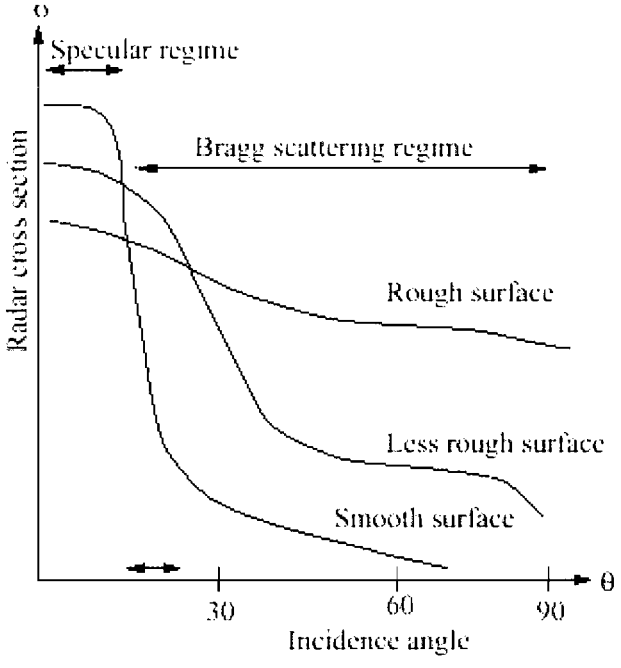

Figure 1.6: Backscatter as a function of the incidence angle and roughness [54]

Range resolution

The range resolution depends on how short the pulse length is. If all energy is sent at the same time in a very short pulse, it is obvious which part of the signal that was sent first. The problem is that a single pulse, short enough to give accurate range resolution and strong enough to be measurable after scattering at the surface, would require too much power and too large a bandwidth for the radar. However, if the pulse is long, there must be an ability to distinguish the first part of the pulse from the last part, in order to get satisfactory resolution. The solution is to use a longer, frequency modulated pulse, known as a chirped pulse. Using a chirped pulse, the instantaneously emitted power can be low, although the total emitted energy is high. A frequency delay filter demodulates the received pulse to a short spike, which gives a high range resolution.

Azimuth resolution

SAR uses the forward motion of the satellite to synthesise a longer antenna that enhances the azimuthal resolution. The resolution is achieved by recording the phase as well as the amplitude of the echoes along the flight path. To identify where the each returning pulses comes from in the illuminated area, doppler shift is used. To achieve this return pulse must be recorded in great detail together with the elapsed time.
The azimuth resolution is proportional to the real aperture length and this is independent of the range and the platform altitude.

Speckle

The scattering wave is made up from several elements on the surface. Because the path length from the radar antenna to the surface can vary from a few wavelengths with the resolution cell, which is made up of the individual return pulse with different phase, the amplitude of the signal is variable.
The coherent nature of SAR images produces a noise-like characteristic known as speckle. Speckle is a universal property of coherent imagery and arises because each resolution cell can be thought of as being made up of many individual point scatterers. In some case these individual return pulse will be add up constructively, in other they will be add up deconstructively. This phenomena results in a random speckle being added to the image. The speckle will decrease the clarity of the image and may be responsible for the large variability in the backscatter.
Because the speckle phenomena are purely random, it can be reduced by averaging several independent looks. This processing when possible is known as a multi-look and is well documented in the literature (e.g [45]).

1.5 Imaging internal waves

The internal waves interact with the surface waves and modulate the surface wind waves. This modulation can either be achieved by surface film (slicks) that accumulate in flow convergence zones and dampen the short surface waves there or by hydrodynamic interaction of these waves with the horizontal surface current associated with internal wave motion (see figure 1.7).

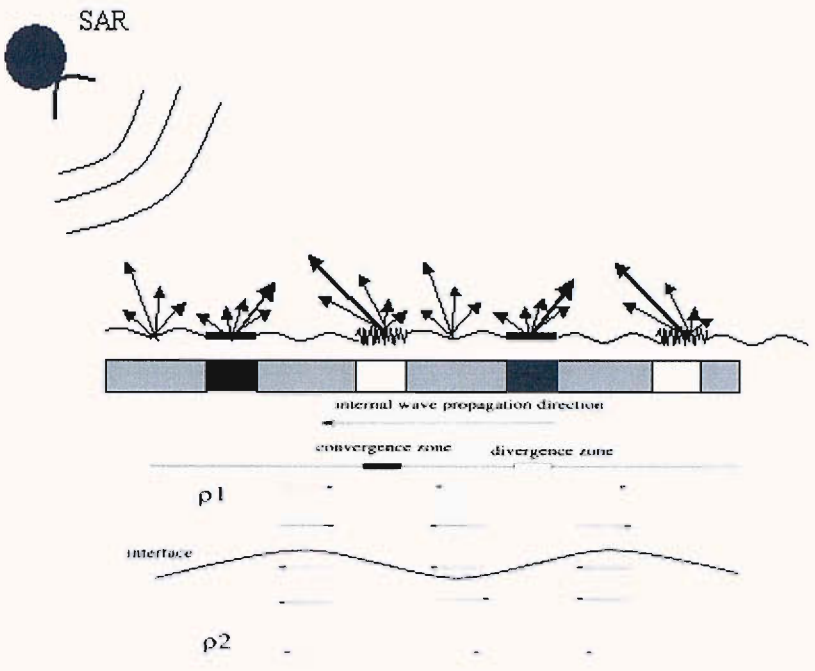

Figure 1.7: A sketch of an internal wave showing the fluid-particle velocity and the surface convergence zone; ρ is the density, where $\rho 1 < \rho 2$ and h1 the mixed layer depth. the vector arrows indicate direction and particle velocity.

The radar is a surface roughness sensor: the higher the roughness, the higher is the radar return and the brighter is the image intensity. IW forms are associated with rough and smooth bands and usually appears as bright and dark bands in the gradient of the surface velocity (u) that is the surface convergence: theory [1], the relative variation of the normalized radar cross section (NRCS) associated with internal waves, $(\Delta\sigma)\backslash(\sigma)$, is linearly related to the gradient of the surface velocity (u) that is the surface convergence:

$$\frac{\sigma\Delta}{\sigma_0} = -A \times \frac{\delta u}{\delta x} \tag{1.5.1}$$

Where A denotes a positive coefficient that depends, among others, on radar wavelength, incidence angle, and surface wind velocity. For a linear SAR system $(\Delta\sigma)\backslash(\sigma)$ is equal to the relative variation of the SAR image intensity, $\Delta I/I_0$. Thus the variation of the image intensity is proportional to the gradient of the surface velocity (=-$\delta u/\delta x$).

Hydrodynamic modulation fails to predict the dark slick bands that sometimes occur in an image. These have been connected to films, which would transform the dark/bright signature into only dark bands. The surface film, which is believed to be primarily made up of naturally occurring surface-active organic materials and which is concentrated at the surface of the ocean, is often active in coastal water. These films dampen short surface waves very strongly, reducing the radar return pulse. The radar

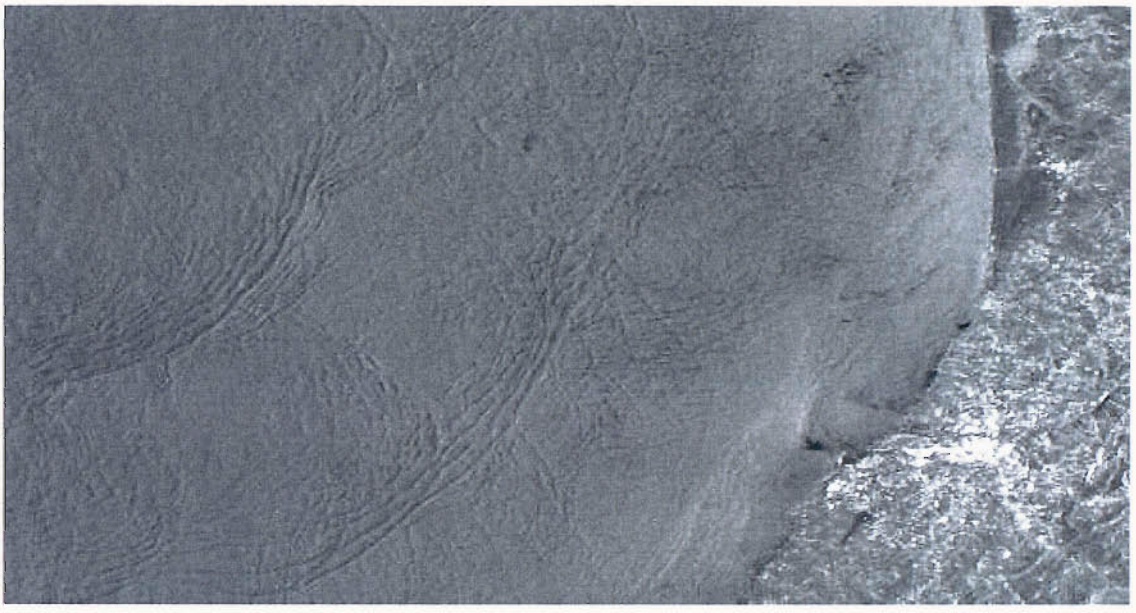

Figure 1.8: Example of internal waves imaging by the SAR

images then consist of dark streaks on a uniform bright background. However in most cases, the radar signature of the internal waves has a double signature, which means that the corresponding radar image consists of bright and dark streaks associated with the internal waves, indicative of hydrodynamics modulation. The cellular currents that accompany them are of the same order of magnitude as the wave phase speeds (50-75cm/s) and produced convergence and divergence near the surface strong enough to alter the short-length surface gravity and capillary wave by means of a periodic modulation that result in a surface signature characteristic of the underlying internal wave field. Figure 1.7 shows how the backscatter is influenced by the internal Waves.

As the signature of the internal waves is a modulation of the surface wind waves, the strength of the wind is an important factor. It was established that no internal waves are present on a SAR image for a wind equal or greater to 11 m/s and that the slicks are only visible with a wind less than 6 m/s [3].

Types of signatures and Transition mode

Analyses of the radar intensity modulations produced by the short-period IW signatures are in the form of bright/dark, dark and bright bands. They correspond respectively to positive/negative, negative or positive variations of radar backscatter from the mean background clutter (undisturbed by IWs). Based on these different types of signatures Da Silva *et al* [19] define a classification scheme. They identify a double-sign signature

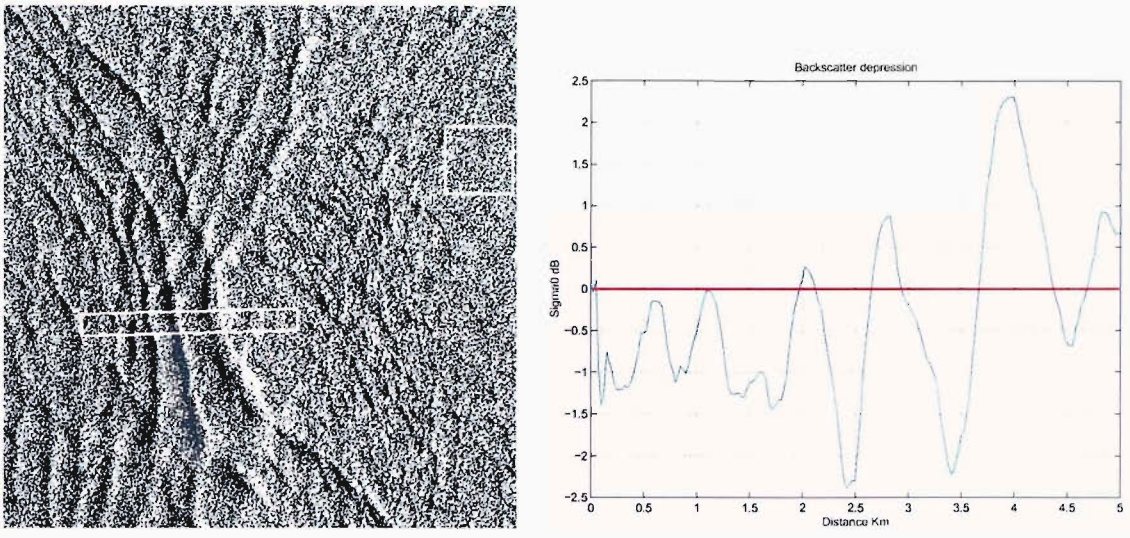

(a) A (b) B

Figure 1.9: Transect on an internal wave SAR signature

when +/- variations are identified, single-negative when a predominant negative variation occurs, and single-positive when a positive intensity variation is detected. The observations show that at very low wind velocities (less than 2m/s) IWs show up as single positive sign. When the wind is higher than 2 m/s, and for IWs propagating in the radar range direction (across track direction), both double and single negative signatures are commonly observed. For azimuth propagating IWs (along track direction) negative signatures prevail.

Figure 1.9(a) presents a close look at short-period internal waves. Figure 1.9(b) presents the backscatter depression of the transect of the internal wave. The leading waves display a double sign signature while the rear waves in the packet can be classified as single negative. This change from double to single signature is a transition mode. Figure 1.10 shows the typical transition mode. The factors that determine which, if either, of these mode transitions will occur under a given set of wind speed and surface film conditions seem to be rather subtle. According to [20], the two controlling variables appear to be wind speed and surface film pressure. Figure 1.11, shows the transition line on a film-pressure/wind-speed diagram, corresponding to the conditions for all mode transitions.

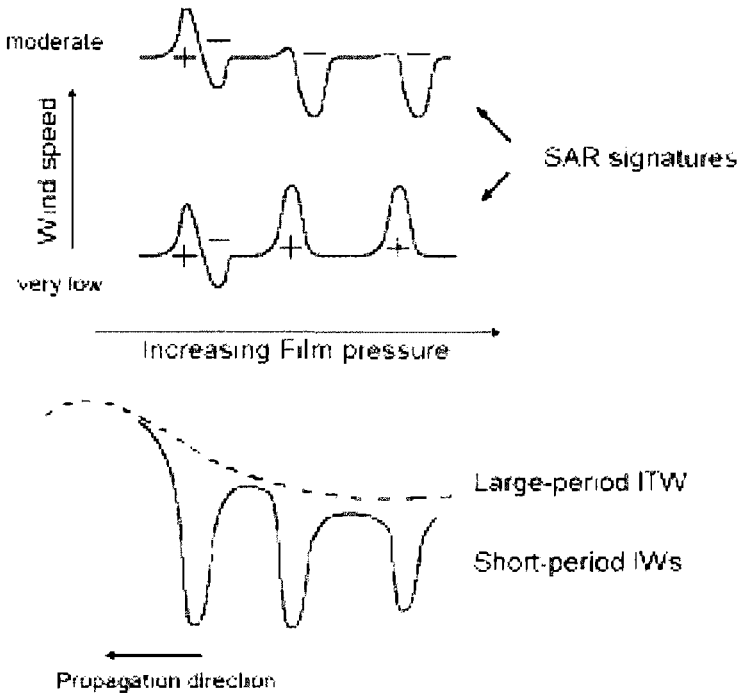

Figure 1.10: Two types of signature mode transition

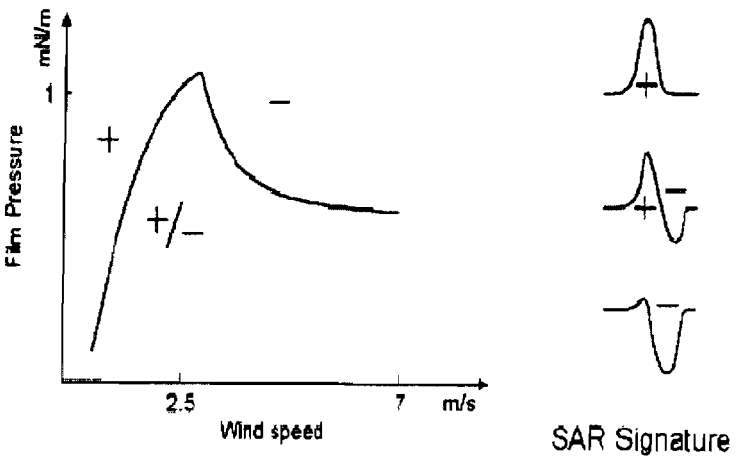

Figure 1.11: Signature mode transition diagram [20]

Chapter 2

Methodology

2.1 Strategy

The aim of this research is to successfully detect internal wave signatures in SAR images automatically. This task needs an elaborate analysis strategy in order to characterize the internal waves signature (IWS). A general description of the characteristic feature of the IWS was presented in chapter one. IWS can be considered as pseudo-invariant features. They have common features but also variable features such as the orientation, the curvature and the length of the waves. Furthermore, the SAR scene can be very complex showing land, interactions between internal waves and other mesoscale features. Every one of the above phenomena can interact in a constructive or in a destructive way on the IWS, and so modify its appearance. The variable features of the IWS and the possibility of a crowded SAR scene prevent the creation of a general blueprint to recognize efficiently IWS. As a consequence a segmented and independent analysis of the presence of certain IWS feature has to be considered. A SAR image is a three dimensional signal, which is composed of a frequency signature, textures, and geometry shape associated to each of the different features present within the signal. The proposed strategy is based on these primary characteristics of an image. It is possible to detect the presence of IWS within a SAR images by studying independently the frequency component, the texture and the geometric shape present in the image. Then each result can be linked with the others and a final test can be performed to evaluate the probability of IWS presence.

Before going through the detail of the different technique and the strategy used, it is necessary to understand how the choices have been made. An internal wave signature is a very complex feature and this can reduce the clarity of the signature wanted.

Previous studies on features extraction from satellite images such as T.Rachin [53] or Kiran [60] and Liu[38] have proven that wavelet transform based processing can be a powerful tool. These studies have been done for general purposes or more specifically with an oceanographic point of view. However they show that whatever the goal, a wavelet transform approach is very successful in edge extraction and multi-resolution analysis. Rodenas and Garelo [55] [56] even investigate a multi-resolution wavelet approach to detect the presence of internal waves on SAR images. A multi-resolution wavelet based approach has the advantage to make a frequency's discrimination at different levels, offering the possibility to extract any signature wanted at a given level. This technique is an appropriate solution for the SAR images and offers the possibility of analysing the remaining signature in term of texture or edge. However this discrimination does not give us any detail on the composition and the composition of the image. To establish the presence of IWS more processing are needed. A first approach is to consider the texture of the images. An image is composed of different range of tone and texture organization. Julesz [34] was the first to use gray tones spatial dependence occurrence statistics in texture discrimination. The idea was quickly developed by Haralick [28] [29], who suggested that the use of a two-dimensional spatial dependence of gray tone in a co-occurrence matrix. This texture discrimination is still found in numerous classification application such as remotely sensed imagery applied to sea-ice or medicine [24] [59][66]. The method has the advantage of offering a simple quantification of the different texture present in the images, which can then be easily used by a classifier. To perform the classification a large number of techniques exist from the statistical to the neural network approach. Due to the large choice, the variation in performance and the different requirements, it has been difficult to find an ideal classifier. However three techniques, for their different requirements, have been retained: A neural network multi layer perceptron, a K nearest neighbours and a PCA technique. The K nearest neighbours is the simplest of the three, and identifies the k nearest neighbours of an unidentified test pattern within a hyper-sphere of predefined radius in order to determine its true class [11]. The PCA on other hand involves a mathematical procedure that transforms a number of correlated variables into a smaller number of uncorrelated variables called principal components. These principal components can then be used to determine the membership to a class. The last of the three is the neural network multi layer perceptron, which perform a generalization of the process by training. The three classifiers will be used in parallel to establish their individual performance, and

different combinations with the input data and the training set will be made in order to optimize their performance.

Another approach that can be used to understand the image composition and to localize sharp variations in the signal is to extract the dominant edges resent in the images, and analysis their orientation and geometry. This can be done with various methods. However, because the previous processing was made using wavelet transform, one can use this information to calculate the modulus of the wavelet coefficient and obtain the dominant edge for a given resolution. One can then apply an edge tracing technique and then find the relationship between edges (i.e. are they pseudo-parallel to one another?). Because one of the internal wave characteristic is that there are at least 3 parallel crests within a packet, one can use the above proposed processing to recognize possible link between different edges and the presence of internal wave. This second approach has the advantage to pinpoint the exact position of every edge that composes any give internal wave signature. Therefore after a positive identification, the signature can easily be analyse to extract primary information such as the orientation, the type of modulation that occurred, and when possible the speed of the wave.

2.1.1 Detection System

From the above descriptions, the detection system will use two different and independent strategies: In the first approach, the system will be design using textural information, and in the second method the detection will be made using edge geometry information. The figure 2.1 show the distinct elements of the system for the two approaches. Every element is dependent of the previous one and their descriptions are as follow:

- **Image (Pre-processing):** *Preparation of the raw data.*

  Speckle is an important part of SAR image, and it needs to be reduced. Because the multi-look technique is not an option for dynamic features a simple pixel average is performed. It is also necessary to select part of the image that is land free, as no land mask technique has been incorporated in the processing yet.

- **Segmentation, Wavelet transform:** *Multiscale analysis.*

  The aim of the processing is to make scale discrimination. In the case of crowded SAR images composed of various mesoscale features, the possible internal waves signature can be weakened by other more powerful signatures. Therefore the use of multiscale wavelet analysis offers the possibility of processing each signature

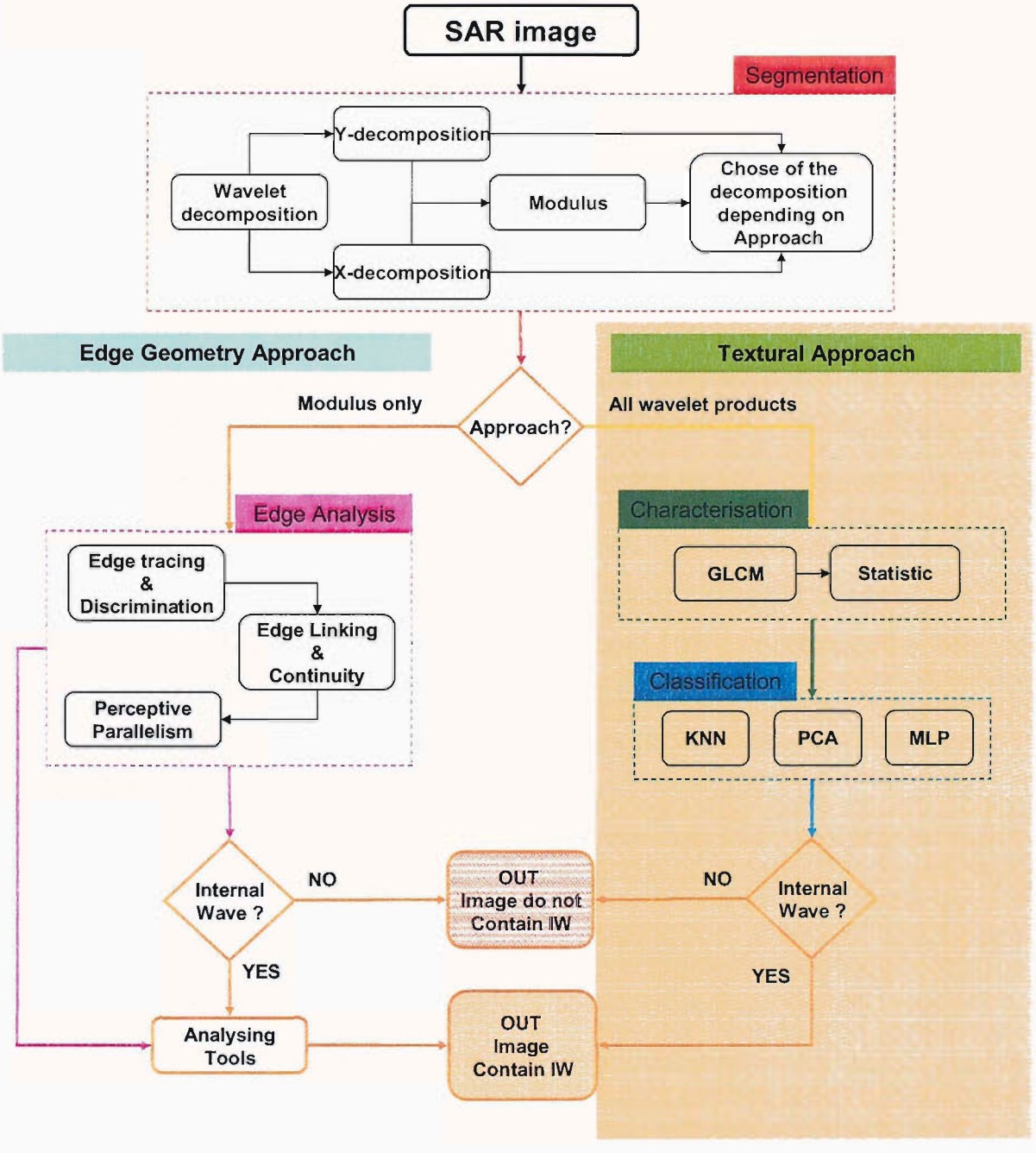

Figure 2.1: Diagram illustrating the layout of the processing

for a given scale.

- **Edges:** *Study of the parallelism of the edges.*
  Another approach to understanding the image composition and to localize sharp variation in the signal is to extract the dominant edges within the images. This can be done with various methods. However, because the previous processing was made using wavelet transform, this information can be used to calculate the modulus of the wavelet coefficient and obtain the dominant edge for a given

resolution. An edge tracing technique can be applied and then the relationship between edges can be found (i.e. are pseudo-parallel to one another?). Because one of the internal wave characteristic is to have a least 3 parallel crests within a packet, one can use the above proposed processing to recognize a possible link between different edges and the presence of internal wave.

- **Texture:** *Texture analysis using GLCM.*
  At this stage of the processing the analysis focuses on the texture organization and Grey Level Co-occurrence Matrix (GLCM), which addresses the average spatial relationships between pixels of a small region or window, to characterize using statistical indexes the sharp gray scale variation when an IWS is present.

- **Classifiers:** *Classification using a KNN or an MLP or a PCA .*
  The above processing characterizes the different signatures within the signal, but does not make any decision about the presence of IWS. To perform this task three classifiers will be used. The first one, which does not require any training but only a query set is the K nearest neighbours (KNN). The second classifier, which requires a training section is the multi layer perceptron (MLP). The last one which uses the principal components of two different classes, uses the GLCM as input directly.

- **Analysis:** The last part of the processing is the analysis of the detected IWS. This analysis will extract the orientation, the types of signature (i.e. type of modulation), and infer the possible direction and wavelength of the wave.

Each step of the processing will be described in a separate chapter along with the mathematical background necessary to describe the process as well as the appropriate result and a discussion. In each chapter it will be shown how the presented processing is implemented and where its contribution take place within the general layout of strategy for the recognition of IWS on SAR images, shown in figure 2.1.

2.2 Data set

The data set is made up of 120 SAR images acquired from the two European satellites ERS-1 and ERS-2. The Southampton Oceanography Centre (SOC) provided the images. Each original PRI SAR images contain 8000 x 8000 pixels, with a pixel spacing

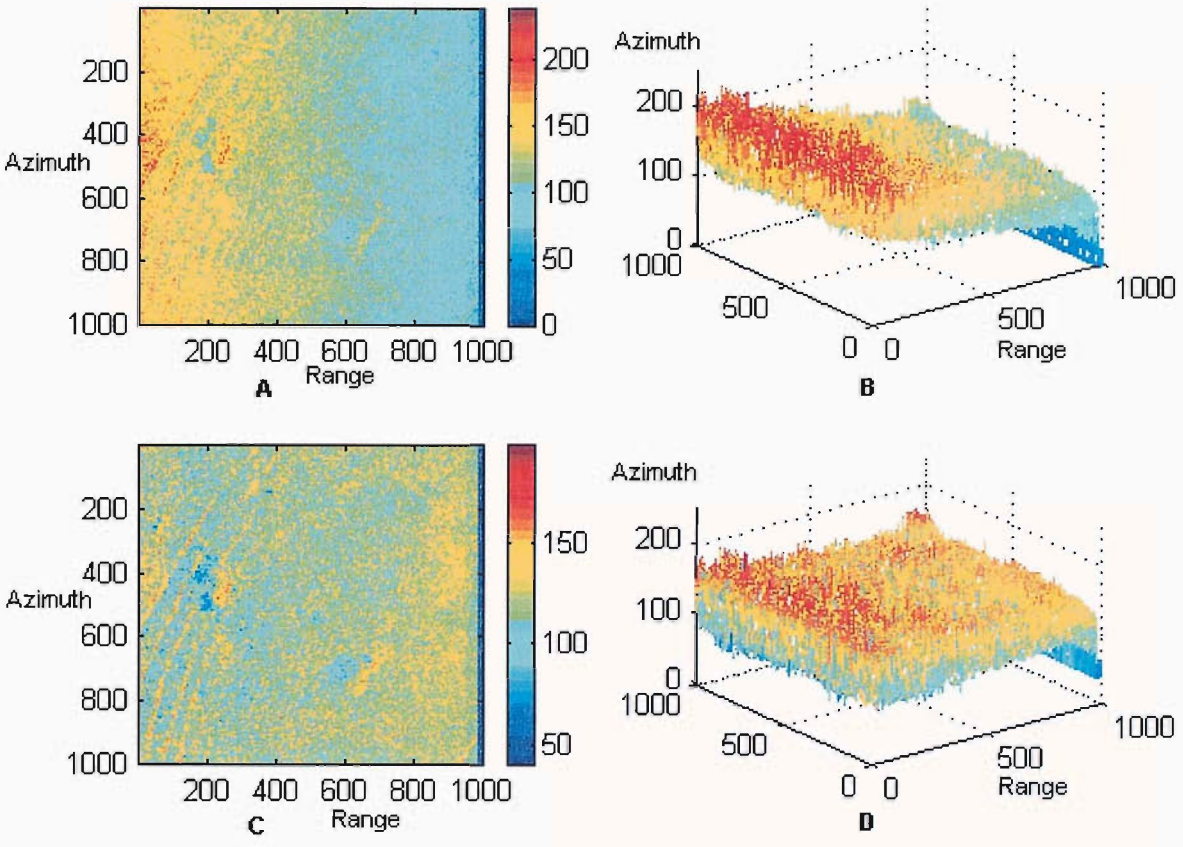

Figure 2.2: Range backscatter degradation.(a)Original image.(b)A 3D representation of the original image.(c) Same as (a)but with the correction.(d)Same as (b) but with the correction

of 12.5 m x 12.5 m, covering an area of 100 x 100 km. The motivation behind the creation of the data set was to obtain as many as possible images of internal waves observed by the SAR, and as a consequence the data do not concentrate on a particular region but it is composed of SAR images taken all around the world.

There is a reduction in the intensity of the backscatter as the range increase (see figure 2.2(a) and (b)) and there is more atmospheric attenuation. It is therefore necessary to apply a correction to compensate for this change in mean intensity in order to obtain a well-distributed mean background level and to have a stationary signal for the wavelet transform. The result can be seen in figure 2.2(c) and (d).

Because of the coherent nature of the illumination, SAR images contain multiplicative speckle noise. Therefore the first step is to apply an 8 x 8 pixel averaging technique to the original images. This procedure reduces the size of the image to 1/64, which offer a substantial reduction of the speckle as well as a reduction of the processing time. The pixels spacing is now equal to 100 m.

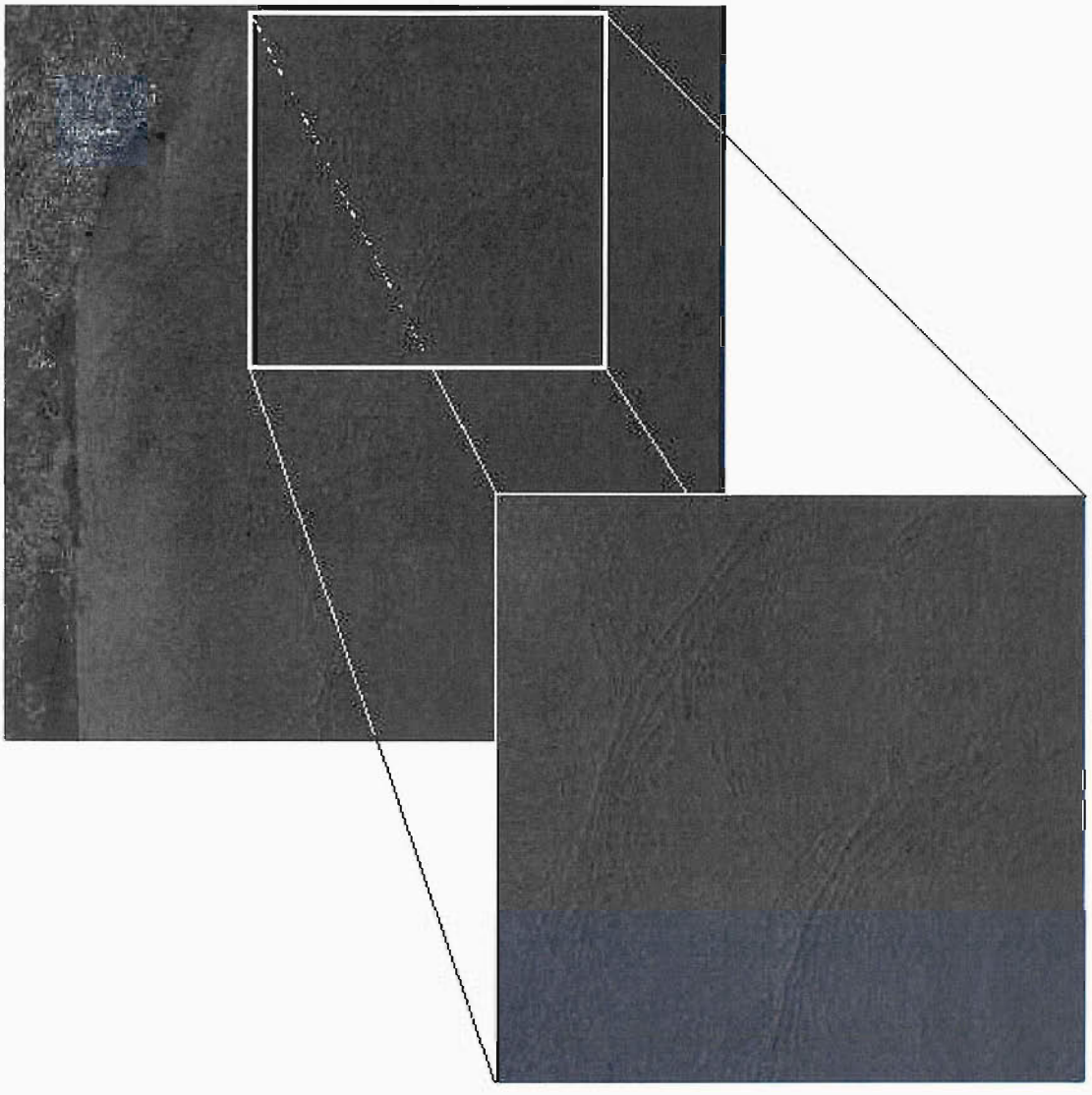

Figure 2.3: Original selected 512x512 SAR image containing an internal waves signature

The data set were made up of windows of 512 x 512 pixels, which were selected manually inside the processed original PRI Images. This selection provides the opportunity to create a succession of different data sets as well as the opportunity to select every scene land free. An example of a selected image can be seen in figure 2.3.

The different steps of the processing and the discussion of their performance will be illustrated by focusing on two images before giving a general overview of the result. These images are called image0 and image25 (figure 2.4(a) and 2.4(b)) and present very different internal waves signatures; one is very strong and projected in the diagonal of the image, the other is weak and projected in the vertical of the image. The difference in intensity and orientation of the signature, influence the results and the accuracy.

Further detail will be given for each different step.

2.2.1 The making of the training set

Three classifiers will be tried out. These classifiers need to be able to create a relationship between the classes. To do so, it is necessary to use a training set, where every class will be represented. The training set was made by manually selecting zones of the image containing some internal waves signature and zones without. In this selection one tried to give a fair representation of the internal wave signature as well as every other possibility that can represent a non-event zone.This gave approximatively 600 samples representing the two classes with an equal proportion and taken from several images.

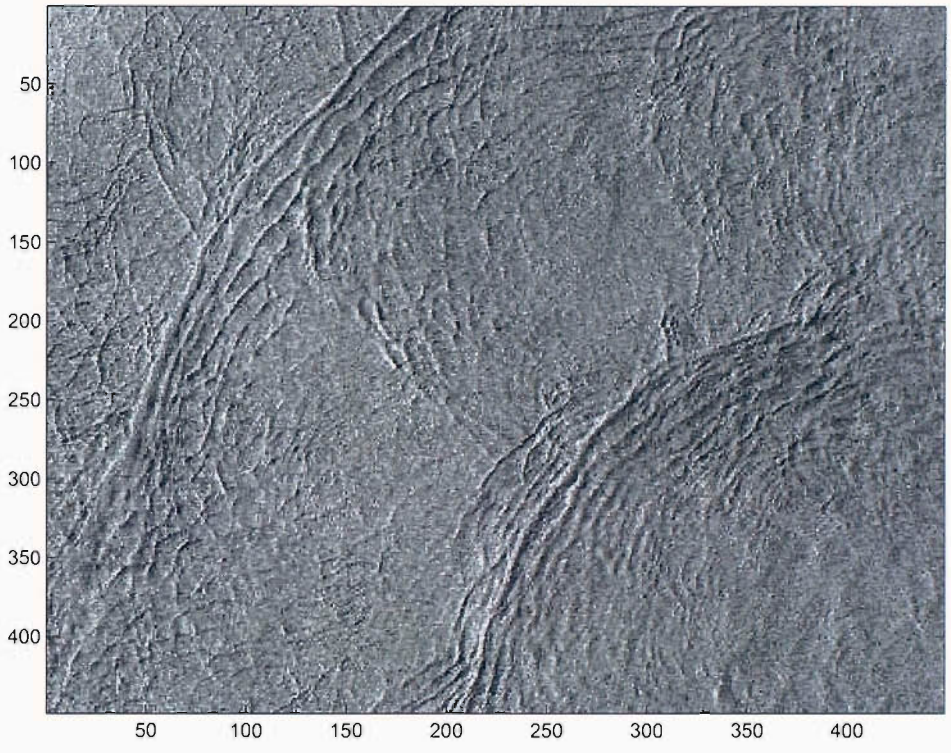

(a) Image0

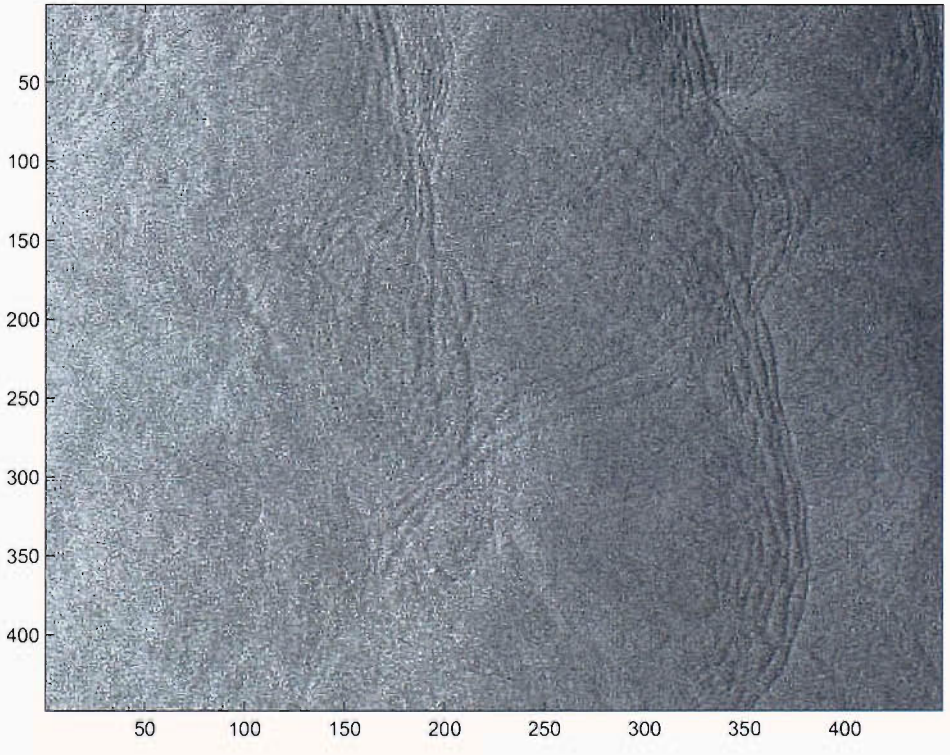

(b) Image25

Figure 2.4: The two images which will be specifically discussed during the processing

Chapter 3

Wavelet Transform

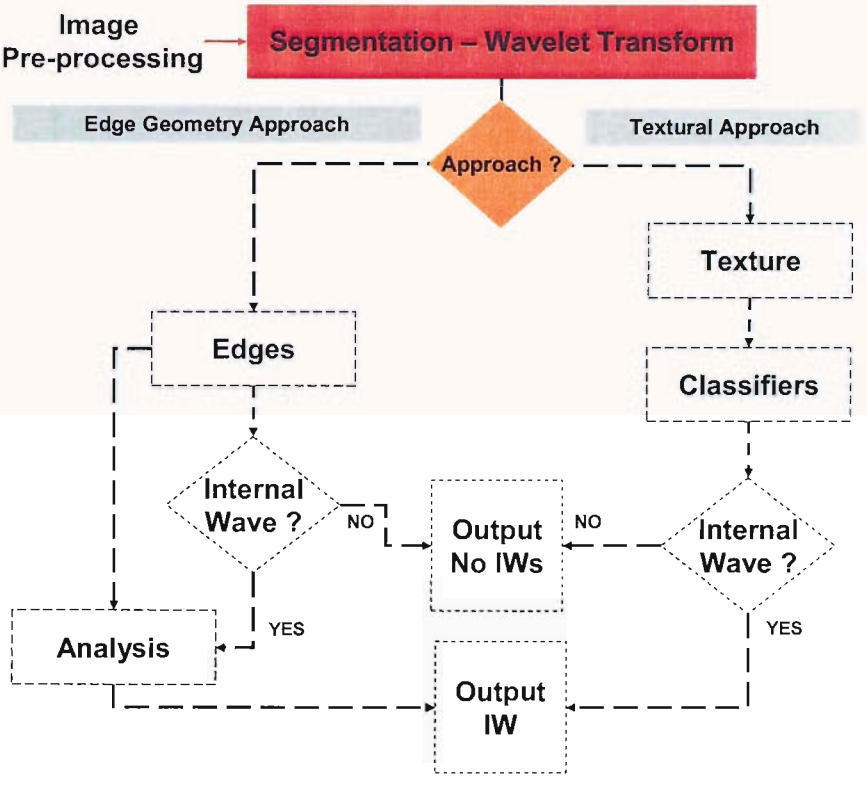

Figure 3.1: Diagram illustrating the layout of the processing

This chapter will describe the first step of the automatic detection of internal waves in SAR images. After a short background on wavelet transforms and a more detail explanation of the technique used, results of the transform will be presented. The chapter will end with a detailed explanation on how the different results from this multiscale decomposition will be used.

3.1 Background

Mathematical transforms are applied to a signal to obtain further information from that signal that is not readily available in the raw signal.

In practice most of the signals are Time-Domain in their raw format. The representation of the signal as a function of the time is not often the best solution. In many cases the most important information is hidden in the frequency content of the signal. The frequency spectrum of a signal is the frequency components of that signal. To derive this information a number of transformations can be applied to the signal. The most popular is the Fourier transform. The Fourier transform provides the connection between time and frequency in terms of the decomposition of harmonic waves, which the resulting frequency composition gives an average over the whole length of the signal. However if a signal changes at a specific time, its transform changes everywhere and a simple inspection of a transformed signal does not reveal the position of the alteration. It can therefore be assumed that a non-stationary signal is a sum of very small stationary signals, which will result in a sum of local decomposition. This approach gives the Short time Fourier Transform (STFT). In the STFT the size of the window is however fixed, which limits the flexibility. A fixed window cannot offer a good resolution in time and frequency at the same time.

One and a half decades ago an alternative to Fourier Transform and to STFT was found: The Wavelet Transform. The Wavelet Transform has a lot of similarity with the Fourier Transform. Both transforms are linear operations that generate a data structure that contains segment of various lengths. The mathematical properties of the matrix involved in the transform are similar as well. The inverse transform matrix is the transpose of the original. Both transforms can be viewed as a rotation in function space to a different domain. Another similarity is that the basis functions are localized in frequency. The main interests in the Wavelet Transform are its differences from the Fourier Transform. The individual wavelet functions are localized in space, which is not the case for the Fourier sine and cosine function. The Wavelet Transform uses a variable window. In order to isolate signal discontinuities, a very short window will be necessary. At the same time, in order to obtain detailed frequency analysis, one would like to have some very long base functions. For this to be achieved it is necessary to have short high frequency and long low frequency basis functions. This is exactly what can be achieved with a Wavelet Transform.

3.1.1 Multiscale edge detection

The edges of structure in an image are often the most important features for pattern recognition. One may consider an edge to be a sharp variation in the image (i.e. a strong intensity variation). On the contrary an edge can be considered to be a transition between two different textures (smooth intensity variation). The difference between these two definitions is the scale at which the image is observed. This discrimination of the edge definition motivates an edge analysis at different scales.

Many edge detection techniques exist, such as the Canny Edge Detector [13], which detect the sharp variation in an image by calculating the modulus of its gradient vector. A multiscale version of this edge detector can be implemented by smoothing the surface with a convolution kernel θ [40]. This is computed with two wavelets that are the partial derivatives of θ:

$$\psi^1(x,y) = \frac{\delta\theta}{\delta x} \qquad and \qquad \psi^2(x,y) = \frac{\delta\theta}{\delta y} \tag{3.1.1}$$

The associated 2-D Wavelet Transform of the image f at scale 2^j and orientation k is defined as:

$$W^k_{2^j} f(x,y) = f * \psi^k_{2^j}(x,y) \qquad k = 1,2 \tag{3.1.2}$$
$$with \qquad \psi^k_{2^j} = 2^{-2j}\psi^k(2^{-j}x, 2^{-j}y)$$

The Wavelet transform with respect $\psi^1(x,y)$ and $\psi^2(x,y)$ in (3.1.2) has two components:

$$\begin{aligned} W^1_{2^j} f(x,y) &= 2^j \left(\frac{\delta(f * \theta_{2^j})(x,y)}{\delta x} \right) \\ &= 2^j \overrightarrow{\nabla}(f * \theta_{2^j}(x,y)) \end{aligned} \tag{3.1.3}$$

$$\begin{aligned} W^2_{2^j} f(x,y) &= 2^j \left(\frac{\delta(f * \theta_{2^j})(x,y)}{\delta y} \right) \\ &= 2^j \overrightarrow{\nabla}(f * \theta_{2^j}(x,y)) \end{aligned} \tag{3.1.4}$$

The modulus of this gradient vectors is proportional to the wavelet transform modulus:

$$M_{2^j} f(x,y) = \sqrt{|W^1_{2^j} f(x,y)|^2 + |W^2_{2^j} f(x,y)|^2} \tag{3.1.5}$$

And its angle is equal to the angle $A_{2^j} f(x,y)$ of the wavelet transform vector (3.1.4),(3.1.5) in the plane (x,y).

$$\alpha = tan^{-1}\left(\frac{W^2_{2^j} f(x,y)}{W^1_{2^j} f(x,y)} \right) \tag{3.1.6}$$

$$\text{then} \qquad A_{2^j} f(x,y) = \begin{cases} \alpha & \text{if } W^1_{2^j} f(x,y) \geq 0 \\ \pi - \alpha & \text{if } W^1_{2^j} f(x,y) < 0 \end{cases} \tag{3.1.7}$$

Multiscale edges are points (x,y) where $M_{2^j} f(x, y)$ is locally a maximum in the one-dimensional neighbourhood of (x,y) along the angle $A_{2^j} f(x, y)$. These points are called wavelet transform modulus maxima.

3.2 Processing

Each individual image is decomposed into a representation of the energy coefficients at different scales, then for each individual level of decomposition the modulus is calculated. The procedure to perform the decomposition is as follow:
Suppose that the scaling function and the wavelet ϕ, ψ, $\tilde{\phi}$ and $\tilde{\psi}$ are designed with the filter h, g, $\tilde{h}$ and $\tilde{g}$ (see Appendix A for more detail). A fast dyadic wavelet transform is calculated with a filter bank called in French the *Algorithme à Trous* ("holes algorithm"). It is similar to a fast biorthogonal wavelet transform, without subsampling. It is computed from a_o (initial image) by a cascading convolution. An example of this decomposition is shown in figure 3.2.

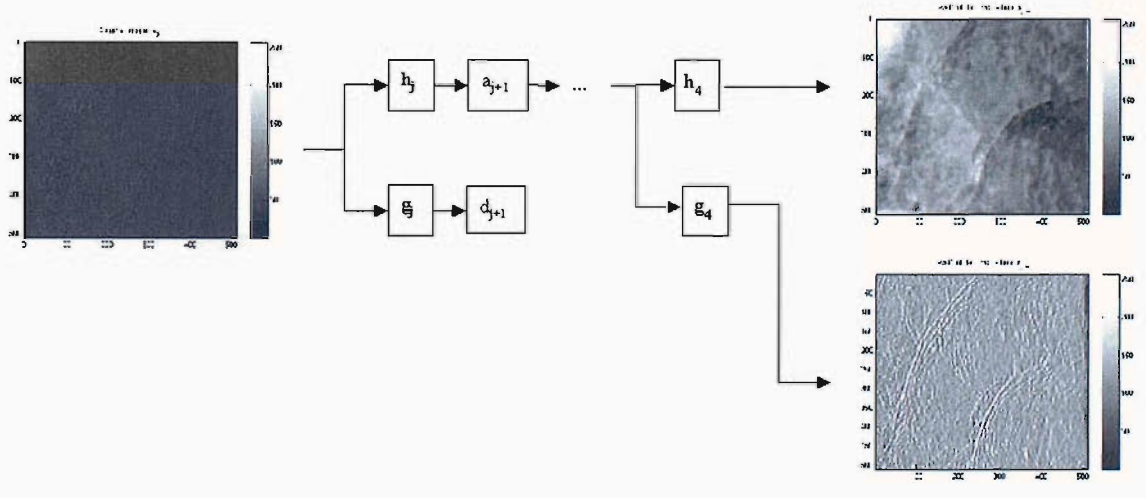

Figure 3.2: Cascading convolutions.

3.2.1 Results from the wavelet decomposition:

The wavelet transform provide an energy representation of the image at different scales. For each individual scale the decomposition in the x-direction, in the y-decomposition, the modulus and the gradient orientation are calculated (see figure 3.3).
Already some differences appear between the directions of decomposition used. If the signature of the internal wave propagates mainly horizontally or vertically, the detection

will be strongest in the x-decomposition and y-decomposition respectively. An example is shown in figure 3.5(a) and 3.5(b). However if the internal wave is orientated diagonally, this dissimilarity disappears (see figure 3.5(c) and 3.5(d)). These results although expected, have a direct influence on the calculation of the modulus. To reduce the internal wave direction influence on the classification, different wavelet representation will be used (i.e. difference on how the X-decomposition or Y-decomposition will be used). More details about the different wavelet representation used are given at the end of this chapter.

By definition the wavelet coefficient mean is null. Every time we have a positive structure at a scale, we have negative values surrounding it. These negative values complicate the analysis and create an artefact, so the positive or negative values are chosen separately for the rest of the processes. This choice is purely dependent on the use of an automatic threshold on the histogram. Once the modulus has been processed to optimize the edge and to reduce the unwanted features a non-maxima operation is applied on the modulus in order to refine the result and be able to process the next steps.

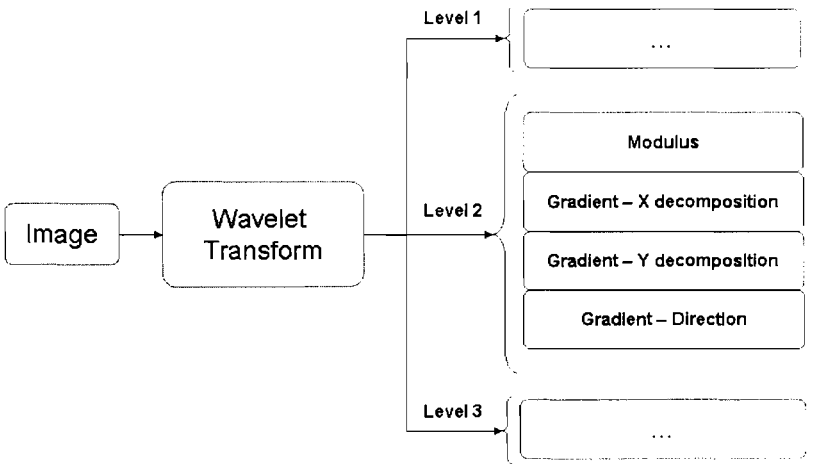

Figure 3.3: Output from the wavelet transform

Non-maxima suppression [46]: To thin the response of the wavelet transform and give edge points which are at the right place, a non-maxima suppression is applied to the modulus. Non-maxima suppression essentially locates the highest point in the edge magnitude data. This is performed by using edge direction information, to check that points are at the peak of a ridge. Given a 3×3 region, a point is at a maximum if the gradient at either side of it is less than the gradient at the point. This implies that we need values of gradient along a line which is normal to the edge at a point.

This is illustrated in figure 3.4. The point $P_{x,y}$ is to be marked as a maximum if its gradient, $M(x,y)$ exceed the gradient at the neighbouring points $M1$ and $M2$ which need to be interpolated. The first-order interpolation using Mx and My at $P_{x,y}$ gives:

$$M_1 = \frac{M_y}{M_x} M(x+1, y-1) + \frac{M_x - M_y}{M_x} M(x, y-1) \tag{3.2.1}$$

$$M_2 = \frac{M_y}{M_x} M(x-1, y+1) + \frac{M_x - M_y}{M_x} M(x, y+1) \tag{3.2.2}$$

The point $P_{x,y}$ is then marked as a maximum if $M(x,y)$ exceeds both M_1 and M_2, otherwise it is zero. In this manner the peaks of the edge magnitude data are retained. At which point hysteresis thresholding can be used.

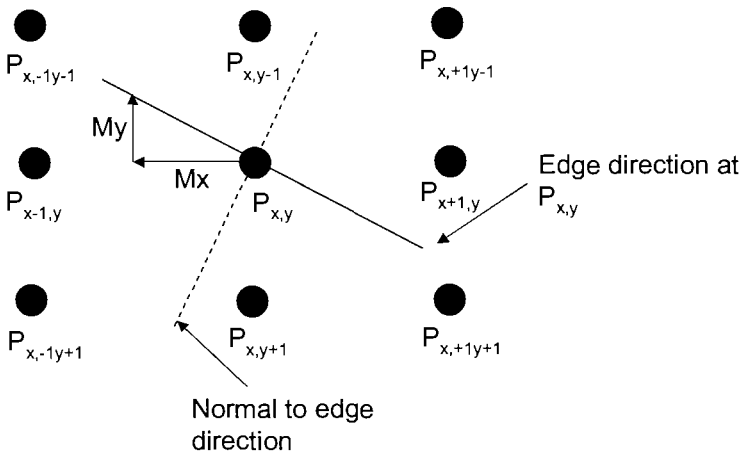

Figure 3.4: Non-maxi representation

At this stage of the process it will be interesting to recall that the modulus from the wavelet analysis will be use as a starting point for two different recognition techniques: the Edge analysis and the textural analysis.

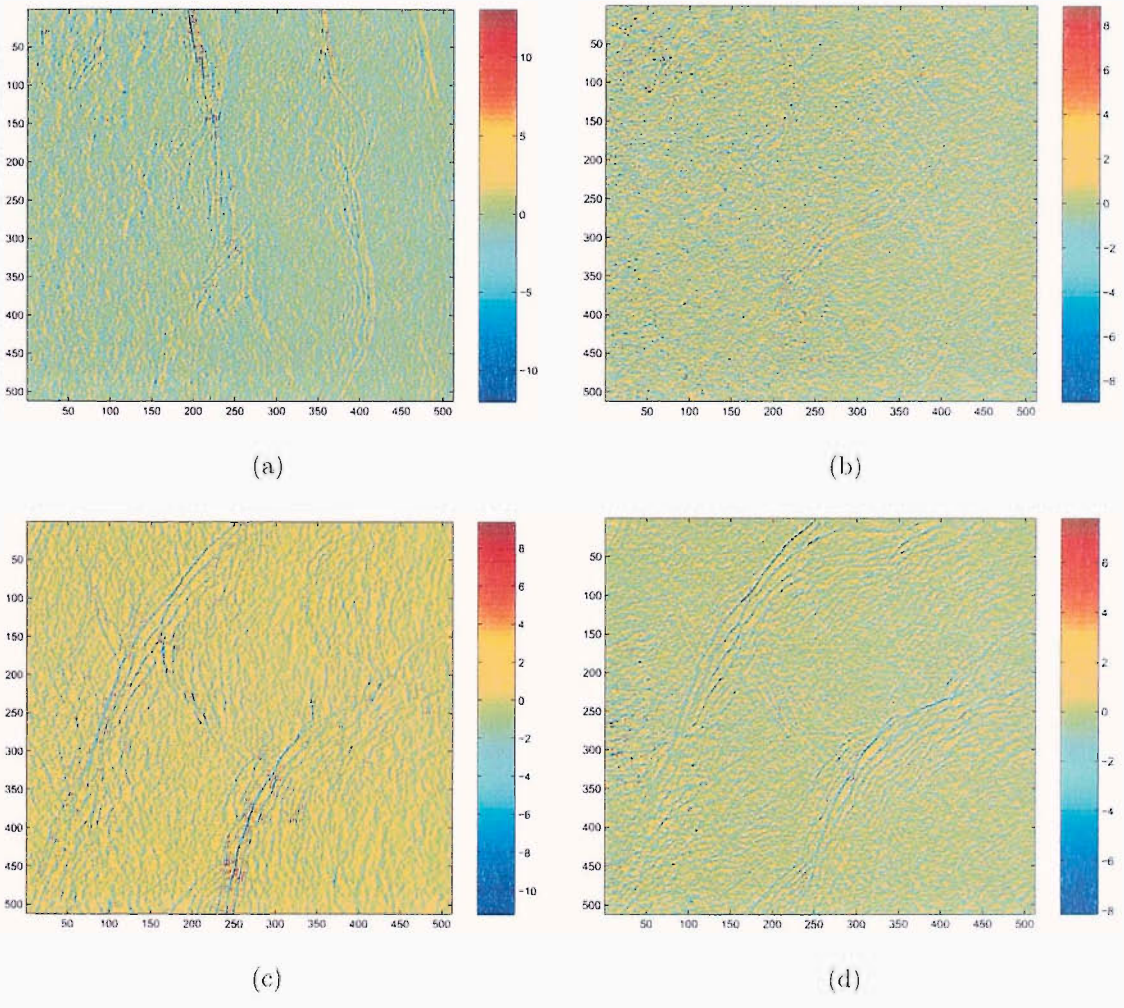

Figure 3.5: Wavelet coefficients at level 2 of the Image25 for (a) and (b) and Image0 for (c) and (d). (a)and(c) X decomposition. (b) and (d)Y decomposition.

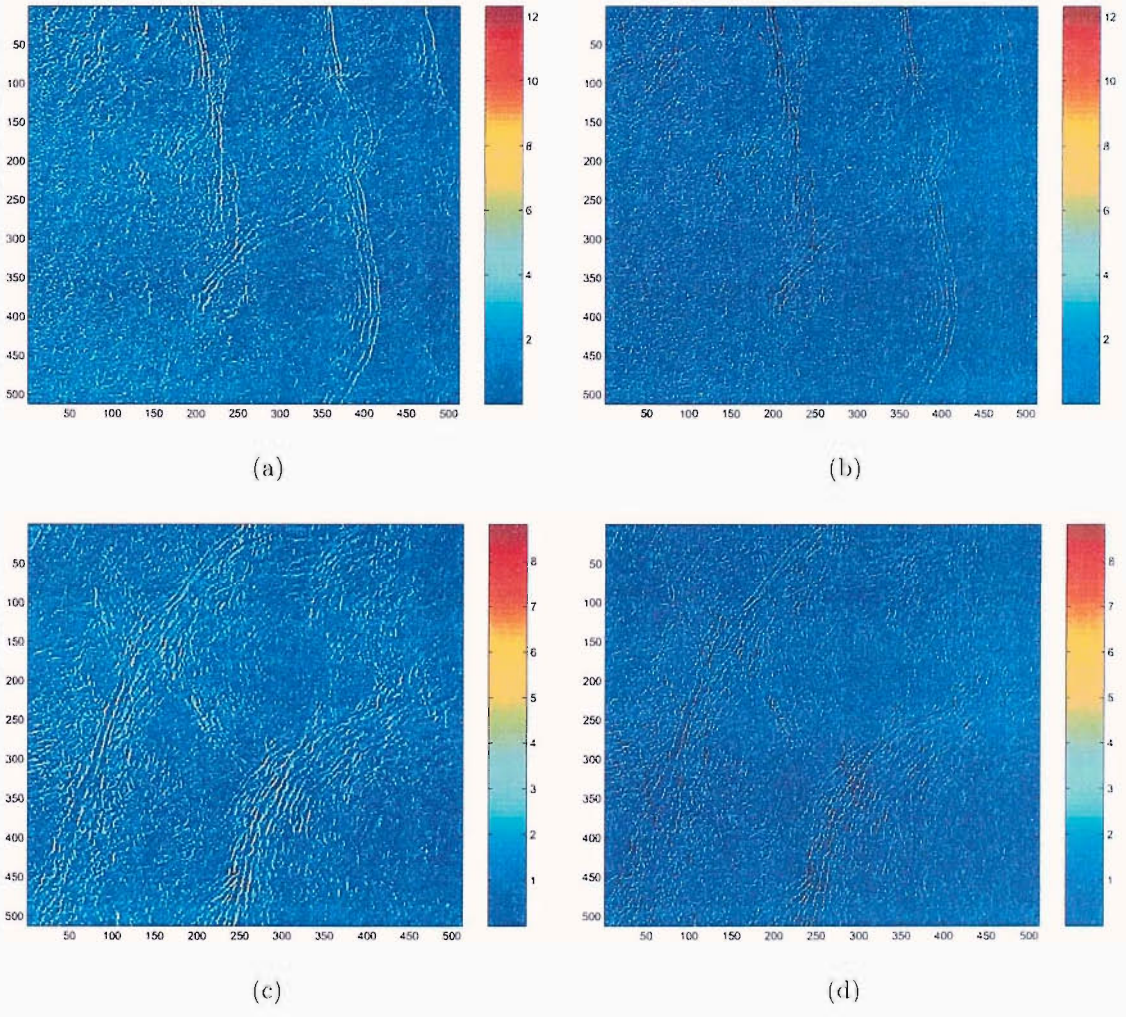

Figure 3.6: Wavelet modulus at level 2 of the Image25 for (a) and (b) and Image0 for (c) and (d). (a) and (c) without non maxima reduction. (b) and (d) with non maxima reduction.

3.2.2 Wavelets and their use

The last section of this chapter describes the use and the preprocessing of the wavelet output for the rest of the processing.

Wavelet for the textural analysis

The textural analysis has a straight forward approach to it. Three wavelet representations will be used, they are:

- **The modulus:**
  Two level of decomposition will be used: The second level and the third. The modulus at different level will be referred to as $M2$ and $M3$, modulus level 2 and modulus level 3 respectively. Before analysing the modulus, a threshold is applied automatically, and the modulus is coded over n number of colour (gray tones) to enable the calculation of the GLCM.

- **The mean between X- and Y-decomposition:** The orientation of the wave has an effect on the wavelet decomposition. Therefore one attempt to reduce this effect is to take the mean between the two decompositions. This wavelet representation will be called mXY and will only be made for the level 2.The mXY is coded over n number of colour.

- **X- and Y-decomposition independently:** In this case the X- and Y-Decomposition will be processed independently and the result will be used at the end of the process. This wavelet representation will be referred to as XY and will only exist for the level 2. In this case the colour coding is performed to the two components using the same scale. In this procedure, the relative importance of the two decompositions with each other is retained.

These representations were chosen in order to perform a good classification and they represent different ways in which the image can be analyzed.

Wavelet for the edge analysis

For this analysis, it has been shown [55] [56] that the best wavelet representation is the modulus of the second level of decomposition. The same method is used as the one used in the $M2$, $M3$ threshold calculation but this time the threshold is not applied to the modulus but is used in the edge tracing technique as a hysteresis threshold [62].

Chapter 4

Expression of the Texture

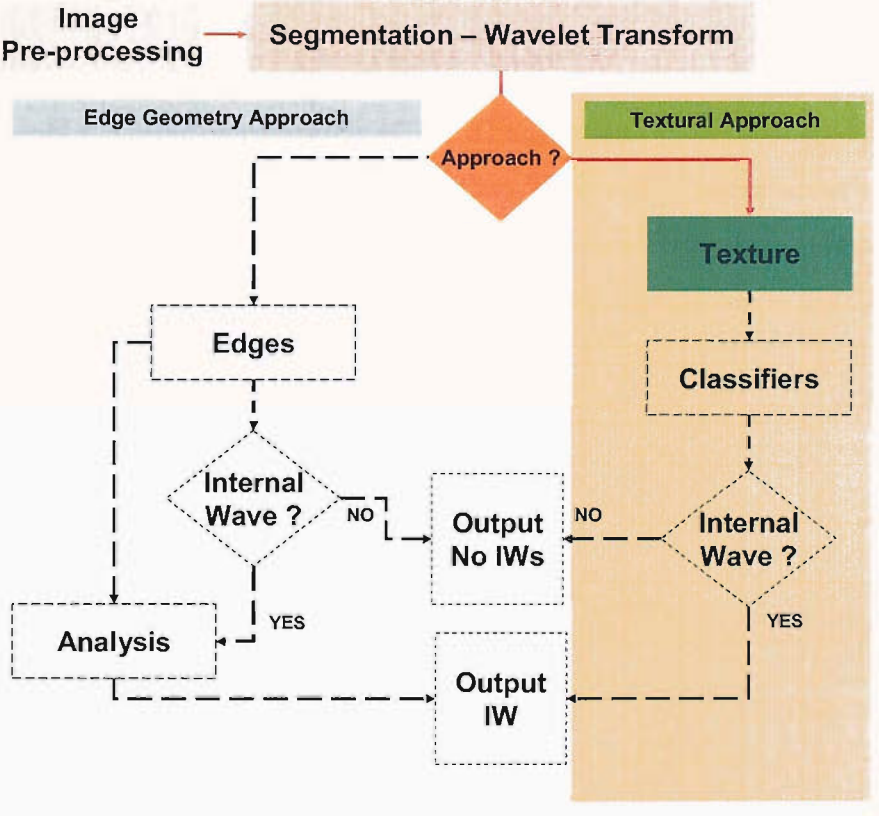

Figure 4.1: Diagram illustrating the layout of the processing

4.1 Texture

In a search of meaningful features for describing information within an image, it is natural to take into consideration the texture representation of the different features present. The texture represents the spatial distribution of the gray tone whereas the tone is based on the varying shades of gray. These two concepts are dependent and both contribute to an the understanding of an image. Texture can be evaluated as being fine,

smooth, irregular, rippled, etc. It contains important information about the structural arrangement of the surface and their environment.

The perspective of tone and texture is based on the concept that texture and tone bear an inextricable relationship to one another. This relationship is highly influenced by the variation of features and the size of the small-patch area. Haralick [29] suggested that in order to obtain the textural feature of an image, one can assume that the texture information is contained in the overall spatial relationship which the gray tones in the image have to one another. This texture information is specified by a set of gray-tone spatial-dependence matrices.

4.1.1 Grey Level Co-occurrence Matrix

The Grey Level Co-occurrence Matrix (GLCM) addresses the average spatial relationships between pixels of a small region or window. The texture information is described by a set of matrices $P(x, y)$. Figure 4.2 shows the nearest-neighbour resolution cell and Figure 4.3 show the matrices $P(x, y)$. Each element $P(x, y)$ expresses the frequency of

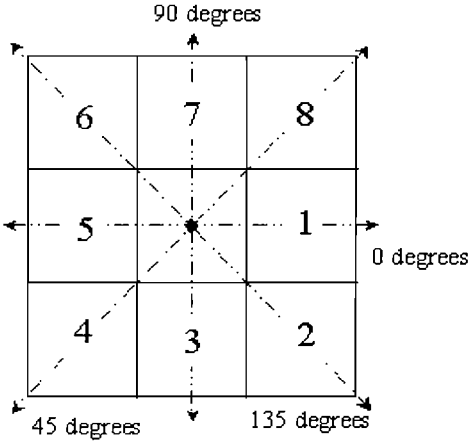

Figure 4.2: Resolution cell 1 and 5 are 0^o nearest neighbours to resolution cell •: resolution cells 2 and 6 are 135^o nearest neighbour;resolution cells 3 and 7 are 90^o nearest neighbour and resolution cells 4 and 8 are 45^o nearest neighbour to • [29].

occurrence of two points, with respective grey-levels x and y, at a distance $D(d, \theta)$ from one another. If an image is quantified by N grey-level, the GLCMs will be NxN arrays. In a homogeneous region, differences between grey levels will be low, and the element close to the diagonal of the GLCM will therefore have high values. Less homogeneous regions will result in GLCMs with high values further away from the diagonal. One important point to note is the sensitivity of GLCMs to linear combinations. If an offset

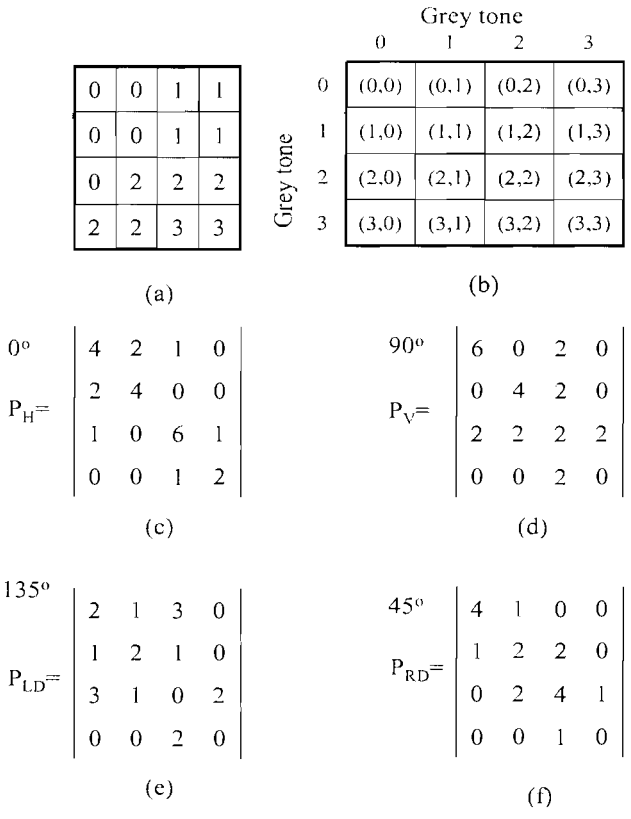

Figure 4.3: (a)4x4 image with gray-tone values 0-3. (b) General form for any gray-tone matrix for an image with gray tone value 0-3. (c)-(f) Calculation of all four distance 1 gray-tone co-occurrence matrices (P_H stand for the horizontal co-occurrence matrices, P_V for the vertical, P_{LD} for the left diagonal and P_{RD} for right diagonal). [29].

is added to all grey levels, the entries in the GLCM will be displace along the diagonal, however if all grey level are multiplied by a constant value, the entries in the GLCM will move away from the diagonal, resulting in a difficult interpretation.
The GLCM is very sensitive to the orientation θ [12]. Therefore to ensure that the textural indices of any texture are not significantly influenced by the angle, an average of the GLCM for four different directions is necessary.

4.1.2 Textural indices

A lot of textural indices are available from the current literature [12],[29]. Only five indices will be defined and presented here. The Entropy (Equation 4.1.1) measures the lack of spatial organization inside the computation window. The entropy is high when

all the $P(x, y)$ are equal, this corresponds to a rough texture and vice versa.

$$ENT = -\sum_{x=1}^{N}\sum_{y=1}^{N} P(x,y) \times \log_{10}(P(x,y)) \tag{4.1.1}$$

The correlation (Equation 4.1.2) quantifies the dependence of grey levels from one another for pixels separated by the distance D. A low correlation means that the grey levels are generally independent from one another (No regular structure in the image). If the correlation is high, one or several structures will repeat themselves in the image.

$$CORR = \frac{1}{\sigma_x \sigma_y}\left(\sum_{x=1}^{N}\sum_{y=1}^{N} \frac{xy}{L} \times P(x,y) - \mu_x \mu_y\right) \tag{4.1.2}$$
$$with \qquad L = \frac{\sum_{x=1}^{N}\sum_{y=1}^{N} xy \times P(x,y)}{\sum_{x=1}^{N}\sum_{y=1}^{N} P(x,y)}$$

$$P_x(x) = \sum_{y=1}^{N} P(x,y) \tag{4.1.3}$$
$$P_y(x) = \sum_{x=1}^{N} P(x,y)$$

μ_x, μ_y, σ_x and σ_y are the mean values and the standard deviations associated for each distribution and P_x and P_y are defined by the equation 4.1.3.

The Local Homogeneity (Equation 4.1.4) quantifies the amount of local similarities inside the computation window. Local homogeneity is larger for GLCMs with elements concentrated near the diagonal, because it is a function of $(x-y)^2$. These GLCMs correspond to textures of organized and poorly contrasted features.

$$HOMOG = \sum_{x=1}^{N}\sum_{y=1}^{N}\left(\frac{P(x,y)}{1+\left(\frac{x-y}{K}\right)^2}\right) \tag{4.1.4}$$
$$with \qquad K = \frac{\sum_{x=1}^{N}\sum_{y=1}^{N} |x-y| \times P(x,y)}{\sum_{x=1}^{N}\sum_{y=1}^{N} P(x,y)}$$

Inertia, also called second-difference moment (Equation 4.1.5) is indicative of the contrast of the GLCM. Because of the $(x-y)^2$ term, inertia is very sensitive to large differences inside the co-occurrence matrix. High contrast regions will have a high inertia, whereas more homogeneous regions will have a low inertia.

$$INR = \sum_{x=1}^{N}\sum_{y=1}^{N} \frac{(x-y)^2}{K^2} \times P(x,y) \tag{4.1.5}$$

Uniformity (Equation 4.1.6) is sometime referred to the second-angular moment. The lowest values of uniformity are attained when all the $P(x, y)$ are equal, and there are no dominant grey levels. In this case all grey levels, are equally probable. This is characteristic of a rough texture.

$$UNF = \sum_{x=1}^{N} \sum_{y=1}^{N} P(x, y)^2 \tag{4.1.6}$$

4.2 Co-occurrence matrix

Once the decomposition of the image into the energy coefficients is done, the result is coded over n colour codes (n=64) and it will be considered as an image with its variation of texture and tone. Each image is now subdivided, which give us 169 images of 64X64 pixels (called "subimages") . On these subimages, the grey level co-occurrence matrix is calculated in the four directions (0, 45, 90, 135 degrees) with a step of d pixels. Results are then averaged to obtain one grey level co-occurrence matrix per subimage. The GLCM at a given scale is calculated for the two decompositions (x and y) and the modulus. An example of a GLCM can be seen in figure 4.4. Both GLCM are orientated along the diagonal and the one with the wider distribution is the one representing part

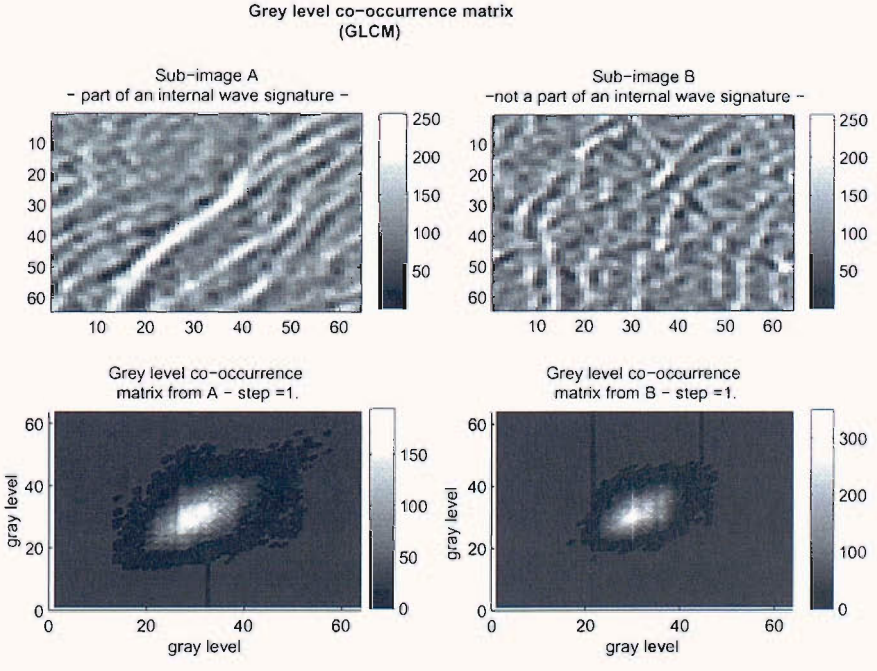

Figure 4.4: grey level co-occurrence matrix $d = 1$

of an internal wave signature.

Influence of the distance $D(d,\theta)$ The GLCM are influenced by the distance $D(d,\theta)$. The case of θ has been discussed earlier (see section 2.2.1). d, the inter-pixel displacement, is a variable that can contribute to a good or a bad representation of texture. The texture representation of the internal waves through the wavelet transform is composed of small curves with a width of 2 to 4 pixels. In this circumstance the values of d has to represent best as possible the strong variation in colour as well as the finest of the texture. In order to optimize the texture representation a few values of d were tried out. Figure 4.5 shows statistical indices plotted for different values of d. It can be seen that the value of d does not have a real influence on the statistical distribution of the GLCM. However a small d seem to produce the greater difference between internal waves and non-internal wave events. This conclusion can be related to the thickness of the wanted signature.

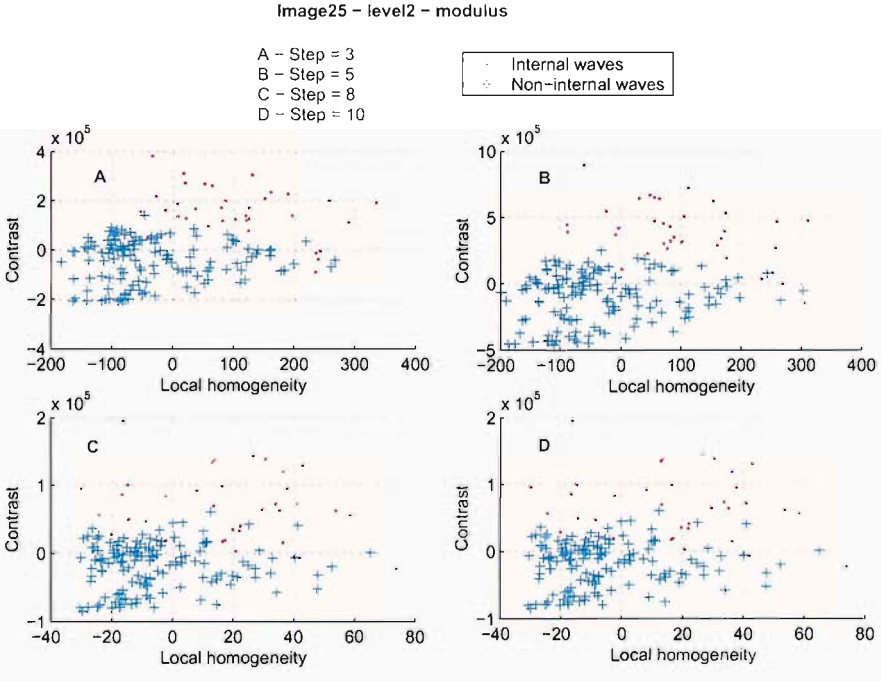

Figure 4.5: Statistical indices for modulus of the image25 level2 for different values of d

Influence of the IWS on the statistical indices: The top right panel of the figure 4.6(a) shows the statistical distribution of the GLCM for the image 25 modulus at level 2. The dots represent the IWS. The characteristics of the GLCM representing

IWS can be described by big contrasts, small entropy, and large correlation values. On the other hand the GLCM representing NIWS can be described by a small contrast, large entropy and small correlation values.

Influence of the internal wave orientation: The internal wave signatures of the image25 are oriented vertically in the image. It is therefore expected that there will be a good representation of the IWS with the x-decomposition and a very weak or no representation at all for the y-decomposition at any scale. Figure 4.6 show the image25 GLCM statistical representation for the x, y-decomposition and the modulus restively. The x-decomposition and the modulus statistical distribution of the GLCM show a large difference between IWS and NIWS. However the y-decomposition statistical distributions do not match the previous results. There is almost no difference in the distribution between the IWS and the NIWS. This result suggests that the wave orientation can have an impact on the accuracy of the detection.

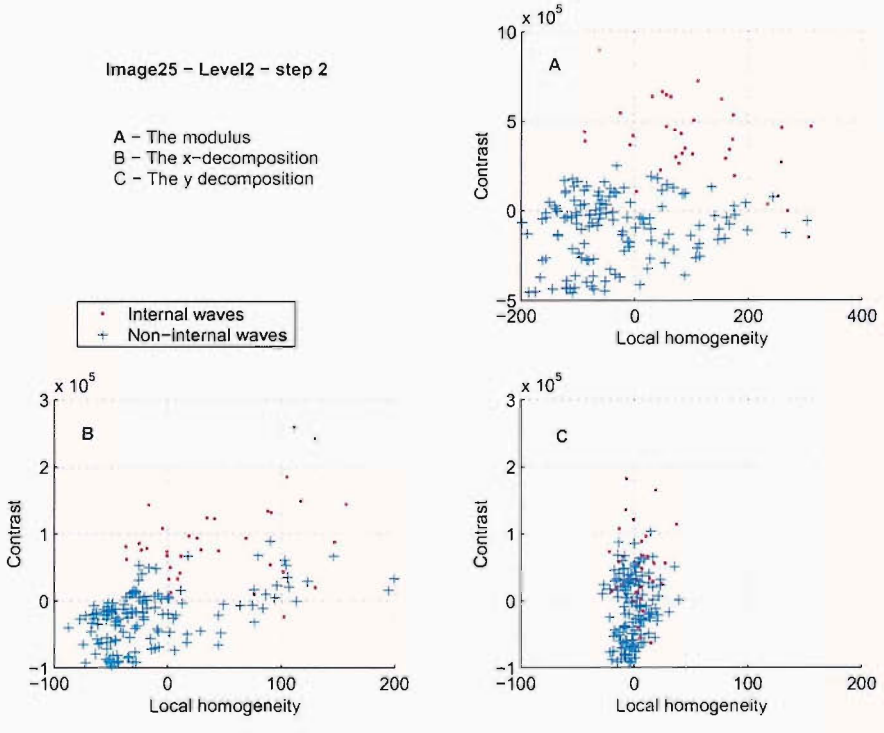

Figure 4.6: Statistical indices for image25 level2 $d = 2$

Chapter 5

The classification

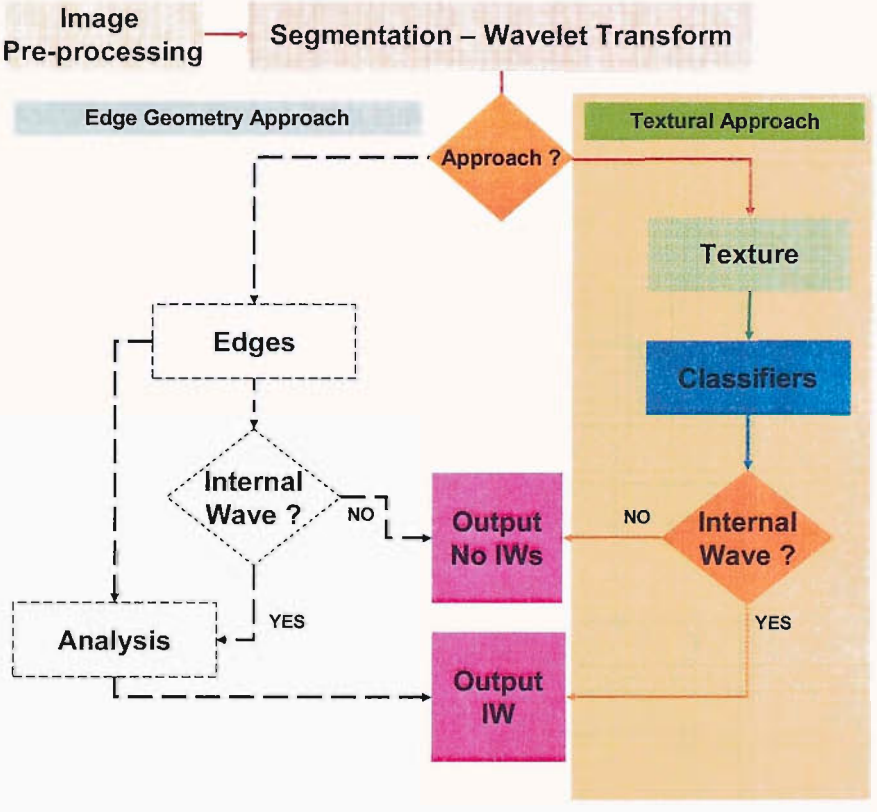

Figure 5.1: Diagram illustrating the layout of the processing

To succeed with the aim of this work, it is necessary to be able to distinguish between the internal wave signature and the background of the SAR images. So far it have been shown that the GLCM and the statistical indexes derived from it, offer the opportunity to present two classes of scatter points: one representing an internal wave signature and the other class the non internal wave signature. In order to automatically separate the two classes the use of a classifier is needed. For this study, initially three types of classifiers were chosen. The first of the three is based on Principal component

analysis (PCA), the second is a K-nearest neighbour (KNN), and the last is a Multilayer perceptron (MLP). The three classifiers used different properties to classify the data sets.

5.1 Principal Component analysis

To perform a recognition of possible internal wave signatures, eigenvalues were calculated from two different training sets representing "event" and "non-event" (the presence of internal wave, and non presence of internal wave) respectively. As the general data set is small both training sets do not exceed 20 examples of subimages. The Principal component analysis was used on two different set of input data. Figure 5.2 and 5.3 show two examples of GLCM of both classes.

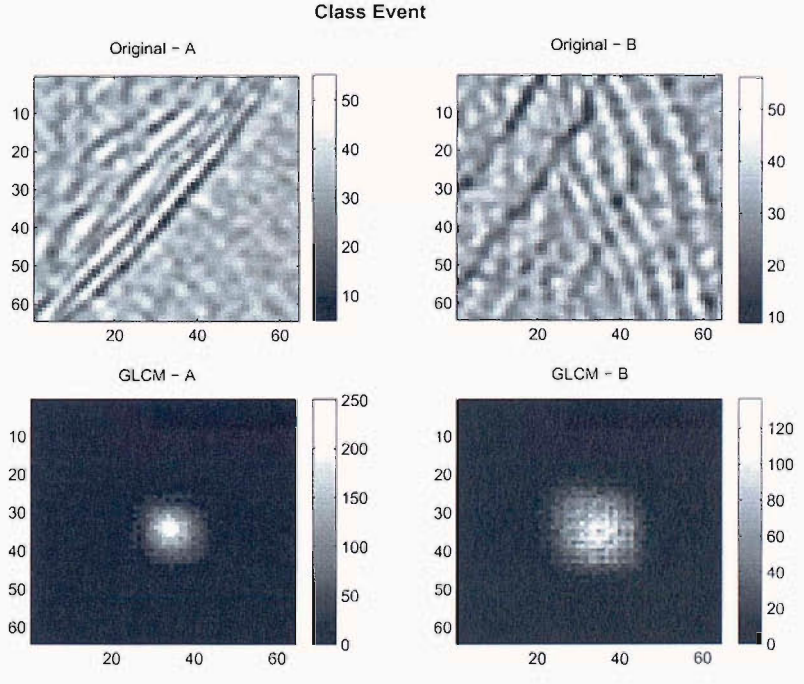

Figure 5.2: Event class: Original image and GLCM ($d = 3$)

5.1.1 Selection technique for the eigenvalue:

Once the eigenvalues from both training sets have been calculated, the same eigenvalues are used to perform a first approximation in the classification of an unknown GLCM. The procedure used is as follow (see figure 5.4 for the schematic representation of the different steps and appendix B for more detail):

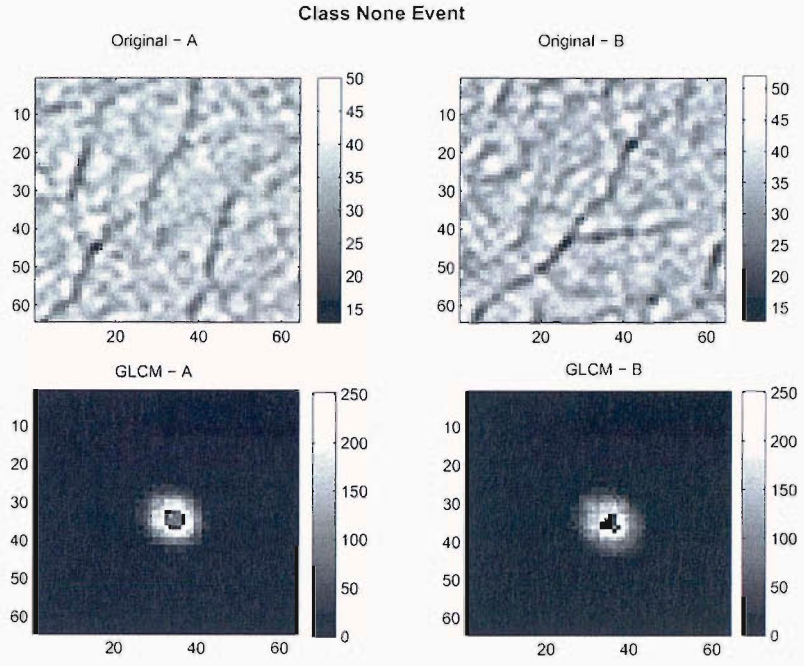

Figure 5.3: Class Non-event: Original image and GLCM ($d = 3$)

- The idea is to calculate the errors between the reconstructed GLCM and the original GLCM using both eigenvalues (5.1.1).
- The first step is to decompose the original unknown GLCM. The decomposition is done for both eigenvalues (event and non-event)(5.1.2).
- The second step is to reconstruct the GLCM. As above the operation is done twice.
- The last step is to calculate the difference between the reconstructed GLCM and its original (5.1.3).

$$\begin{aligned} W_{k(\text{testing set, event})} &= u^T_{k(\text{training set, event})} \times (\Gamma_{(\text{testing set})} - \Psi_{(\text{training set, event})}) \quad (5.1.1) \\ W_{k(\text{testing set,N-event})} &= u^T_{k(\text{training set,N-event})} \times (\Gamma_{(\text{testing set})} - \Psi_{(\text{training set, N-event})}) \end{aligned}$$

$$\begin{aligned} \Gamma_{(\text{reconstructed testing set,event})} &= u_{k(\text{training set, event})} \times W_{k(\text{testing set, event})} + \Psi_{(\text{training set, event})} \quad (5.1.2) \\ \Gamma_{(\text{reconstructed testing set, N-event})} &= u_{k(\text{training set, N-event})} \times W_{k(\text{testing set, N-event})} + \Psi_{(\text{training set, N-event})} \end{aligned}$$

$$\begin{aligned} Diff_{(\text{reconstructed testing set, event})} &= \Gamma_{(\text{reconstructed testing set, event})} - \Gamma_{(\text{testing set})} \quad (5.1.3) \\ Diff_{(\text{reconstructed testing set,N-event})} &= \Gamma_{(\text{reconstructed testing set,N-event})} - \Gamma_{(\text{testing set})} \end{aligned}$$

Where Γ is the GLCM, u the eigenvector, k the number of eigenvalues, Ψ the mean, and W projection of the GLCM into the eigenspace. A result of this operation is shown in

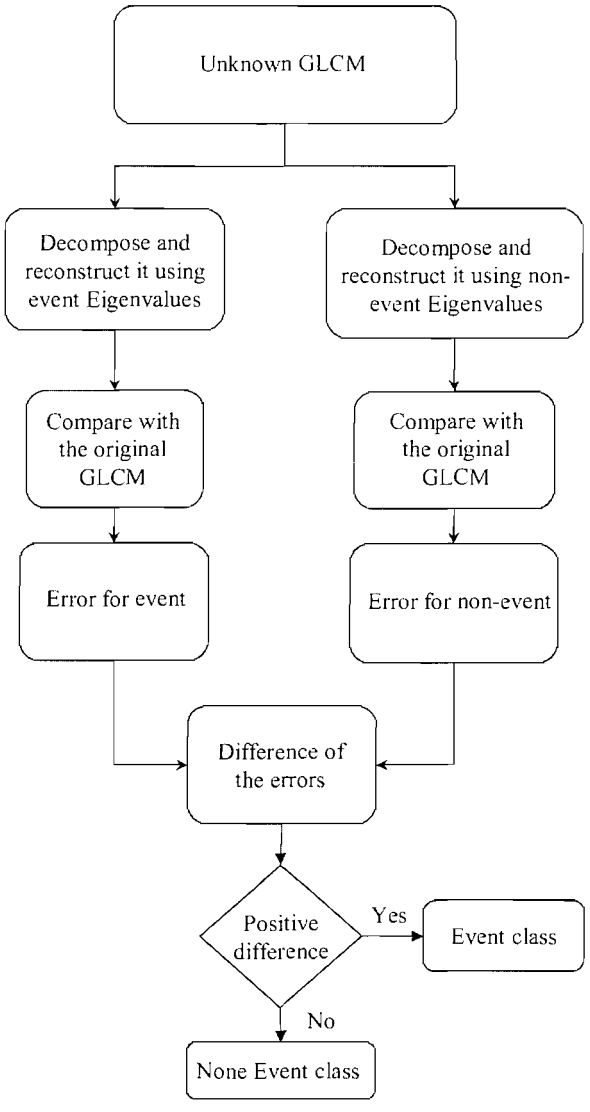

Figure 5.4: PCA classification: the different steps

figure 5.5. To make the result obvious the unknown GLCMs used are the same of those used in the training sets. However in many cases the total error found is a lot smaller and a threshold needs to be used to infer the classification. The use of this threshold creates a problem: each individual classification of a whole image (512x512) requires a different threshold. Furthermore the determination of the threshold is empirical. However the total error value can be used as one more parameter describing the "link" between the GLCM and the different classes.

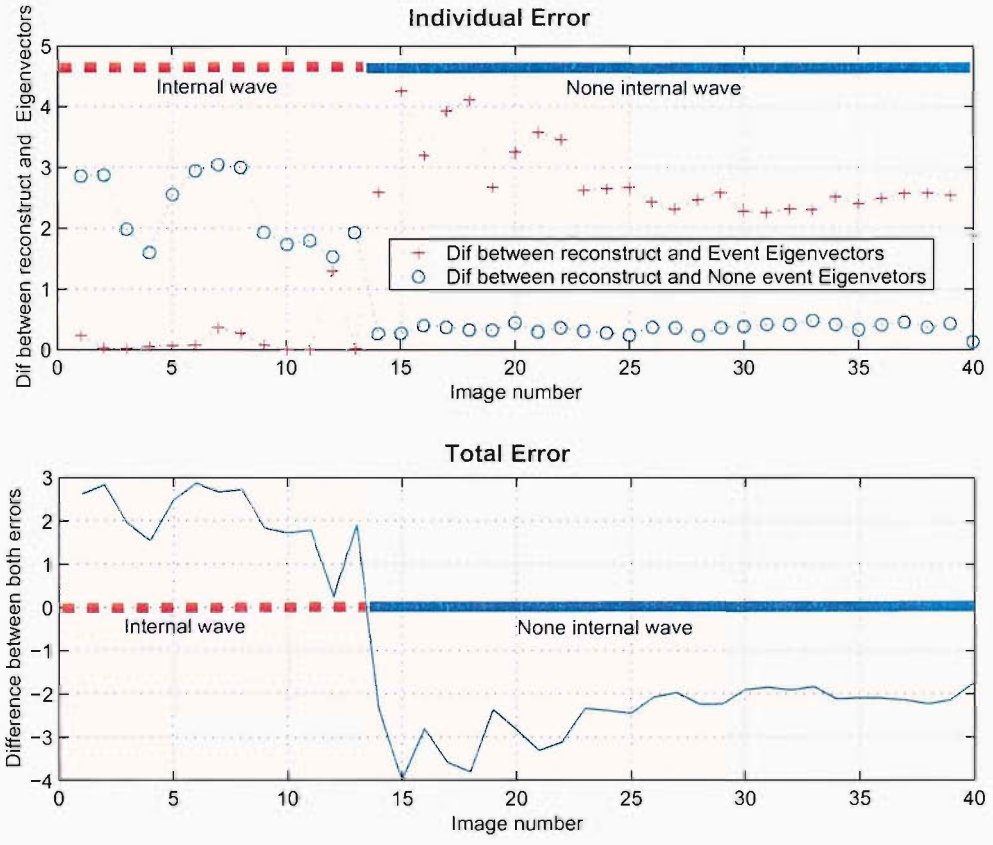

Figure 5.5: Result of discrimination between IW and non-IW event.

5.1.2 Classification using Principal Component analysis

Using the methods described previously a classification of the GLCM can be made. Figure 5.6 is an example of discrimination produced by the PCA technique. To make a distinction between the two classes a threshold has to be applied on the lower plot presented on figure 5.6. The obvious threshold (τ) has to be $\tau = 0$, but in many cases it is not the most effective

To optimize the classification and reduce the influence of the wave orientation different classification combinations are tried out. The combinations are made by using different wavelet representation to improve the IWS / background ratio. Another objective of the optimization is to find a consistent threshold able to classify different SAR scenes. As before the results will be presented for the image0 and the image25.

Results: In order to try to quantify the result, confusion matrices were calculated (see figure 5.11). Three indices are used to quantify the results:

- The total accuracy, which is the ratio between the number of correctly classified

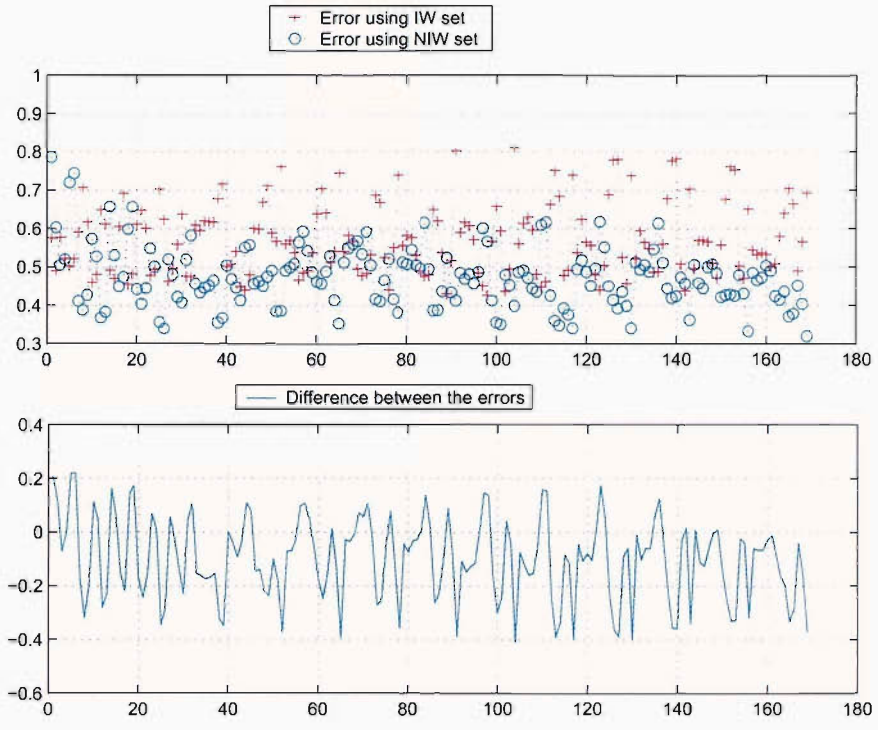

Figure 5.6: Discrimination between IW and non-IW part of the image25

and the total number classified.

- The error on negative detection is the ratio between those negative events wrongly classified and the total number of negative events. This index shows the proportion of negative events misclassified. classified.

- The error on positive detection is the ratio between those positive events wrongly classified and the number of positive events. This index shows the proportion of positive events misclassified.

Figure 5.7 show the accuracy and error of the PCA classification for the images 0 and 25 for different configurations. Of all the possibilities tried, one wavelet representation (level2 mXY for $d = 3, 5$, Figure 5.7(c)) illustrates the difficulty of this approach very well. At first the general classification seems better for the image0 than for image25. In the case of image25 there is large sensitivity to the value of d. For $d = 5$ the total accuracy decreases but the error of missclassification of the two classes is a lot more acceptable than when $d = 3$. The result of the classification of this image for a value of d equal to 5 is shown in figure 5.8. In the case of image0 there is no error in the classification of the internal wave class for both value of d. This has the effect of increasing the total accuracy of the classification. However the problem with this

classification is shown in figure 5.9. The zone of influence of the internal wave in this classification is too large and has produced a very important error in the classification of the non-internal wave class. This error is due to the choice of the threshold. To perform comparative results in this analysis both thresholds have been set to zero. However a better value of the threshold exists for the classification of image0 (threshold= 0.15), which gives the result shown in figure 5.10. In this corrected case the total accuracy is above 85% with an error for the miss-classification of both classes below 10%.

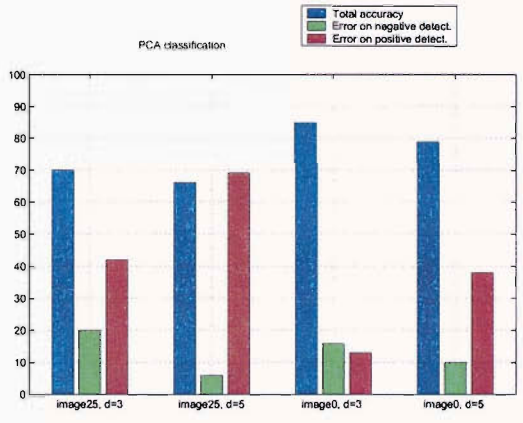

(a) configuration: $M2\ d = 3, 5$

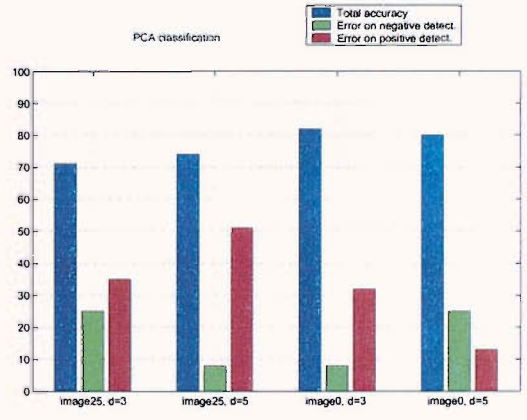

(b) configuration: $XY\ d = 3, 5$

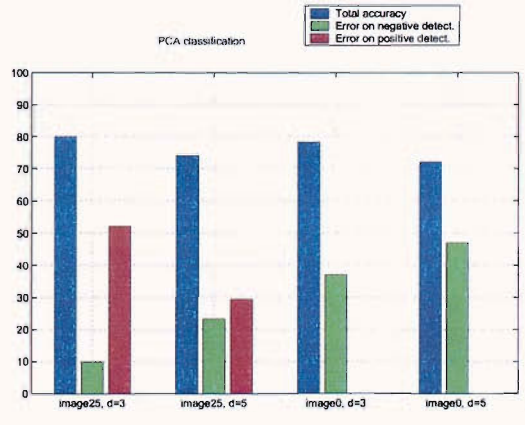

(c) configuration: $mXY\ d = 3, 5$

Figure 5.7: Accuracy results of the PCA classification for level2 and a threshold equal to zero

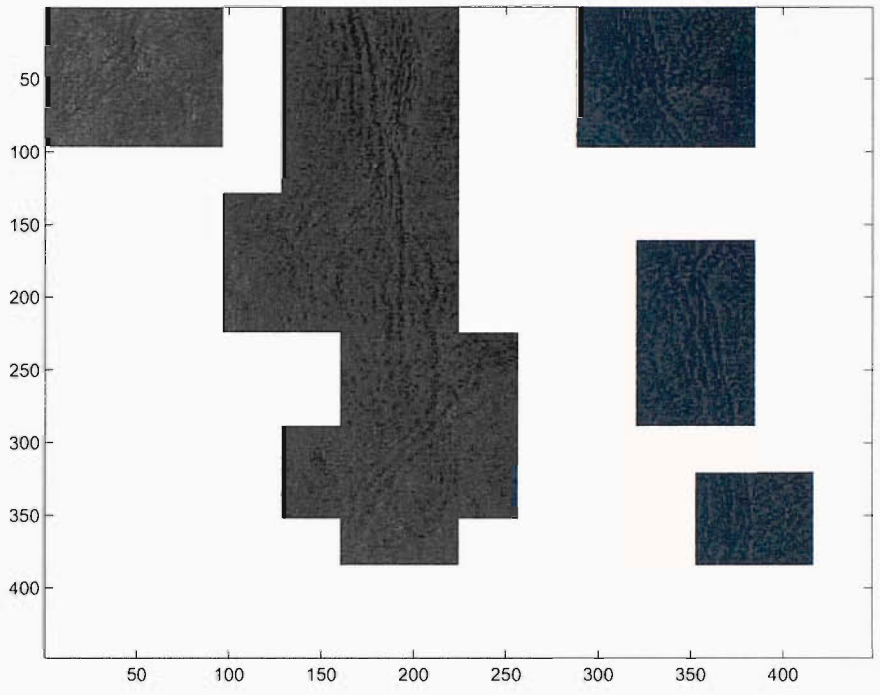

Figure 5.8: Illustration of the PCA classification for image 25 level2 with the configuration mXY, $d = 2$ and a threshold equal to zero (figure 5.7(c))

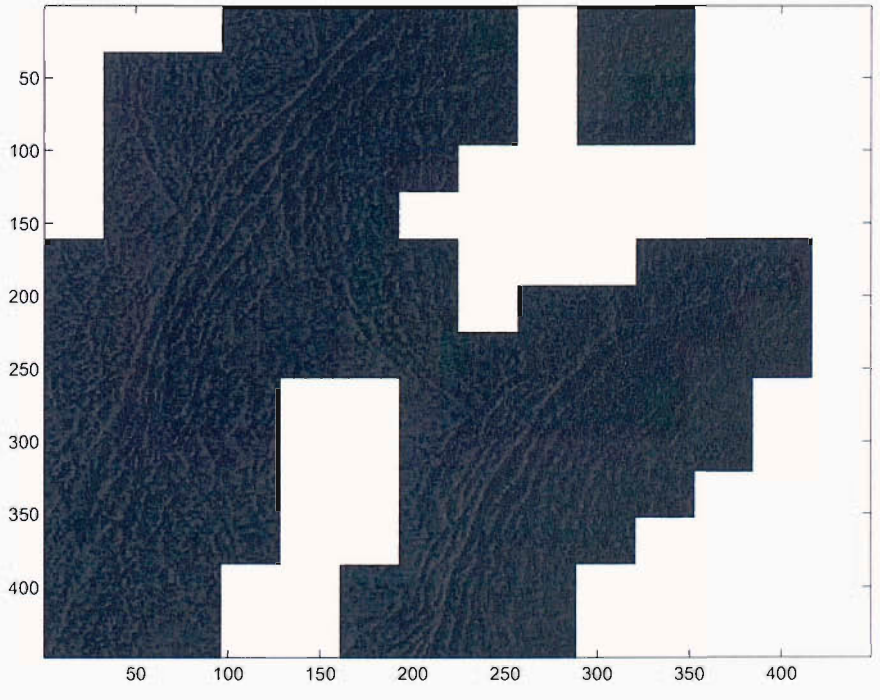

Figure 5.9: Illustration of the PCA classification for image 0 level2 with the configuration mXY, $d = 2$ and a threshold equal to zero (figure 5.7(c))

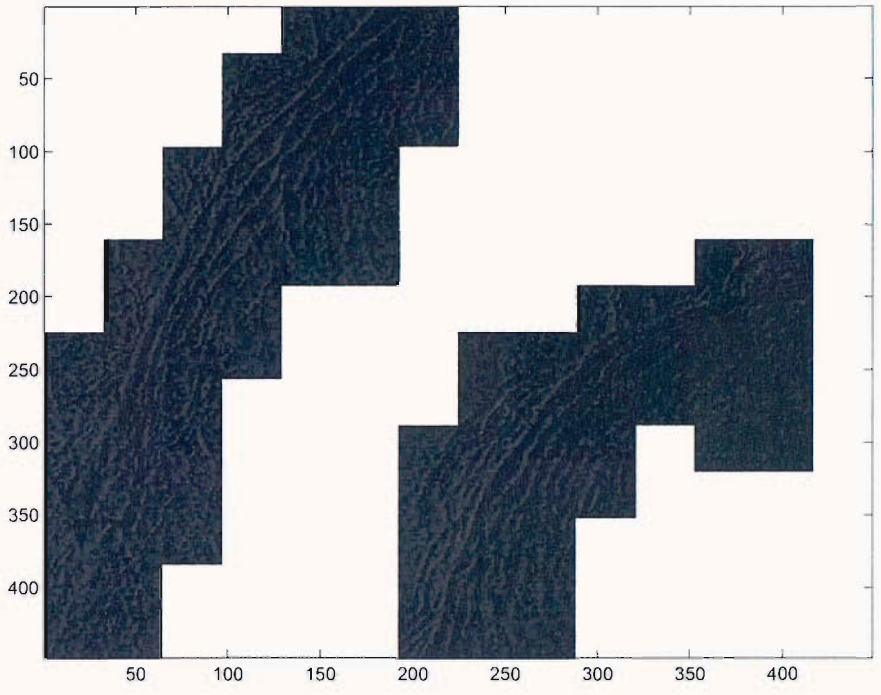

Figure 5.10: Illustration of the PCA classification for image 0 level2 with the configuration mXY, $d = 2$ and a threshold equal to 0.15

Summary For a correct threshold values the PCA classifications performs a good recognition of the internal wave signature. However an accurate classification is highly dependent on the determination of the threshold values. Furthermore a small variation of the threshold gives a large difference in classification accuracy. The need to set a threshold value is a very important drawback of this approach As a method of automatic threshold determination could not be found, this results in a method that is too unreliable to enable a systematic classification method to be adopted.

5.2 K-nearest neighbour

Nearest neighbour methods have been used as an important pattern recognition tool. In such methods, the aim is to find the nearest neighbours of an unidentified test pattern within a hyper-sphere of predefined radius in order to determine its true class [11]. The traditional nearest neighbours rule is shows in table 5.1 [63].

Nearest neighbour methods can detect a single or multiple number of nearest neigh-

- Out of the N training vectors, identify the k nearest neighbours, irrespective of class label. k is chosen to be odd.
- Out of these k sample, identify the number of vectors, k_i, that belong to class w_i. Obviously $\sum_i k_i = k$.
- Assign x to the class w_i with the maximum number k_i of samples.
- If two or more classes w_i, have an equal number E of maximum nearest neighbours, then we have a *conflict.*
- for each classes involve in the conflict, we determine the distance d_i between query set $x = \{x_1, ..., x_n\}$ and class w_i based on the E nearest neighbours found. If the m^{th} training pattern of class w_i involved in the conflict is represented as $y^{i,m} = \{y_1^{i,m}, ..., y_n^{i,m}\}$ then the distance between test pattern x and class w_i is:

$$d_i = \frac{1}{E} \sum_{j=1}^{N} \left| (x_j - y_j^{i,m}) \right|$$

- Assign x to class C if its d_i is the smallest.

Table 5.1: K-NN rules

bours. However the value of k is implicitly dictated by the different classes distribution; if the different classes overlap, more than one nearest neighbours is necessary to produce a classification ($k > 1$).

In order to obtain a representative classification, it is necessary to ensure that the various vectors are statistically different across classes, and the features are statistically independent. If the above condition is not satisfied pre-processing is necessary using techniques such as PCA, which remove the feature dependencies.

The classification of GLCM to enable the positive selection of the presence of internal waves signature over image background and other mesoscale oceanographic features, is

also conducted using a K-nearest neighbour classification technique.
Two different kNNs are used for this classification. The first is a classic kNN as presented in the second chapter. The second method is a variation on the importance of the k nearest vectors. Instead of using the mean between the k chosen vectors to determine the class of the unknown vector; a weight is introduced to favour the nearest vectors from the furthest one. Classifications were carried out using different values for k and d.
A training set and the query set are composed from the statistical indices from the GLCMs. These statistics are normalized in an attempt to reduce the effect of relative difference from cases to cases. The vectors used to make up the training set are from a study showing the presence of internal waves, and manually classified.
The results will be represented as a probability of occurrences of internal waves within a cell of 32x32 pixels (resulting in the overlap of the 64x64 windows) and confusion matrices will be used to derive the accuracy of the classification. The confusion matrices will be constructed by applying a threshold (50%) over the probabilistic answer for both kNN (see figure 5.11).
Note that in the previous section as in this one, two practical cases are shown. These cases are two extremes of the representation of an internal wave on SAR images. The strong differences in the orientation and strength of the signature in the two cases will show up strongly the strength and weakness of the method used.

5.2.1 Results

In order to obtain the best performance from the KNN, it is necessary to have a good tuning: i.e. the correct number of values for each vector, the correct value for K, and an appropriate training set. To obtain the best optimization the following section will present some results as a function of the three parameters describe above. Note that the statistical indices are ordered in the following manner: Entropy, local homogeneity, Correlation, Contrast, Energy, Correlation,and angular moment.

Training set A The training set A consists of the most basic approach. Two case studies (namely image0 and image25) were used. So in this configuration one image is used as training set to classify the other image and vice versa.
The result of the accuracy of this classification is presented in figure 5.12 and figure

5.13 for the image25 and image0 respectively. Like the previous classification the overall result is better for the image0 than for the image25. Another straight forward conclusion is that there no real difference between the result of both kNN used. The results obtained with $d = 3$ and $k = 3$ are in general the best result for a given configuration. The classification for the image25 still contains a very critical miss-classification of the positive part.

One of the internal waves presents in this image has a weak and vertical signature. This internal wave signature is not very well extracted by the wavelet analysis and as a consequence the statistical indices derived from this section are similar to those derived from the section representing the background in the image. This particular internal wave signature can then explain the poor accuracy of the classification in this part of the image.

An examples of the classification of the image25 is presented in figure 5.14(b).

	Non-Evt	Event	
Non-Evt	77	18	80% of total accuracy 18% of error on non-event class
Event	15	60	20% of error on event class

Figure 5.11: Example of a confusion matrix and the derived accuracy. The value are from the classification of image25 with step=2 $k = 2$ for a traditional KNN (figure 5.12)

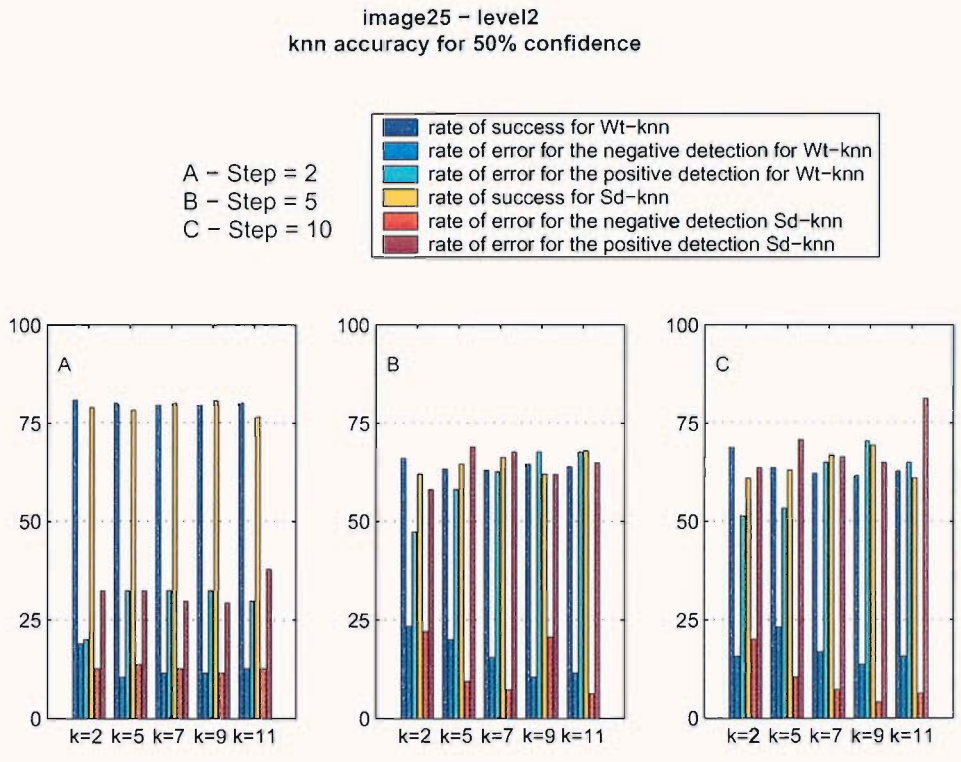

Figure 5.12: Image25 level2 modulus classification: 50% confidence

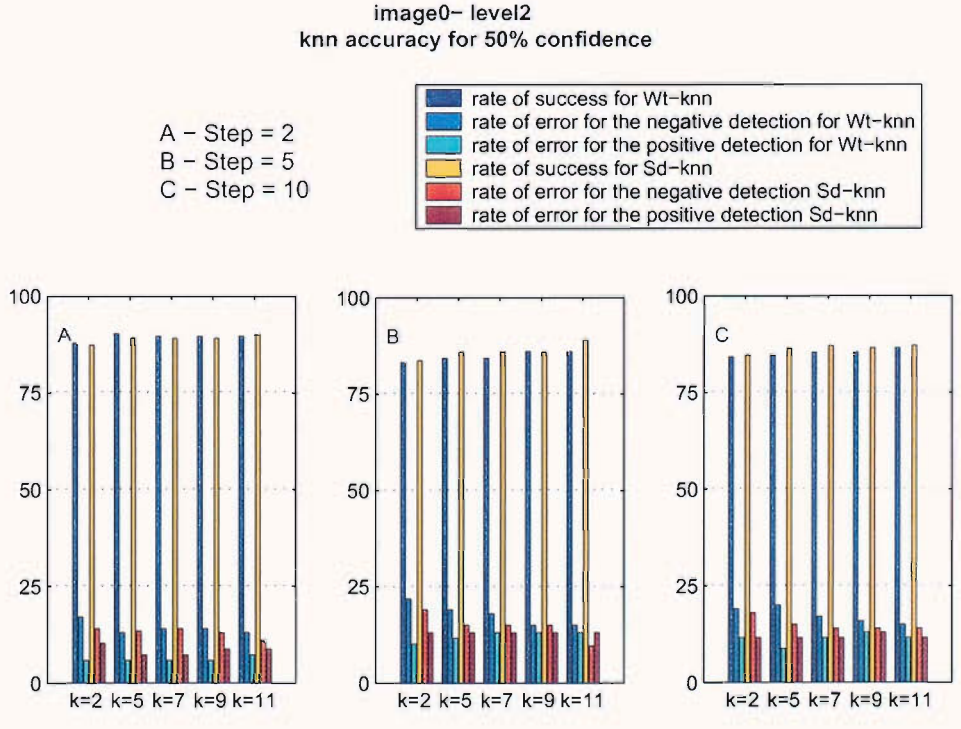

Figure 5.13: Image0 level2 modulus classification: 50% confidence

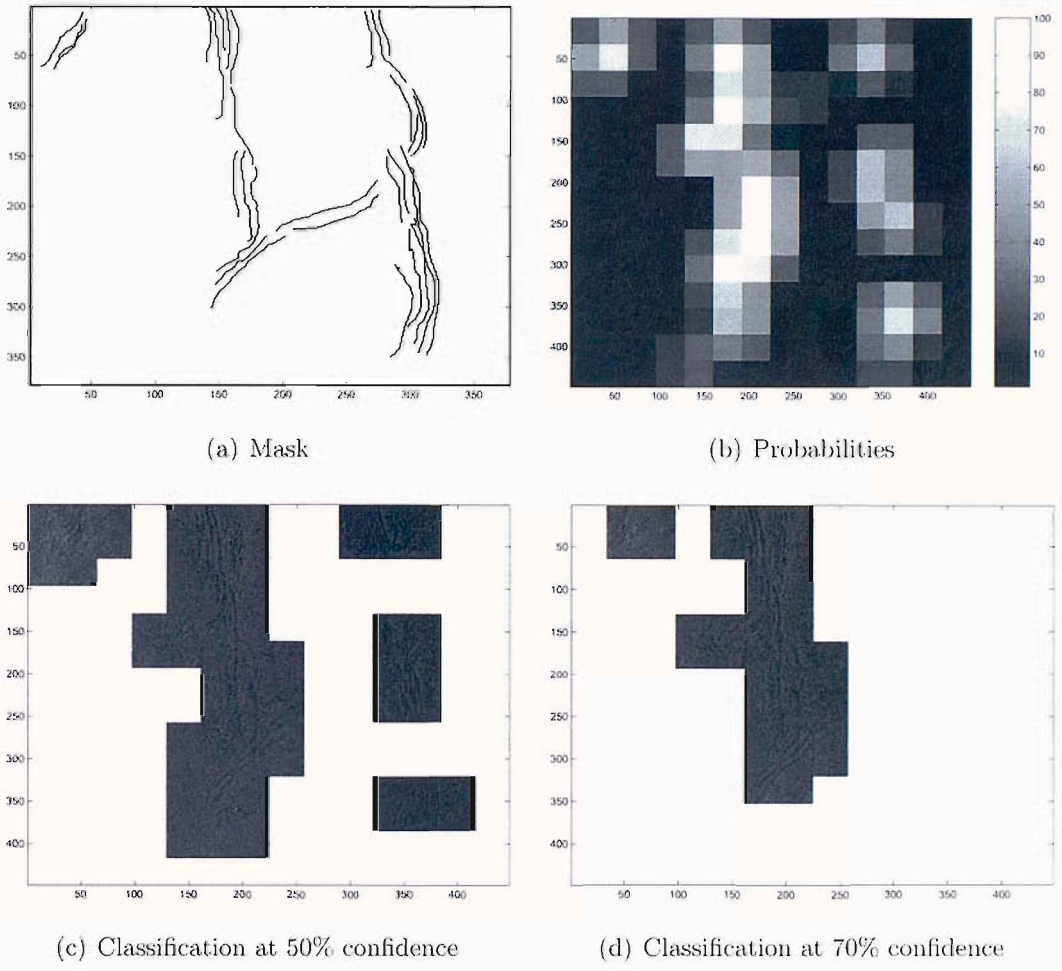

(a) Mask

(b) Probabilities

(c) Classification at 50% confidence

(d) Classification at 70% confidence

Figure 5.14: Image25 level2 modulus classification

Training set B In this case, the training set is made up to 600 vectors representing the two classes with a proportion of around 50% each was used. Each of the vectors was made up from the statistical indexes derived from the GLCM. The results of the classifications are presented for the two case studies with different values of k and d. The first conclusion from the results (table 5.2, 5.3) is that they are worse than for the previous training set. This degradation is especially evident for the image25. However this degradation does not compromise the quality of the data sets, it is a better representation of the different internal waves signature. This training set is more representative of the internal waves signature than the previous training set which was very simplistic. However, a few configurations still give some good results. For example the configuration using the wavelet representation mXY for $k = 3, 5$ and $d = 3$ offers a correct classification for both cases.

It is important to investigate the wavelet representation XY and the influence of k.

Figure 5.15(a) and 5.15(b) show the probability of internal waves presence for the X- and Y-decomposition for image 25 respectively for $k = 3$ and $d = 3$ (namely case 1). The results of the classification are shown in figure 5.16. Figure 5.17(a) and 5.17(b) show the probability of internal waves presence for the X- and Y-decomposition respectively for $k = 7$ and $d = 3$ (namely case 2). The results of the classification are shown in figure 5.18. For both cases the configuration is the same, except that the value of k goes from 3 to 7. For both cases the probability of occurrence of internal wave signature is higher for the X-decomposition than the Y-decomposition. This result underlines again the influence of the internal wave orientation. The value of k become important in the middle left part of the image for the Y-decomposition. At this place the Y-decomposition shown a rough zone. In this region the interpretation depends on the value of k that is used. As this zone is complex, the KNN need a large value of k to be able to give a good classification.

The tables 5.2, 5.3 present the overall results for different number of the input vectors used to classify each sub-images: $2-4-6$: Two input values represent the entropy and the local homogeneity, four input input values represent the first two plus the contrast and the energy and six input values represent the previous four plus the correlation and the angular moment. The result show that the set with up to four input values is the best, which mean that the statistical indexes used in this configuration are the best to represent the two classes.

The best configuration, i.e. the correct parameterisations of the k, d, and the wavelet representation, is the wavelet representation mXY for $k = 3,5$ and $d = 3$. This setup works for both images and therefore will be the one to be retained in the application chapter. Figure 5.19(a), 5.19(b) and 5.20(a), 5.20(b) show the classification using this setup for both case studies.

Summary In general the KNN offers a better classification than the previous technique used. The improvement is based on the fact that the configuration can be fixed and therefore the classification is independent of any further adjustment. To conclude the retained setup is as follow:

- Choice of the training set:
  - Training B. It is a broader representation of the signature in the SAR images
- Choice of the KNN (Normal or weighted):

  - weighted

- Choice of the k:

  - $k = 3$

- Choice of the input vector:

  - input vector length is equal to 2 and 4

	K=3 - Step=3									K=3 - Step=5								
	Input=2			Input=4			Input=6			Input=2			Input=4			Input=6		
	M2	mXY	XY	M2	mXY	XY	M2	mXY	XY	M2	mXY	XY	M2	mXY	XY	M2	mXY	XY
Total accuracy	81.3	80.0	68.8	73.7	81.3	66.6	75.5	80.4	79.5	77.3	72.8	62.2	66.6	72.9	61.7	71.1	72.8	65.5
Event error	39.2	23.2	8.9	33.9	16.0	5.3	32.1	19.6	57.1	37.5	32.1	12.5	35.7	28.5	8.9	39.2	26.7	8.9
N-Event error	11.8	18.9	38.4	23.6	19.5	42.6	21.8	19.5	43.2	17.7	25.4	46.1	32.5	27.2	47.9	25.4	27.1	43.2
	K=5 - Step=3									K=5 - Step=5								
Total accuracy	81.3	84.8	70.2	76.4	84.4	67.1	78.2	80.8	66.6	73.3	76.4	62.6	66.6	72.0	62.2	73.3	74.6	66.2
Event error	39.2	28.5	8.9	32.14	21.4	7.1	30.2	21.4	10.7	33.0	33.9	12.5	32.1	28.5	10.7	33.9	23.2	12.5
N-Event error	11.8	10.6	36.6	20.7	13.6	41.4	18.9	18.3	40.8	18.0	20.1	45.5	33.7	27.0	46.7	24.2	26.0	40.8
	K=7 - Step=3									K=7 - Step=5								
Total accuracy	83.1	84.4	88.4	76.0	82.6	83.5	74.2	76.0	77.3	78.6	76.4	64.8	68.4	71.1	65.3	74.6	72.0	66.6
Event error	28.5	28.5	14.2	32.1	21.4	14.2	30.3	21.4	14.2	32.1	33.9	12.5	32.1	30.3	10.7	32.1	25.0	12.5
N-Event error	13.0	10.6	10.7	21.3	15.9	17.1	24.8	24.8	25.4	17.9	20.1	42.6	31.3	28.4	42.6	23.1	28.9	40.2

Table 5.2: Result of the classification performed by the KNN of the Image25 for a variety of different values of d and k.

	K=3 - Step=3									K=3 - Step=5								
	Input=2			Input=4			Input=6			Input=2			Input=4			Input=6		
	M2	mXY	XY	M2	mXY	XY	M2	mXY	XY	M2	mXY	XY	M2	mXY		M2	mXY	XY
Total accuracy	74.2	83.1	62.2	73.7	82.6	62.3	76.4	79.9	59.1	78.2	84.4	68.4	77.7	84.4	63.4	75.5	82.6	65.3
Event error	29.8	10.3	3.5	15.7	8.7	0.0	15.8	14.3	1.7	28.0	14.2	3.5	15.7	12.28	3.5	21.0	14.0	1.7
N-Event error	24.4	18.4	49.4	29.7	20.3	50.9	26.1	23.4	54.1	14.6	16.0	41.0	24.4	16.0	48.0	25.5	18.4	45.8
	K=5 - Step=3									K=5 - Step=5								
Total accuracy	79.5	82.2	60.4	76.0	82.6	63.1	78.2	75.5	62.2	79.5	85.3	65.7	78.6	84.0	66.6	78.2	84.0	67.5
Event error	21.	10.5	1.7	14.0	10.5	1.7	15.7	12.2	1.7	22.8	15.7	1.8	14.	12.2	1.8	17.5	12.8	1.8
N-Event error	22.2	20.3	52.3	27.8	19.6	48.8	23.8	23.2	50.0	19.0	14.28	44.0	23	17.2	45.2	23.2	17.2	42.8
	K=7 - Step=3									K=7 - Step=5								
Total accuracy	81.7	83.1	77.3	80.4	82.2	76.8	79.1	79.5	74.8	79.5	85.8	66.6	79.5	84.8	67.5	79.1	83.5	68.4
Event error	35.0	10.5	1.75	15.8	10.5	3.5	14.0	10.5	24.5	19.2	14.0	1.75	14.0	8.7	1.7	17.5	12.2	1.7
N-Event error	12.5	19.0	29.7	20.8	29.7	29.7	23.2	23.8	33.3	20.8	14.8	44.4	22.6	17.2	42.8	22.0	17.8	42.7

Table 5.3: Result of the classification performed by the KNN of the Image0 for a variety of different values of d and k.

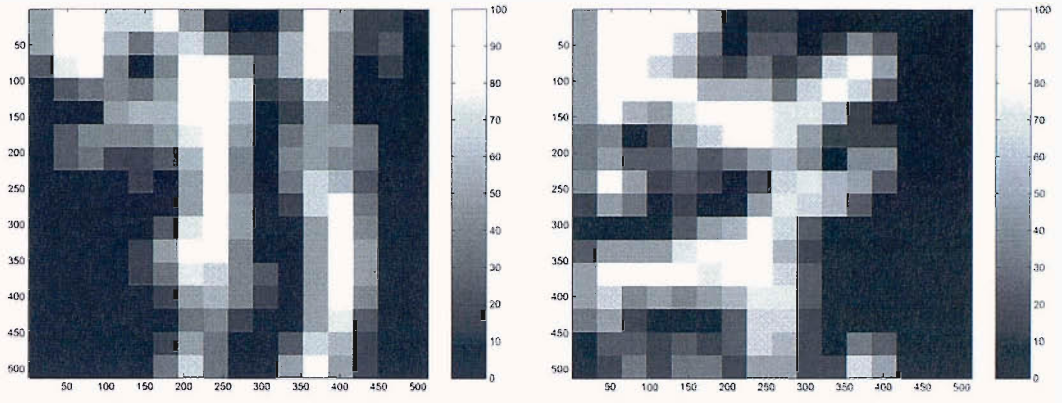

(a) Classification for X-decomposition (b) Classification for Y-decomposition

Figure 5.15: KNN output for k=3 using the X and Y configuration of the image25

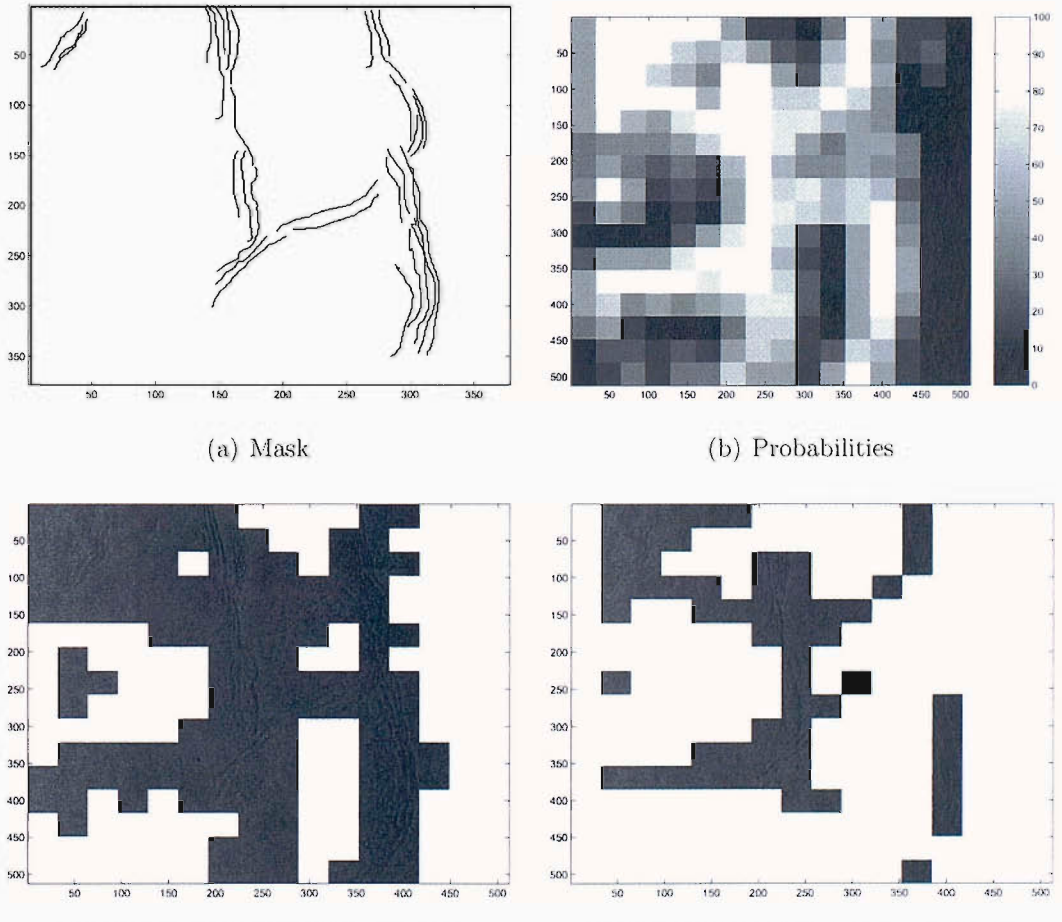

(a) Mask (b) Probabilities

(c) Classification at 50% confidence (d) Classification at 70% confidence

Figure 5.16: KNN output for k=3 using the XY configuration of the image25

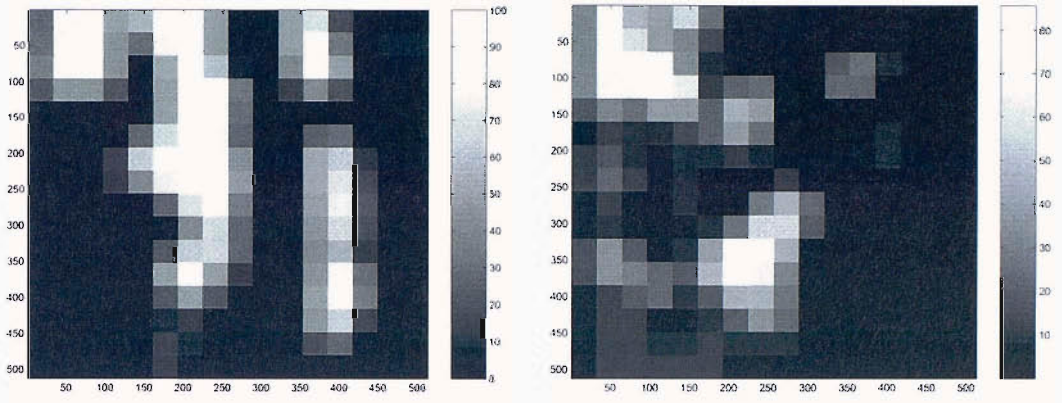

(a) Classification for X-decomposition (b) Classification for Y-decomposition

Figure 5.17: KNN output for k=7 using the X and Y configuration of the image25

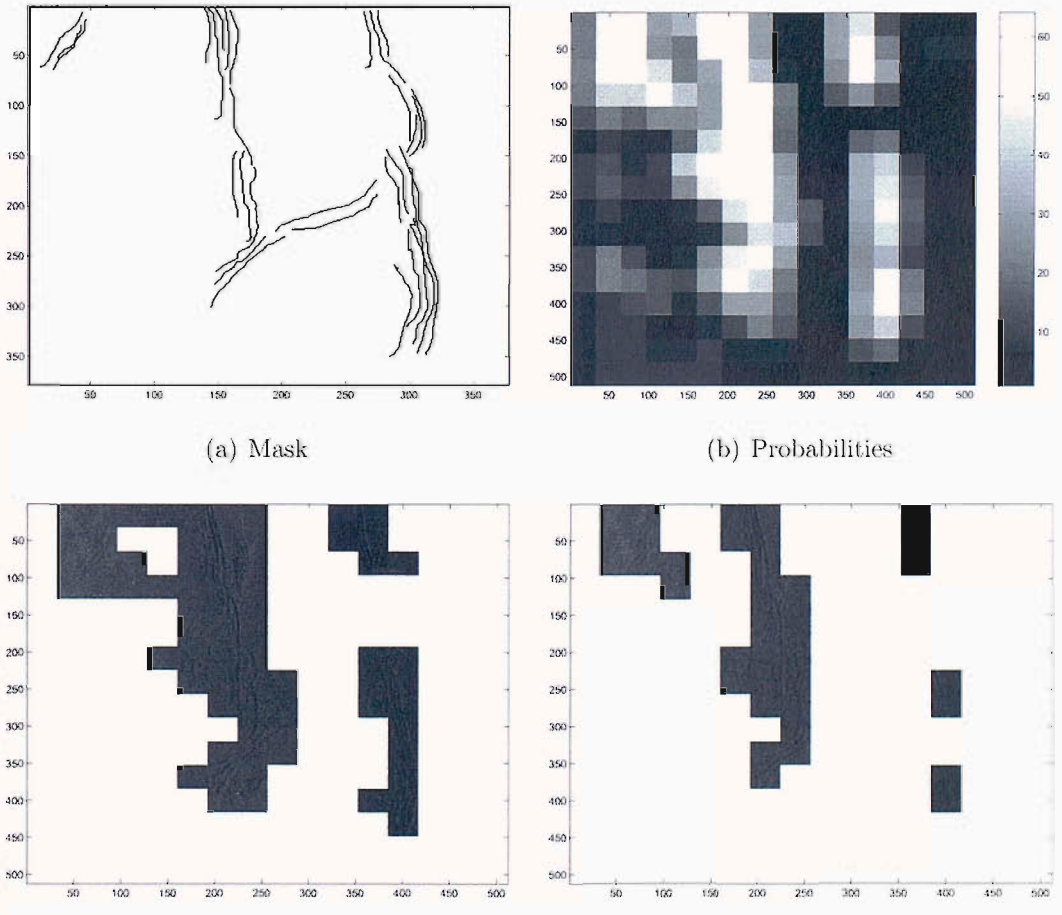

(a) Mask (b) Probabilities

(c) Classification at 50% confidence (d) Classification at 70% confidence

Figure 5.18: KNN output for k=7 using the XY configuration of the image25

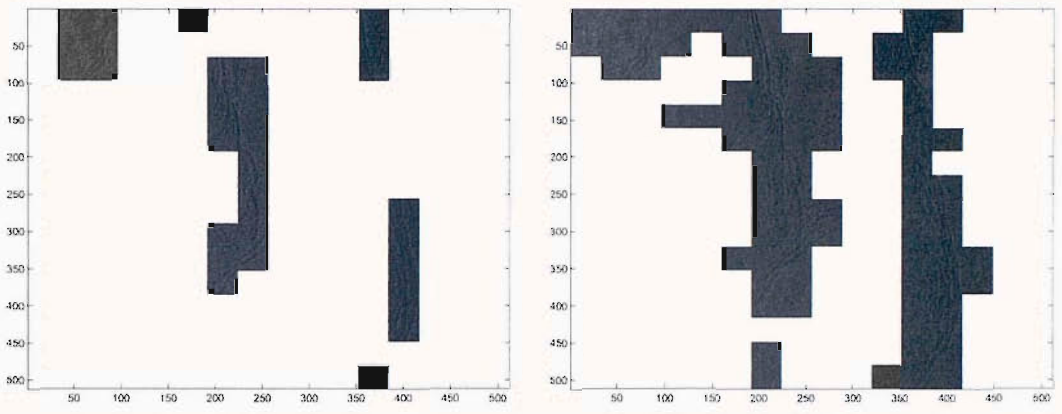

(a) Classification at 50% confidence (b) Classification at 70% confidence

Figure 5.19: Result of the KNN classification of the image 25 for k=3 using the wavelet representation mXY.

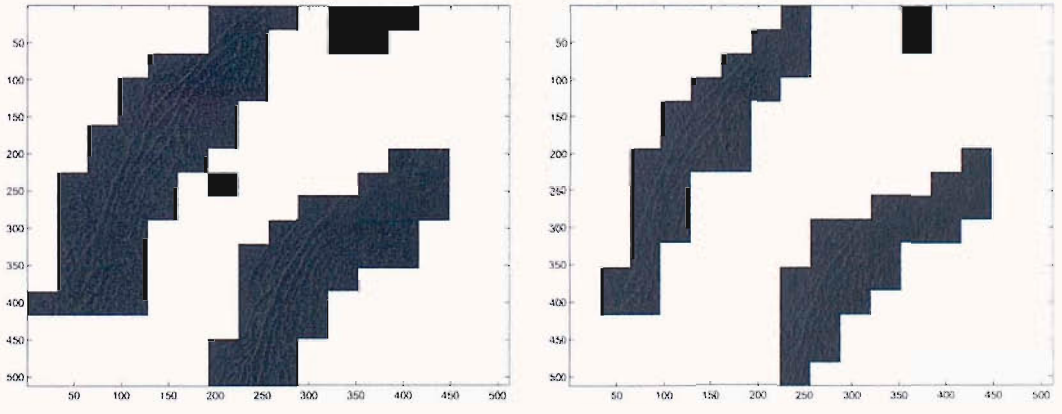

(a) Classification at 50% confidence (b) Classification at 70% confidence

Figure 5.20: Result of the KNN classification of the image 0 for k=3 using the wavelet representation mXY.

5.3 Multi-Layer Perceptrons

Artificial Neural Network models have been studied for many years in the hope of achieving human like performance in the field of speech and image recognition. The different abilities of neural network have attracted many people to use it for remote sensing applications [17], [18].

The traditional parametric statistical approaches to supervised classification such as maximum likelihood use the assumption of a multivariate Gaussian distribution. Each class in feature space is assumed to have an n-dimensional multivariate Gaussian distribution. With these methods a problem appears when the data in the features do not follow the assumed model.

In the Neural Network approach the problem with the assumptions do not exist and they potentially have the ability to classify data with a better efficiency [37]. Neural Networks applied for supervised classification are similar to the K-nearest neighbour algorithm. The main advantage with the use of the Neural Network approach is there is no model or distribution assumed at the start.

Many types and architectures of Neural Networks have been developed [22]. The most popular architecture for pattern classification and recognition is the multi-layer perceptron (MLP). The developments of the neural network techniques were specially due to the increasing in computing power in the 1980's. New types of architecture and technique were developed such as the back-propagation MLP algorithm described by Rumelhart [57].

5.3.1 MLP Structure

A neural network consists of a number of interconnected nodes. Each node is a simple processing element that responds to the weighted input it receives from other modes. The arrangement of the nodes is referred to as the networks architecture (see figure 5.21).

The resolution of a non-linear problem asks for a multi-layer structure such as the MLP. The multi-layer structure is composed of 3 layers at least (see figure 5.21).

The design procedure for neural network pattern classifiers involves the following step:

- Define correctly the input and output of the network as well as a suitable structure for the particular problem involve.

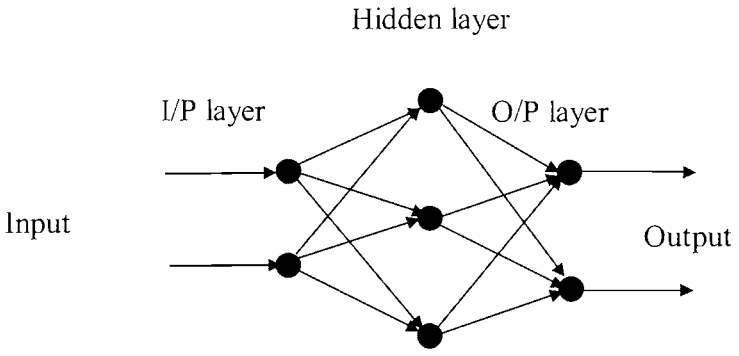

Figure 5.21: MLP layout

- Choose a good training method for the structure of the network. It is important Select carefully the training set as well as the training time.
- Find a good compromise between the training set the training time and the number of nodes, in order to provide high accuracy and good generalization.

These choices are very important for the performance of the network, but the determination of a good general structure is difficult.
The feed-forward network is composed of a hierarchy of processing unit, organized in a series of two or more mutually exclusive sets of layers. The layer serves as a holding site for the values applied to the network; the nodes are the element of a feature vector, such as the texture of an image or the wavebands of a data set, etc [14]. The last layer is the point of final state of the network is reading. Between these two layers lies zero or more layers of hidden unit (hidden layer). Weights connect each unit in one layer to those in the next layer (there is no feedback).
The role of the input layer is somewhat fictitious, the input layer is used only to feed the network and distribute a separate mapping or conversion of the input data (their weights are insignificant).

The MLP has a feed forward propagation; the information is passed through the network via the input layer and it is modified by the weights associated with the connection. The receiving node sums the weighted signals from all nodes to which it is connected in the preceding layer as follows:

$$Net_j = \sum W_{i,j} o_j \tag{5.3.1}$$

Where $W_{i,j}$ represents the weights between node i and node j, and o_i is the output from node i. The output from a given node j is:

$$o_j = f(net_j) \tag{5.3.2}$$

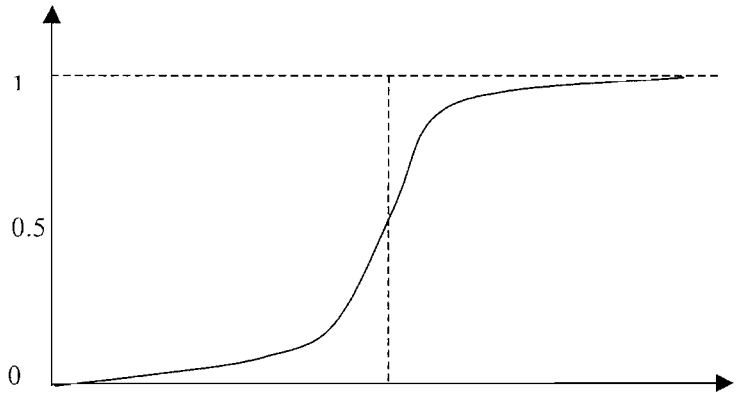

Figure 5.22: Example of a sigmoid function

The function f is a non-linear sigmoid function (see figure 5.22). The sigmoid function is applied to the weighted sum of input before the signal is passed to the next layer. When the signal reaches the output layer it forms the network output. The output of one node is set to one, while all other nodes in the output layer are equal to zero.
The MLP is trained to recognize particular patterns. During this training the network builds a model to generalize and predict the output from a given input. The back-propagation is a method widely used. During the training period the output signal is compared to the output desired then an error is deduced. The error is reinjected in the network, and the weights of the connection are modified according to the generalized delta rule. This process is repeated until the error reaches an acceptable value.

$$\Delta W_{ji}(n+1) = \eta(\delta_j o_i) + \alpha \Delta W_{ji}(n) \tag{5.3.3}$$

η is the learning rate of the network, δ_j is an index of the rate of change of the error, and α is the momentum parameter.
The capabilities of the neural network to be accurate, to generalize and to interpolate, are affected by many factors. The first factor and maybe the most important and most difficult to determine is the number of layers and nodes in the network. In general the number of nodes in the hidden layer increases the abilities of the network to solve complex situation but its abilities to generalize decrease. The size and the type of the

training set is also very important. The training set has to be representative of the entire distribution of each class. To obtain an overview of the class, a large training set is required, and then the training time is increased. A few methods have been developed to compress the training time such as the delta-bar-delta rule or optimization procedure [10],[50]. Increasing the training set increases the training time. The longer the network is trained the more accurate it becomes but its ability to generalize decreases. There is then a compromise to find between the training set, the architecture and the training time required to optimize the network.

Training is accomplished by presenting the pattern to the network and determining the output. The actual output of the network is compared to the target and an error is derived. The error calculated is propagated backward through the network and used to change the weight within the net. This process is repeated until the error reaches an acceptable value. This training method is known as the back-propagation training method. The number of hidden layers needed and the number of nodes in a hidden layer is possibly one of the most difficult questions related to multi-layer networks. No methodology have been found yet in order to determine these variables [30]. However Foody [25] shows that the complexity of a given problem has to be the main driven factor into the chose of the MLP's architecture.

5.3.2 MLP Training and Back-propagation

Once the appropriate neural network structure has been chosen, the training strategy has to be selected. Often during a training period the error does not converge, becomes unstable or oscillates between two minima. This situation necessities some adjustment in considering the following training parameters:

- Training using pattern or epoch;
- Use of momentum and corresponding weight
- Learning weight and weight changes over time
- Sequential vs. random ordering of training vector
- Determining whether the training algorithm is stuck at a local energy minimum

In many applications, it is advantageous to consider modifying the neural node characteristic to include a bias. For example with the sigmoid function which give

$f(0) = 0.5$ for $net_i = 0$. We may wish to bias this node such as $f(0)$ is another value. This bias may also be part of the training. A simple model for the unit with bias is to modify net_i such as:

$$net_j = \sum_i W_{ij} o_i + bias_j \tag{5.3.4}$$

The Generalized Delta Rule is a product-learning rule for a feedforward, multiple-layer structured neural network that uses gradient descent to achieve training or learning by error correction. The network weights are adjusted to minimize the error based on the difference between the actual output and the desired output. The basic operations of the GDR are:

- Apply input vector to the network
- Propagate the input pattern in the network to determine the node output
- Compute and propagate error measure backward through the network
- Minimize the error at each stage through the node weight adjustment

Each element of the network has its own terminology:

- i: the input pattern
- o: corresponding output pattern or response (vector)
- w: network weight associated to the node-node connection
- t: desired system output

Note that weight w_{ji} denote the strength of connection from node i to unit j.

Back-propagation

For this presentation of the different steps, a 3 layer MLP s assumed.

- Present i^p from output o_i of all units in network.
- Use the expression $\Delta^p W_{ij} = \varepsilon \left(t_j^p - o_j^p\right) f_j' \left(net_j^p\right) \tilde{o}_j^p$ to update W_{ij} for the output layer.
- Use the expression $\Delta^p W_{ij} = \delta_j^p \tilde{o}_j^p \varepsilon$

(Pattern) Error Measure	$E_P = \frac{1}{2}\sum_j \left(t_j^p - o_j^p\right)^2$
(Pattern) Weight correction	$\Delta^p W_{ij} = \delta_j^p \tilde{o}_j^p \varepsilon$
Output unit	$\delta_j^p = \left(t_j^p - o_j^p\right) f_j\left(net_j^p\right)$
Internal units	$\delta_j^p = f_j\left(net_j^p\right) \sum_n \delta_n^p W_{nj}$
Output derivative (Assume sigmoidal characteristics)	$f_p\left(net_j^p\right) = o_j^p\left(1 - o_j^p\right)$

Table 5.4: Summary of the GDR equations for the training using the Backpropagation technique

The method above suggests that a care must be taken in choosing the learning rate, which is, in a gradient approaches, define as:$\varepsilon(n) = \varepsilon_0/n$. To add momentum at each iteration, we can modify the correction parameter as follow:

$$\Delta^p W_{ij}(n+1) = \delta_j^p \tilde{o}_j^p \varepsilon + \alpha \Delta^p W_{ij}(n) \tag{5.3.5}$$

The expression corrects the correction term (n+1) using a product of a factor α and the correction term (n). This method can prevent oscillation in the system.

5.3.3 Results

The MLP needs like the KNN, a training set. To offer a valid comparison, the same training set is used here. The construction of the training set for an MLP has to follow a few rules. For example Pankiewizc [49] stipulates that two thirds of the data set has to be used for training purpose and the rest for validation. A recommendation by Tovinkere [65] stipulates that the number of training per classes should be up to 20 times the number of classes. The list of recommendation is large see [37] and [8] for more detail. To be able to follow these rules and to simplify the processus, the data set was created using 10 different images representing around 600 sample with a repartition of 50% between classes. The validation is provided using the two case studies: image0 and image25.

There are two steps in the construction of an MLP. The first is to determine how many hidden layers will be used and the number of nodes. The second step is the number of inputs that will offer the best configuration. To perform this construction the result will be given using the average between the validation using image0 and image25.

Number of hidden layer and their sizes: For this purpose a series of MLPs were built using different numbers of hidden layers and numbers of nodes. Each MLP was trained for 600 iterations and validated using the two case studies. It became obvious that the case with one hidden layer was desirable for the small training time and the accuracy of the classification. Figure 5.23 show the result for an MLP with two input nodes, one output and different number of nodes in the hidden layer, expressed as the mean square error calculated at each iteration . The graph show a minimization of the error for 12 nodes in the hidden layer.

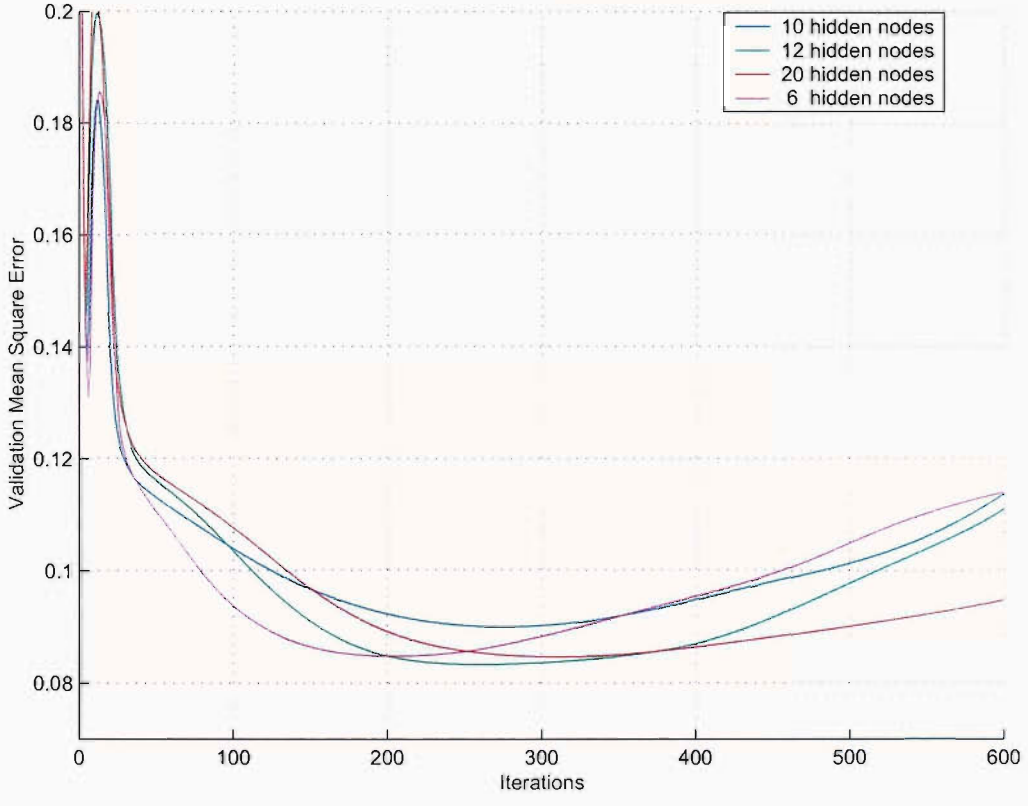

Figure 5.23: Mean Square error for number of node in the hidden layer.

Number of input: For this purpose, the previous result with a MLP with one hidden layer of 12 nodes and one output is used. Three new MLPs were constructed using this parameterisation with $2-4-6$ input node respectively. They were trained independently for 600 iterations and validated using the two case studies. The result can be seen in figure 5.24, with the mean square error calculated at each iteration. The graph show a minimization of the error with a value of 0.08 for 6 input nodes between 250 and 300 iterations.

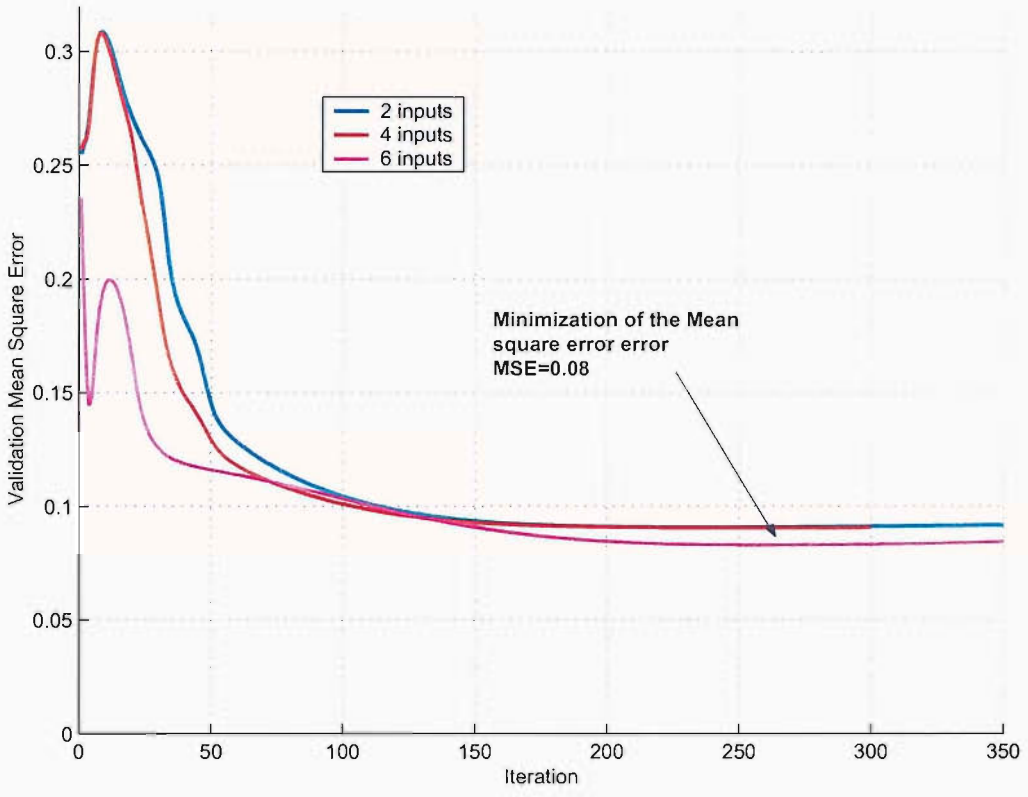

Figure 5.24: Mean Square error for different number of input nodes

Validation results: The MLP used has 6 input nodes where the statistical index are introduced into the network, one hidden layer with 12 nodes and one output node. The results are presented for the two case studies and for different values of d (see table 5.5).The overall results have a better accuracy than for the two previous classifier used, even for the case of image25 which exhibits a good classification. The improvement is significant for every values of d and for every wavelet representation.

As in the previous classification it is important to look at what is happening for the wavelet representation XY, for two reasons: because highest accuracy is reached for the wavelet configuration with a value of d equal to 3, which was not the case in the classification using as KNN; and to see if the problems occurring for the KNN classification still exist. Figure 5.25(a) and 5.25(b) show the probability of occurrence of internal wave for the X- and Y-decomposition respectively. As before, the classification of the X-decomposition offers a good identification of the classes. In the classification of the Y-decomposition, the left middle part of the image shows the highest values of probability. However, the probabilities shown in figure 5.25(b) are small (less than 50%), which do not compromise the result of the X-decomposition and therefore give a

	Image 0			Image 25		
	Step=3			Step=3		
	M2	mXY	XY	M2	mXY	XY
Total accuracy	83.3	84.8	84	83.1	87.1	92
Event error	1.7	7.0	5.2	10.7	25.0	5.3
N-Event error	22	17.8	19.0	18.9	8.8	8.9
Step=5				Step=5		
Total accuracy	87.1	85.7	83.1	77.3	78.1	85.7
Event error	8.7	5.26	1.75	35.7	28.1	3.5
N-Event error	14.2	17.2	22	18.3	18.3	17.7

Table 5.5: MLP classification results

correct overall classification (Figure 5.26). Figure 5.27(a), 5.27(b) show the probability of occurrence of internal wave for the X- and Y-decomposition respectively, for image 0. In this case the two signatures are mainly orientated diagonally in respect to the image coordinate with one extremity of the smaller wave orientated horizontally. These differences are well observable in the repartition of the probability of occurrence in the figure 5.27(a), 5.27(b), which as for the image 25 give an overall better classification. Now a comparison can be made with the best wavelet configuration for the KNN classification, which is the wavelet representation mXY. Figure 5.29 and 5.30 show the result of the classification for the image0 and image25 respectively. The results for the first case study (image0) are good and give a good representation of the signature of the internal wave within the image for both thresholds: 50% and 70%. In the case of the image25 the story is a bit different. The signature of the right hand side of the image is completely miss-classified. This missclassification comes from the fact that this wavelet representation is the mean between the x- and y-decomposition. As this signature is horizontally oriented, it is not detected in the y-decomposition, therefore it is weakly represented in the mean between the two decompositions and therefore the MLP does not succeed in classifying this zone properly.

Summary In general the MLP offers an overall better classification than the previous techniques described. The setup of the MLP was chosen for a good compromise between

the accuracy of the classification and a quick training time. To conclude the preferred configuration is as follow:

- Choice of the training set:
  - Training B. It is a broader representation of the signature in the SAR images
- Choice of the number of hidden layer and their number of nodes:
  - One hidden layer with 12 nodes
- Choice of the number of input:
  - number of input = 6
- Best wavelet representation:
  - XY

5.4 Conclusion

This chapter presented three classifiers to tackle the problem of the classification of the internal wave signature in SAR images. The information contained in the GLCM and statistical indices are used to discriminate between two classes (event and non-event), using a PCA technique, two different KNN classifiers, and a MLP classifiers. The PCA classification technique used the GLCM directly, while input to the KNN and the MLP are statistical indices.
The recognition technique was applied to two SAR images (the image0 and image25). The image0 shows a strong well defined internal waves signature, with orientation along the diagonal of the scene. The image25 is the opposite, the signature of the 2 major internal waves present are weaker, and vertical with respect to the scene orientation. These two cases were chosen, because they represent the two extreme cases of the internal waves signature present in SAR image and provide a good test for the method proposed.

PCA technique: The discrimination between classes was done using the idea that it is necessary to have as much difference as possible between the presence of internal waves (event) and the non-presence of internal waves (non-event). The results presented for each individual study show, the total accuracy, the percentage of the misclassification

of the non-event and the misclassification event. The accuracy offered by this classification is reasonable, but dependent on a particular threshold. The threshold needed to optimize the classification is very variable, which makes generalization of the technique difficult. In the presented results, the threshold was set at zero to offer comparative results, but in many cases this was not the best solution to perform the most accurate classification.

KNN technique: Two KNN techniques were used, a traditional KNN and a weighted KNN, using a range of values of k (k = 3, 5, 7). The results presented for each individual cases show, the total accuracy, the percentage of the misclassification of the non-event and the misclassification event. The accuracy offered by this classification is slightly better in terms of accuracy, but definitely more reliable, as this method does not need any threshold, so it offers the chance to perform a generalization of the result. The best configuration found was with $k = 3$ and with the input vector having a length of $2 - 4$.

MLP technique: The MLP use was made up with 6 input nodes, one hidden layer containing 12 node, and one output node. This classifier offer the best classification of the three, with a best configuration for the wavelet representation mXY and a value of $d = 3$.

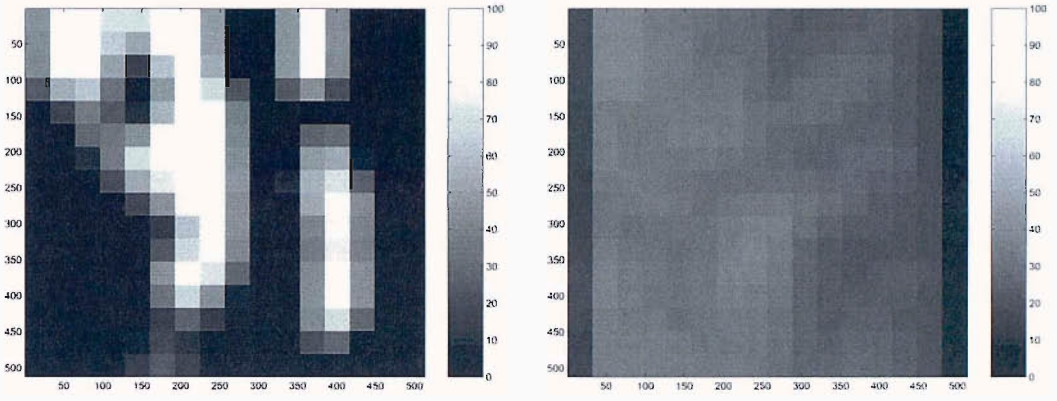

(a) Classification for X-decomposition

(b) Classification for Y-decomposition

Figure 5.25: MLP output for k=3 using the X and Y wavelet representation of the image25

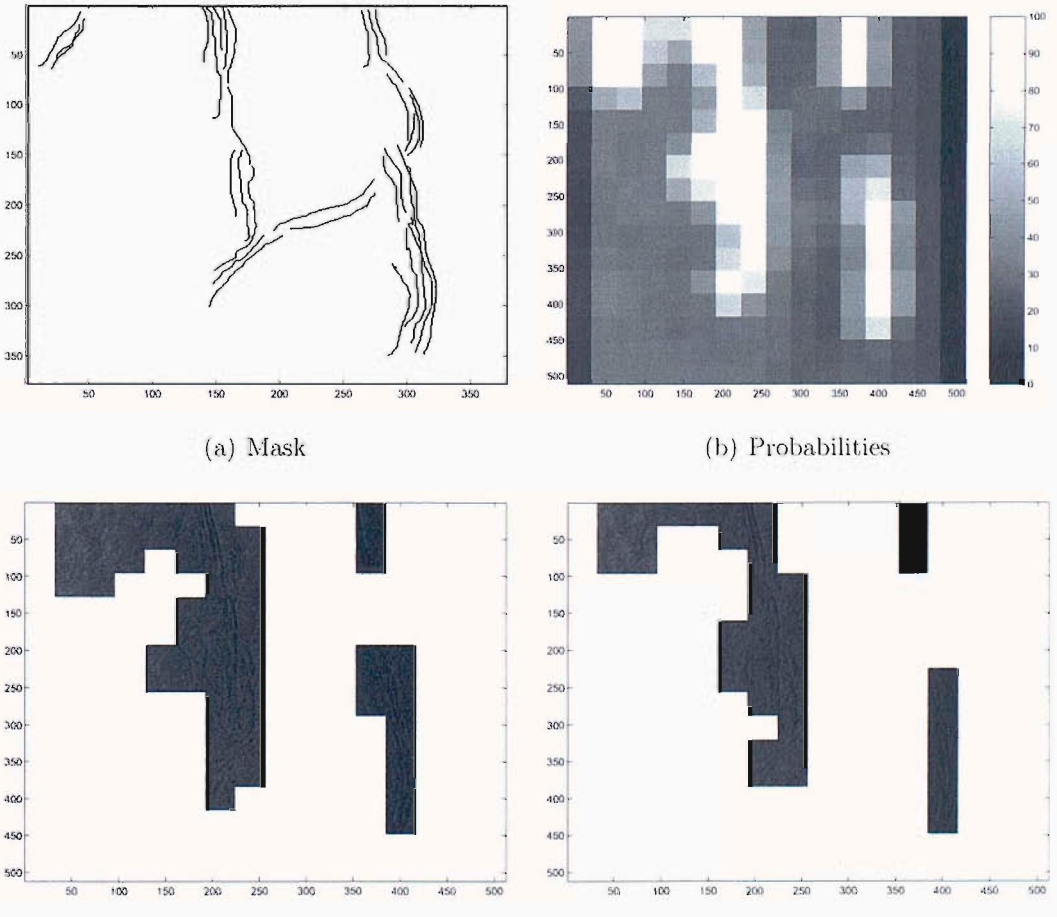

(a) Mask

(b) Probabilities

(c) Classification at 50% confidence

(d) Classification at 70% confidence

Figure 5.26: MLP output for k=3 using the XY wavelet representation of the image25

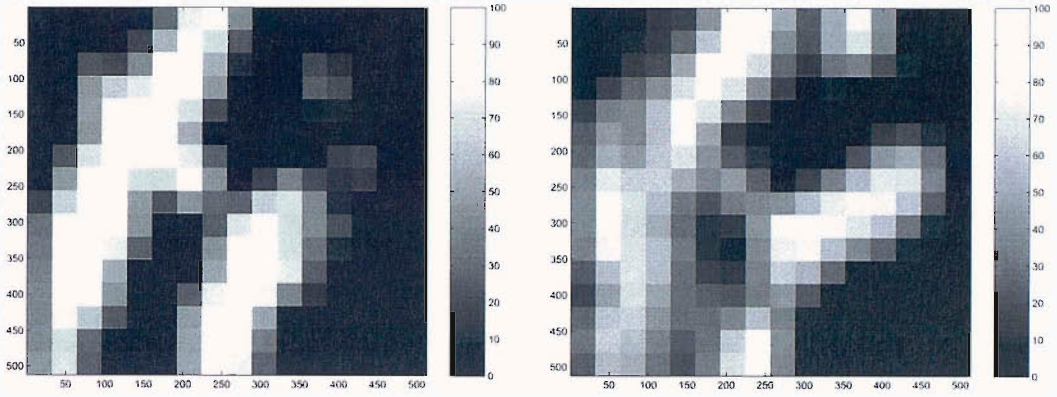

(a) Classification for X-decomposition

(b) Classification for Y-decomposition

Figure 5.27: MLP output for k=3 using the X and Y wavelet representation of the image0

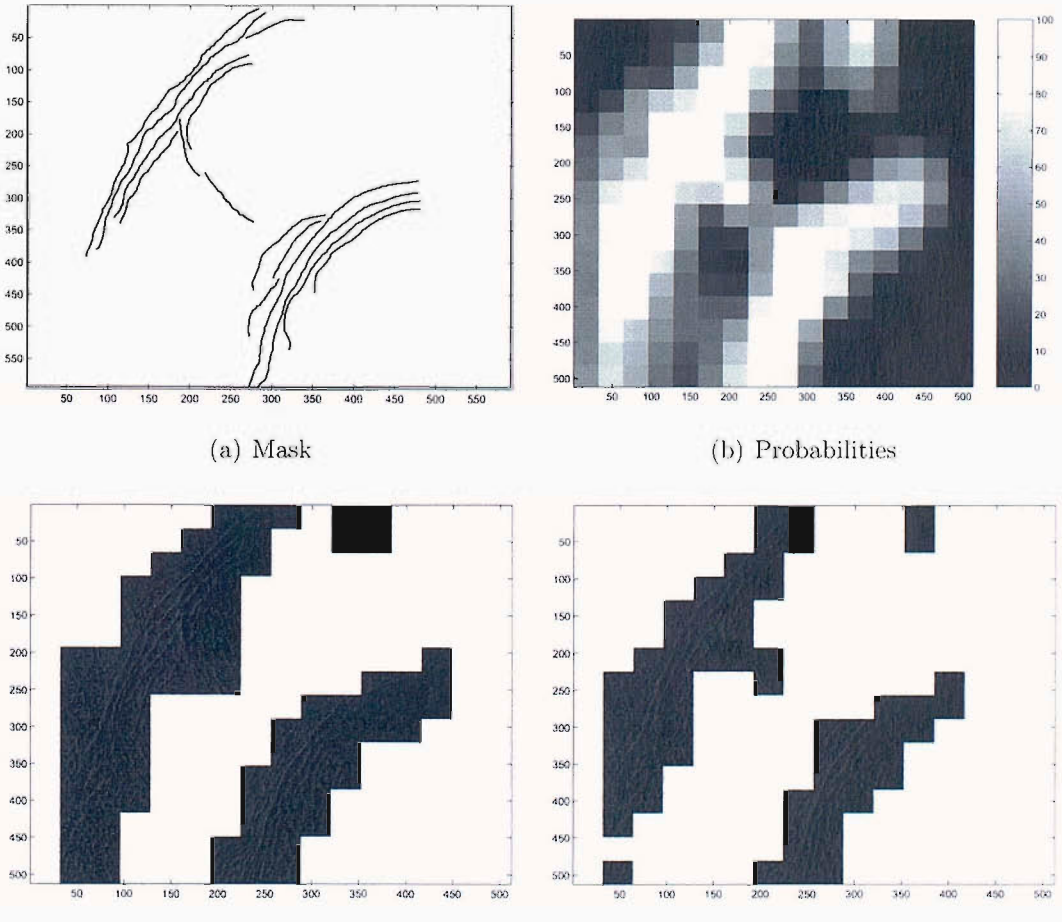

(a) Mask

(b) Probabilities

(c) Classification at 50% confidence

(d) Classification at 70% confidence

Figure 5.28: MLP output for k=3 using the XY wavelet representation of the image25

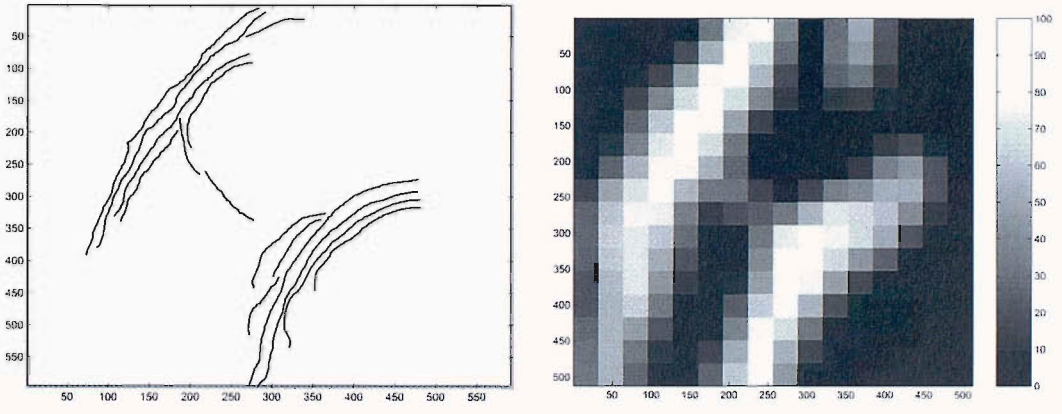

(a) Mask

(b) Probabilities

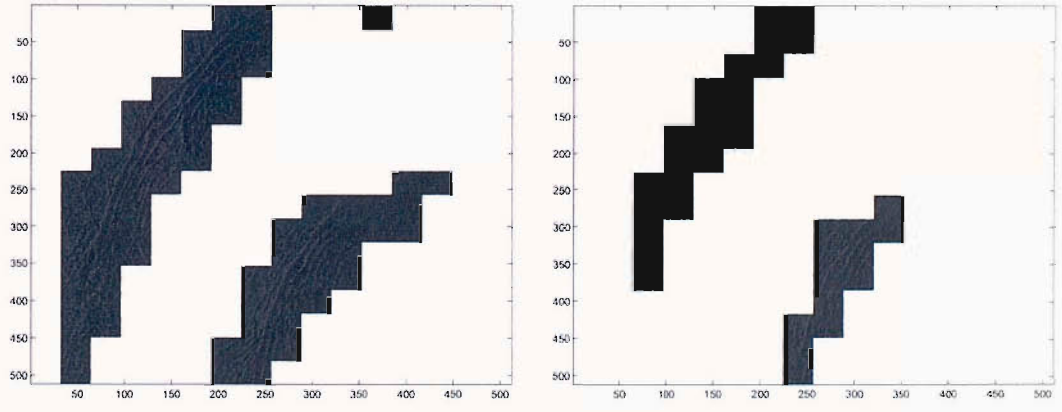

(c) Classification at 50% confidence

(d) Classification at 70% confidence

Figure 5.29: MLP Classification of the image 0 for different cutoff values, for k=3 using mXY wavelet representation

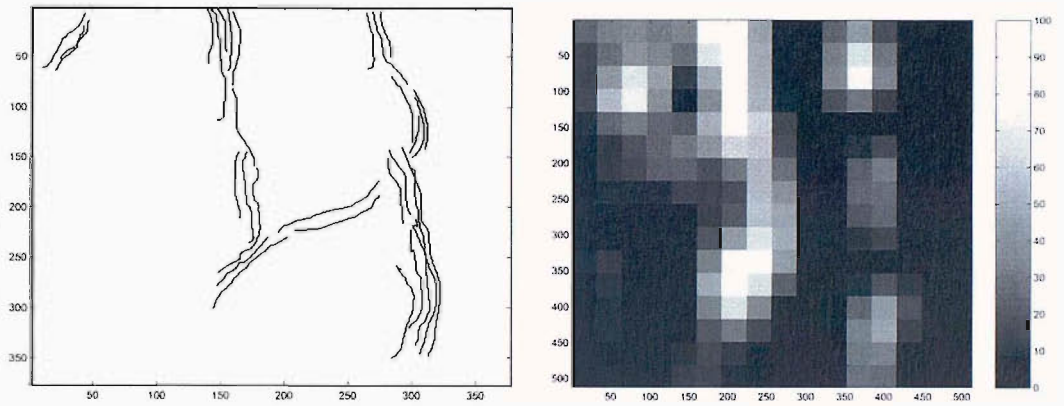

(a) Mask

(b) Probabilities

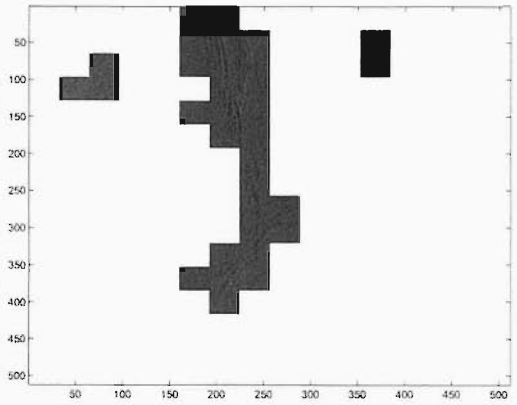

(c) Classification at 50% confidence

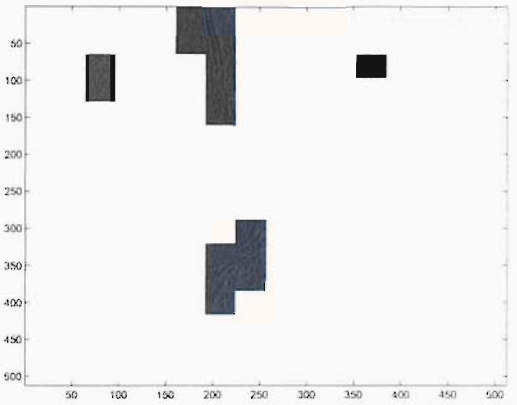

(d) Classification at 70% confidence

Figure 5.30: MLP Classification of the image 25 for different cutoff values, for k=3 using mXY wavelet representation

Chapter 6

Edge extraction

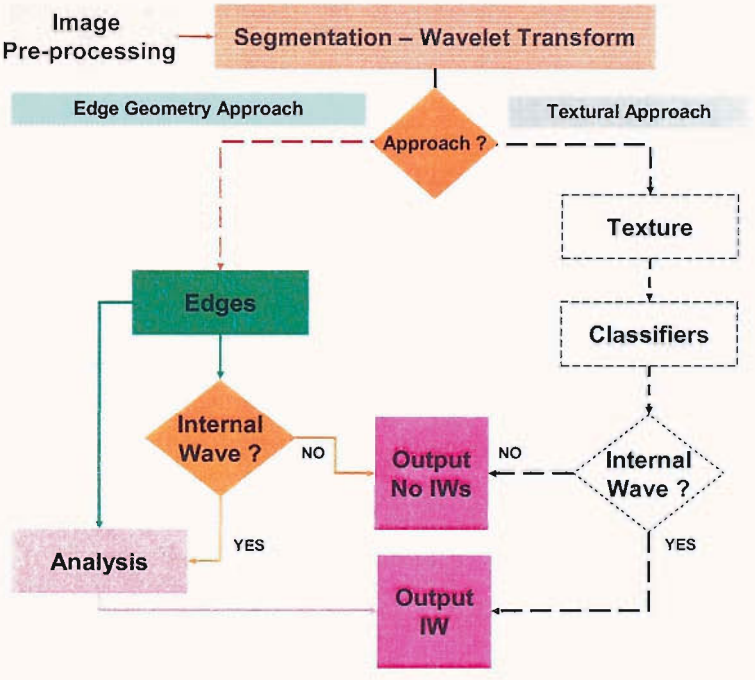

Figure 6.1: Diagram illustrating the layout of the processing

6.1 Introduction

The aims of this chapter are to investigate whether it will be possible to extract the internal wave signatures within the SAR images by considering the edges of these features and their geometry. Feature extraction generally seeks invariance properties so that the extraction process does not vary according to chosen conditions. Extraction implies that a description of a shape, such as its position and size is available. There are many techniques for features extraction, such as the hough transform [31], generalised hough transform [21] and active contour techniques [15] [69]. The edges which characterize the

internal waves take in general the form of train lines, or/and arc with different radius. Therefore it is difficult to assign a general template for the shape of the edges. Their direction, size and their number are very variants. The variant characteristics of the signature are a major problem to overcome. The solution is found by partitioning the problem with a very simple approach. The template is defined as follows: find three edges with a distance of d with $d_{min} > d > d_{max}$ between each other and presenting pseudo-parallelism. Any predispositions of shape, orientation or size are used in the template. However before applying the template to the edges list, pre-processing is needed to make sure that the edge of a single potential internal wave is represented by one and only one edge. Therefore a test of edge continuity and cooperation between edges has to be made.

6.2 Edge tracing, Continuity and cooperation between edges

6.2.1 Edge tracing

Edge analysis is understood to be the study of the geometry of the edge obtained from the internal wave signatures. To allow this study to take place, the edge of the internal wave has to be represented by one continuous line. This is where the edge tracing, approximation to a continuous curve becomes useful.

Edge Tracing Method and Curvature Edge tracing is one of the most fundamental subjects of image analysis. An edge can be traced by simply following the line of high pixel values (above a given threshold). For this, any edge line of the object is accepted as the starting point and the edge is traced.
In order to follow the edge of an object in lines there are methods like Hough and Rotation Transformations [35], but because the internal wave edges do not have a classical geometric shape such as a line or circle, these techniques have proven to be difficult to control and tune. In this work, a simpler algorithm is presented using a hysteresis threshold technique (figure 6.2) instead [62].

1. ***Step 1:*** A first pixel point of a given edge is found by a primary scanning of the image (modulus wavelet representation) and identifying a point above a given

upper threshold (figure 6.2 and 6.3).

2. ***Step 2:*** The subsequent points are traced if the points are above a given lower threshold

3. ***Step 3:*** The coordinates of the edge point found in step 2 are used to determine the direction for the next search, by taking the last 10 last points found and determining θ from a simple linear regression.

4. ***Step 4:*** Repeat step 2 and 3 until no edge point is found.

The mathematical expressions to determine the advancing direction are as follows:

$$x = x + f(cos(\theta)) \tag{6.2.1}$$

$$y = y + f(sin(\theta))$$

$$\text{where } \theta = -\pi, -\frac{\pi}{2}, \frac{\pi}{2}, \text{ or } \pi$$

The value of x and y are rounded to the closed integer. Small segments are generally

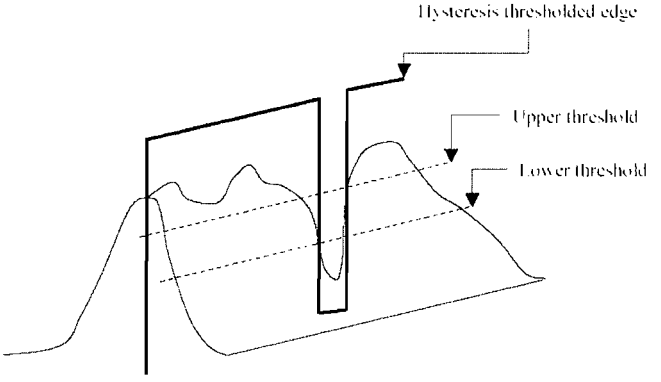

Figure 6.2: Hysteresis thresholding

defined by cubic polynomial functions. The fitting can be achieved by considering a parametric form. In a parametric representation, the contour $v(t)$ (i.e. $v(t) = (x(t), y(t))$) can be approximated by two polynomials given by:

$$x(t) = a_x + b_x t + c_x t^2 \tag{6.2.2}$$

$$y(t) = a_y + b_y t + c_y t^2 \tag{6.2.3}$$

A definition of the curvature (k) at $v(0)$ can be obtained by considering the derivation of the equation 6.2.2 and 6.2.3 using the form of the equation 6.2.4(see table 6.1). Accordingly, the value of the curvature for the pixel $v(0)$ is given by equation 6.2.5 [46].

$$k(t) = \frac{\dot{x}(t)\ddot{y} - \dot{y}(t)\ddot{x}}{[\dot{x}^2(t) + \dot{y}^2(t)]^{\frac{3}{2}}} \tag{6.2.4}$$

$$k(0) = 2\frac{c_y b_x - c_x b_y}{[b_x^2 + b_y^2]^{\frac{3}{2}}} \tag{6.2.5}$$

The knowledge of the curvature can by used to disregard edges that have a curvature greater than a given threshold, because they do not represent an internal waves signature and are either an artifact or another unwanted feature.

If $v(t)$ is a curve, then it can be express in a parametric form such as:

$$v(t) = x(t)\vec{i} + y(t)\vec{j}$$

where $\vec{i}$ and $\vec{j}$ are the vector unit. At any point within this curve $v(t)$ the tangent can be describe by its modulus $|\dot{v}(t)| = \sqrt{\dot{x}^2(t) + \dot{y}^2(t)}$ in the direction $\varphi(t) = \tan^{-1}(\dot{y}(t)/\dot{x}(t))$. The curvature at this point describe the changes in the direction $\varphi(t)$ with respect to changes in arc length:

$$k(t) = \frac{d\varphi(t)}{ds} \tag{6.2.6}$$

where s is arc length, along the curve itself. One can rewrite equation 6.2.6 as:

$$k(t) = \frac{d\varphi(t)}{dt}\frac{dt}{ds} \tag{6.2.7}$$

The term $\frac{dt}{ds}$ describe the change in the arc length with respect to t. If one considers the curve as the motion of a point, then this differential defines instantaneous change in distance with respect to time (the speed):

$$\frac{ds}{dt} = |\dot{v}(t)| = \sqrt{\dot{x}^2(t) + \dot{y}^2(t)} \tag{6.2.8}$$

and

$$\frac{dt}{ds} = \frac{1}{\sqrt{\dot{x}^2(t) + \dot{y}^2(t)}} \tag{6.2.9}$$

By considering that $\varphi(t) = \tan^{-1}(\dot{y}(t)/\dot{x}(t))$, then the curvature at a point $v(t)$ in equation 6.2.9 is given by the expression 6.2.5

Table 6.1: Description of curvature [46]

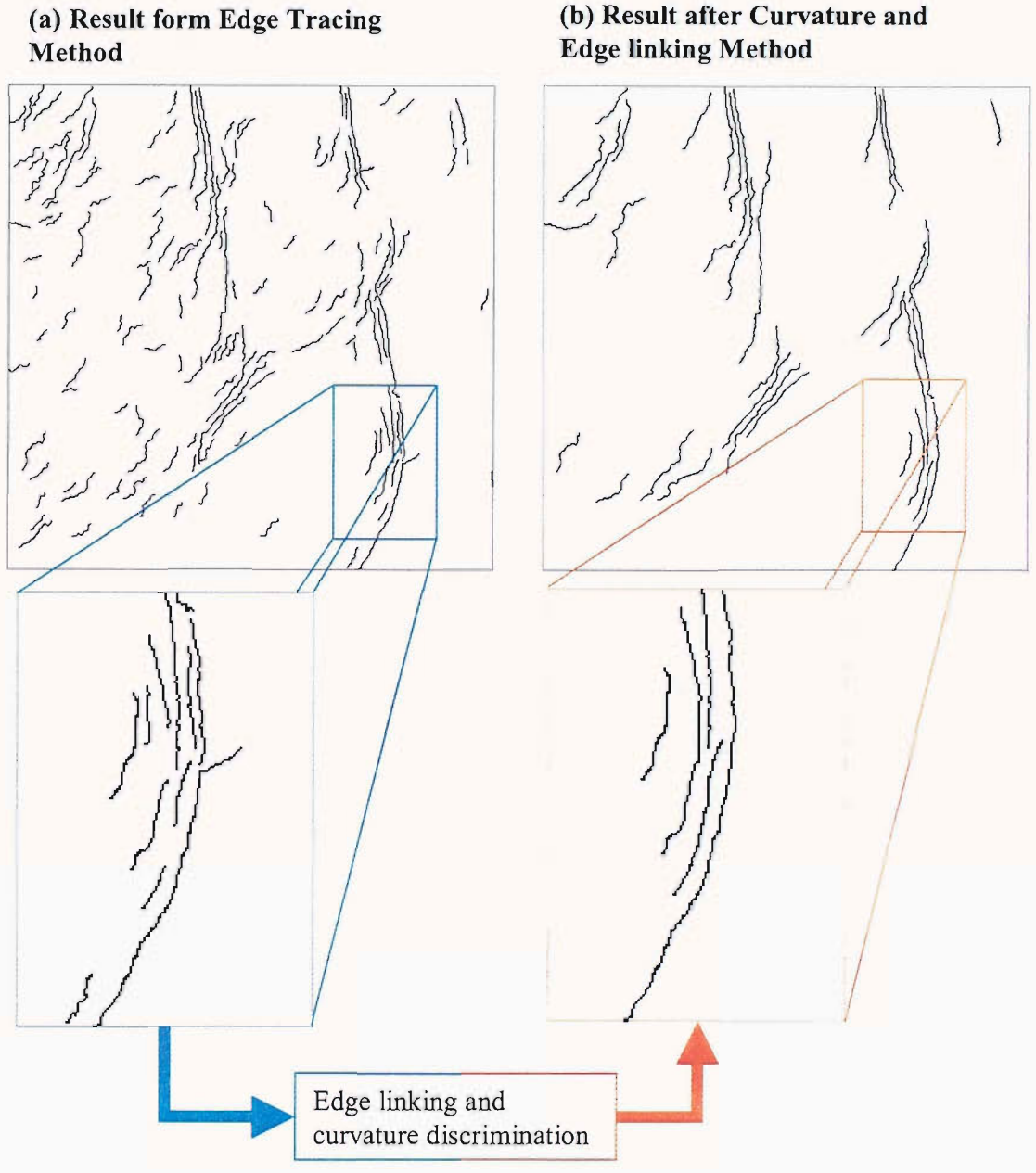

Figure 6.3: Examples from the Edge training and curvature discrimination. (a)Edge tracing method apply the modulus from the wavelet transform. (b) The curvature discrimination as well as edge linking technique. One can see that from (a) to (b) some edge have been disregarded using the curvature criterium.

6.2.2 Continuity and cooperation between edges

The purpose of continuity and cooperation between edges is to identify significant structural relationships. The operation is done by successive refinement [43] following a bottom-up strategy. Figure 6.4 show the application of this process where the length of the accepted gaps is proportional to the length of the two segments. Furthermore the grouped segments from one level are considered as individual for the next level. This strategy permits local information to be integrated into a global context. In order to recover curvilinear segments, it is useful to identify which segments are potentially neighbours. It then necessary that potential neighbours segment must satisfy in general, two geometric constraints: proximity and continuity. The continuity and proximity criteria are presented in figure 6.5. More precisely, the candidate must verify the following relation where $\varepsilon = 0.1$ and $a = 1$ and $b = 0.1$ [43] are two constants which account for the proximity. The measure of ε (called measure of bending [43]) allowed is a function of the parameter a, which controls the departure from the collinearity of the joined curves, of b which controls the sensitivity to the length of the gaps being filled and t which is the length of the gap.

$$\varepsilon \leq (\alpha^2 + \beta^2(a + bt)) \tag{6.2.10}$$

where α and β are expressed in radius.

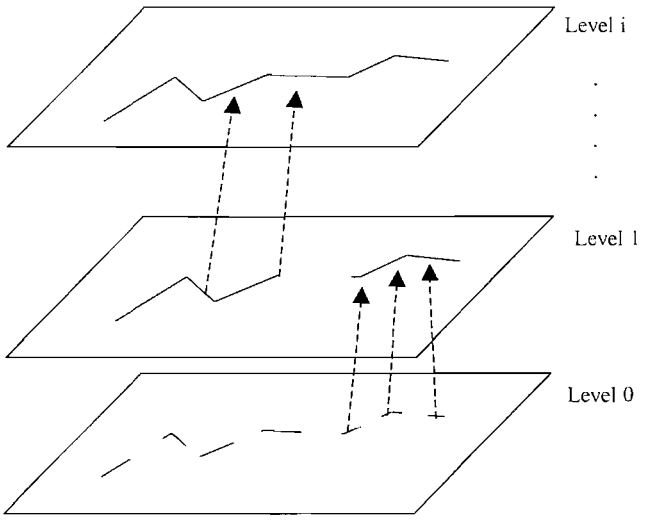

Figure 6.4: Successive refinements

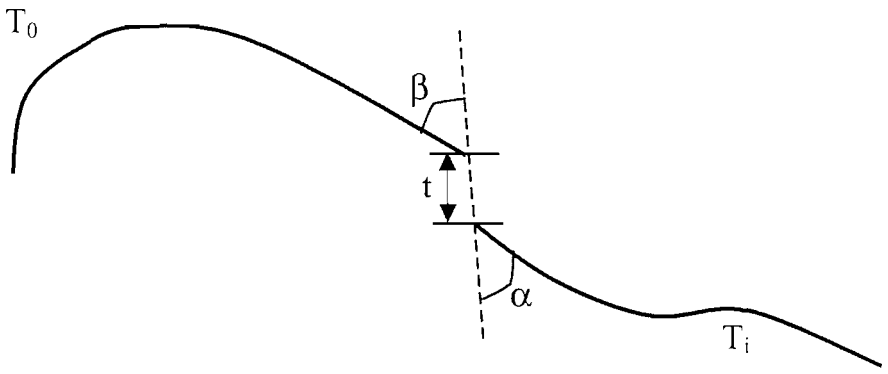

Figure 6.5: Continuity criteria

6.2.3 Implementation

The edge detection was made using the wavelet multi-resolution technique, and linked into chain points. Figure 6.6 show a result of this process. Some edge are dropped out due to the poor contrast or/and broken due to poor linking. The grouping process start by identifying for each free segment (chain points) a set of free neighbouring segments. These selected segment satisfy constraints on measures of proximity and continuity. If more than one segment is found to match the criteria, the one selected is the one that minimizes the expression 6.2.10. The gap between two segments is filled using a linear regression. This grouping process is repeated iteratively until no more grouping are found.

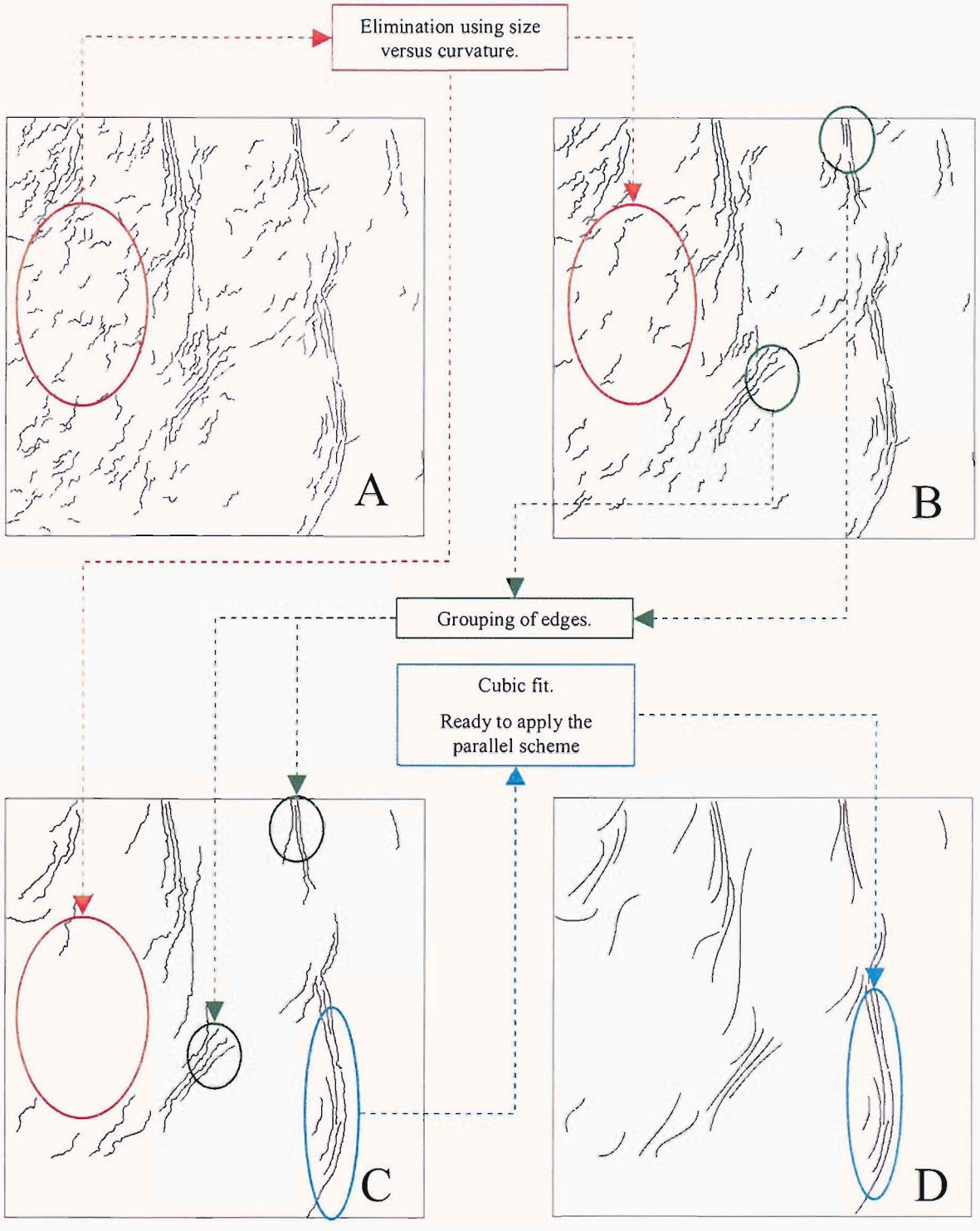

Figure 6.6: Examples from the Continuity and cooperation between edges. (A) show the edges detection scheme using the wavelet multi-resolution technique using an automatic threshold. (B)and(C) are the result from the continuity and cooperative edge technique.(D) show the cubic fit of the selected edges

6.3 Parallelism of the edges

The concept of parallelism for straight lines is clear but there is a lack of an established model for describing parallelism among curves. The following section will describe a model for describing parallelism among curves and extract common properties among them to serve as a measuring rod for parallelism detection [32].

This model uses the properties of the tangent of a given point part of a curve, so we will start by introducing a new tangent representation called Direction-dependent tangent (DDT), which incorporates concavity information into the tangent representation and prohibits false matching. Based on a theorem and the tangent representation an algorithm for parallelism detection will be presented using driving forces.

6.3.1 Direction-Dependent Tangent (DDT) Representation:

The tangent at a point on a given curve is defined as the slope at this point. The curve (C) can be represented in a parametric way, such that the position of a point $(C(k))$ can by expressed by $C(k) = (x(k), y(k))$. Therefore the tangent vector at this point can be defined by $\overrightarrow{\varphi}(k) = (\dot{x}(k), \dot{y}(k))$. In this definition $\dot{x}(k)$ represent the differentiation of x with respect of t at the point k. $\overrightarrow{\varphi}$ is a vector, but only the direction component is of any interest. Therefore $\overrightarrow{\varphi}$ represent the orientation of the vector tangent with a range of $[-\pi, \pi]$.

When a curve is represented in a parametric manner, the sense in which the sequence of the points are defined, has an influence on the sense of the tangent. If the sequence of the points is defined form the right to the left, the tangent orientation will be different from a sequence of the points is defined form the left to the right. In other words $\overrightarrow{\varphi}$ is sensitive to the coding direction of the curve C. The impact is that two tangent from two different curve can be only be compared correctly if and only if the coding direction of the two curves is done using the same direction. In order to resolve this problem IP and Wong [32] create an extension to tangent definition called: Direction-Dependent Tangent (DDT).

Figure 6.7 show the same curve with two different coding directions. By working in either curve the tangents point toward the direction of movement and are called forward tangents. $\varphi_q(s)$ represents the forward tangent at $C_q(s)$ and is defined by $\varphi_q(s) = atan2(\dot{x}_q(s), \dot{y}_q(s))$ with range $[-\pi, \pi]$ ($atan2$ is the standard C function that return arc tangent according to the signs of x and y argument). However for implementation,

Figure 6.7: (A) Clockwise direction while (B) show a anticlockwise coding direction.

the tangents are set to a positive value ([0 2π]) and are defined by

$$\varphi_q(s) = (atan2(\dot{x}_q(s), \dot{y}_q(s)))mod\ 2\pi$$

In addition to the tangent orientation, the sense of rotation of the tangent is important. In other words one can record if the tangent appears to the left or the right-hand side with respect to the sense of coding of the curve. They are called left tangent and right tangent respectively. Figure 6.7 (A) show left tangents and figure 6.7 (B) show right tangents.

To determine whether a tangent is left- or right-tangent is an easy task. Anti-clockwise turning tangent orientations implies right-tangents. These tangent vectors are positively oriented. Denote the relation $\Gamma(\varphi_q(a), \varphi_q(b))$ between two vectors a and b with orientation $\varphi_q(a)$ and $\varphi_q(b)$ that are positively oriented,

$$\Gamma(\varphi_q(a), \varphi_q(b)) \Leftrightarrow \begin{vmatrix} cos(\varphi_q(a)) & cos(\varphi_q(b)) \\ sin(\varphi_q(a)) & sin(\varphi_q(b)) \end{vmatrix} \geq 0 \tag{6.3.1}$$

if $\Gamma(\varphi_q(s), \varphi_q(s+\varepsilon)) \geq 0$ is satisfied, where ε is small positive number, then the forward tangent at point s is a right-tangent. Otherwise, it is a left-tangent. To incorporate this information into the tangent representation, DDT is defined as:

$$\psi_q(s) = \begin{cases} \varphi_q(s) + 2\pi & \text{if } \Gamma(\varphi_q(s), \varphi_q(s+\varepsilon)) \geq 0 \\ \varphi_q(s) & \text{otherwise} \end{cases} \tag{6.3.2}$$

Two DDTs ψ_1 and ψ_2 are equivalent if either one is true: Same orientation and both left-tangent or both right-tangent ($\psi_1 = \psi_2$). Or/and opposite orientation with one left- and one right-tangent ($|\psi_1 - \psi_2| = \pi$ or 3π). Therefore the operator $Left(.)$ (i.e. ensure that the angle is between 0 and 2π) is defined for DDTs as:

$$Left(\psi) = \begin{cases} \psi & \text{if } \psi < 2\pi \\ (\psi - \pi)mod\ 2\pi & \text{if } \psi \geq 2\pi \end{cases} \tag{6.3.3}$$

The equivalency between two DDTs, can be described by $\psi_2 \Leftrightarrow \psi_1 \triangleq \psi_2$

$$Left(\psi_1) = Left(\psi_2) \Leftrightarrow \psi_1 \triangleq \psi_2 \tag{6.3.4}$$

6.3.2 Types of Parallelism and perceptual parallelism problems:

Parallelism of a curve is a more general term than for the straight line case. In fact one can identify three types of parallelism (figure 6.8). As their properties are used to construct the model, it is important to give a definition: a sleeper refers to a line joining two segments (i.e. rail track) on each of the curves that are being compared. (The procedure to select two segments to be joined is detailed is section 6.3.3.)

1. Let C_x and C_y denote two simple segments, if all sleepers within the segment are of the same slope, this is sufficient condition to say that the two segment are in translation parallelism (case 1).

2. Let C_x and C_y denote two simple segments, if all sleepers established are perpendicular to their DDTs, this is sufficient conditions to say that the two segment are in railroad parallelism (case 2).

3. Let C_x and C_y denote two simple segments, if all sleepers are concurrent on elongation, this is the sufficient condition to say this is of central similarity transform parallelism (case 3).

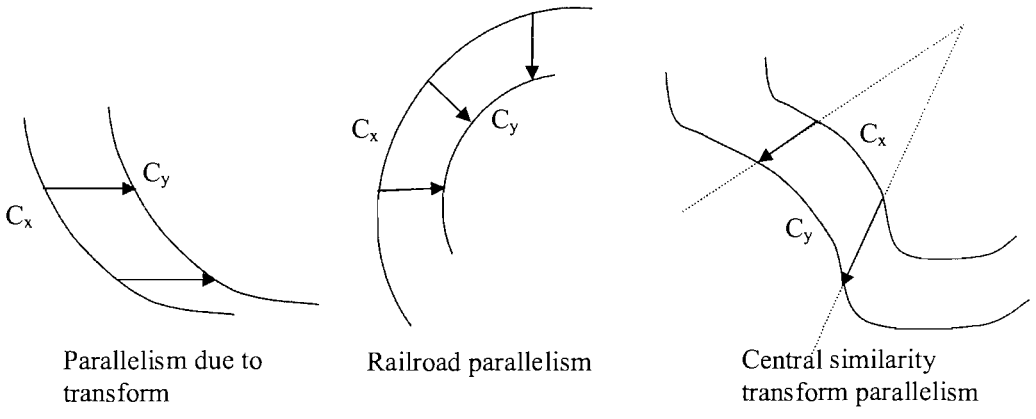

Figure 6.8: Parallelism definitions

Using these strict definitions of parallel curves a set of criteria can be built. However these definitions can only be used as a guideline. It is clear that one does not have enough information to distinguish between railroad parallelism and central similarity

transformation without producing further information. This suggests that the algorithm should be able to detect perceptual parallel curves. Therefore Ip and Wong [32] formulated an inspection procedure for perceptual characteristic of parallel curves. Four perceptual characteristics have been identified, they are: Sleeper Criterion, Tangent Alignment Criterion, Similarity Criterion and Elasticity Criterion. These characteristics are used in terms of a minimization problem: if the curves obey enough of these criteria them they are perceptually parallel.

The formulation of these criteria is expressed using driving forces. It was not very practical to apply these forces to every point of each curve, because they can for instance, be composed of infinite number of points. Instead one wants to create a list of important salient points that exists on both sleepers. Another consideration is that every tangent of both curves needs to have the same orientation; therefore the curves are divided into simple segments. The point of separation of one curve to two simple segments is the point where the curvature is null. If a curve with a form like an S is taken and the curvature separation test applied , two simple segments are obtained, one having its tangent in the opposite sense to the other.

Driving forces Given two simple segments, one from each curve, one is chosen as the active segment and is approximated it by its salient points. These salient points are then coupled to the other segment by linear interpolation. This initial match does not have to meet all the criteria it is just a starting point. The goal was to show that the two simple segments are perceptually parallel or not, it is necessary to find the match for every salient points of the active segment onto the passive segment. The task of best matching will be performed using these forces. For every pair (a salient point from the active segment and an associate point from the passive segment), a measurement of necessary displacement to obtain the perfect match is calculated using the four forces. These can reinforce each other if they are in the same direction or balance each other if they are in opposite direction. During each iteration, the resulting force is computed and adjustment of the point associate to the salient points is made accordingly. The process stops when no more adjustment can be made and a convergence is reached and the test for parallelism can be applied to the two segments using a calculation of the error with respect to a perfect case. If the error is below a given threshold: the two simple segments are considered parallel. The four forces used for the convergence are

as follows (figure 6.9 gives a schematic representation of these forces) [32]:

- **Force one: Deflection force:**

  A defection force is defined as a force that acts to minimize the deviation in coupling orientation. For a pair of parallel simple segment, salient point on C_i should be coupled to points on C_j such that the sleepers joining them are either parallel to those at the endpoint or concurrent (see figure 6.9-a). In other words, is the vector (P_5, P_6) parallel to the vector (P_1, P_2)? This force and its direction can be express as followed (see table 6.2 for reference): (where $q_1(S_p)$ represent the strength (modulus) of the force and $g_1(S_p)$ its orientation.)

$$q_1(S_p) = \begin{cases} \langle (P_5 - P_0) \rangle \times \langle (P_6 - P_5) \rangle & \text{if } \langle (P_2 - P_1) \rangle \cdot \langle (P_4 - P_3) \rangle \neq 1 \\ \langle (P_5 - P_1) \rangle \times \langle (P_6 - P_5) \rangle & \text{otherwise} \end{cases} \tag{6.3.5}$$

$$-g_1(S_p) = \begin{cases} \psi_j(f(S_p)) & \text{if } [q_1(S_p) > 0] \cdot eq \cdot IsLeft(\psi_j(f(S_p))) \\ \psi_j(f(S_p)) + \pi & \text{otherwise} \end{cases} \tag{6.3.6}$$

  Where "eq" is the equality operator and $IsLeft$ identify if the given DDT is a left-tangent. Note that the expression on both side of the equality operator are boolean expression (0 or 1).

$$P_a = (x_a, y_a)$$

$$\langle (P_a - P_b) \rangle \times \langle (P_c - P_d) \rangle = (x_a - x_b)(y_c - y_d) - (y_a - y_b)(x_c - x_d)$$

$$\langle (P_a - P_b) \rangle \cdot \langle (P_c - P_d) \rangle = (x_a - x_b)(x_c - x_d) + (y_a - y_b)(y_c - y_d)$$

$$\langle \psi_i(S_p) \rangle = (cos(\psi_i(S_p)), sin(\psi_i(S_p)) \text{ with } \psi_i(S_p) \in [0, 2\pi]$$

$$\langle \psi_i(S_p) \rangle \times \langle \psi_j(f(S_p)) \rangle = cos(\psi_i(S_p)) \times sin(\psi_j(f(S_p))) - sin(\psi_i(S_p)) \times cos(\psi_j(f(S_p)))$$

Table 6.2: Expression definitions

- **Tangent alignment force:** For parallelism to exist, the tangents of conjugate pairs must agree. However under perspective parallelism it is not possible to have a perfect agreement, but one can look for a deflection small enough that the two curve look parallel when observed by human eyes (see figure 6.9-b). i.e. is the

tangent $\psi_j(f(S_p))$ approximately parallel to the tangent $\psi_i(S_p)$. The magnitude of this force and its direction can be express as followed:

$$q_2(S_p) = \langle Left(\psi_i(S_p))\rangle \times \langle Left(\psi_j(f(S_p)))\rangle \tag{6.3.7}$$

$$-g_2(S_p) = \begin{cases} \psi_j(f(S_p)) & \text{if } [q_2(S_p) > 0] \cdot eq \cdot IsLeft(\psi_j(f(S_p))) \\ \psi_j(f(S_p)) + \pi & \text{otherwise} \end{cases} \tag{6.3.8}$$

Where "eq" is the equality operator and $IsLeft$ identify if the given DDT is a left-tangent. Note that the expression on both side of the equality operator are boolean expression (0 or 1).

- **Approximation error force:** As described above, the curve C_i is approximated using a set of salient points $C_i(S_p)$. This implies that the corresponding point $C_j(S_p)$ is an approximation of the curve C_j. If the two curves are parallel (see figure 6.9-c) the magnitude of this force and its direction can be expressed as followed:

$$q_3(S_p) = d_j(f(S_p)) - d_j(f(S_{p+1})) \tag{6.3.9}$$

Where $d_j(f(S_p))$ denote the perpendicular distance measured to the farthest distance on C_j from the chord curve defined by $C_j(S_p)$ and $C_j(S_{p+1})$ (figure 6.10 (c))

$$-g_3(S_p) = \begin{cases} \psi_j(f(S_p)) & \text{if}[q_3(S_p) > 0] \cdot eq \cdot [IsLeft(\psi_j(S_p)) \cdot eq \cdot IsLeft(\psi_j(f(S_p)))] \\ \psi_j(f(S_p)) + \pi & \text{otherwise} \end{cases} \tag{6.3.10}$$

Where "eq" is the equality operator and $IsLeft$ identify if the given DDT is a left-tangent. Note that the expression on both side of the equality operator are boolean expression (0 or 1).

- **Elasticity force:** For the pair of simple segments to being coupled, distance between successive coupled points $C_j(f(S_p))$ are lengthened or shortened more or less uniformly during the coupling process(see figure 6.9-d). This force and its direction can be express as followed:

$$q_4(S_p) = \frac{arcLength_j(f(S_p), f(S_{p+1}))}{arcLength_j(S_p, S_{p+1})} - \frac{arcLength_j(f(S_{p-1}), f(S_p))}{arcLength_j(S_{p-1}, S_p)} \tag{6.3.11}$$

$$-g_4(S_p) = \begin{cases} \psi_j(f(S_p)) & \text{if } [q_4(S_p) > 0] \cdot eq \cdot [IsLeft(\psi_j(S_p)) \cdot eq \cdot IsLeft(\psi_j(f(S_p)))] \\ \psi_j(f(S_p)) + \pi & \text{otherwise} \end{cases} \tag{6.3.12}$$

Where "eq" is the equality operator and $IsLeft$ identify if the given DDT is a left-tangent. Note that the expression on both side of the equality operator are boolean expression (0 or 1).

These forces are calculated for each salient points $C_i(S_p)$ and its the conjugate $C_j(f(S_p))$ at each iteration. Then a resultant of the four forces is simply calculated and the conjugate point $C_j(f(S_p))$ are moved following the direction of the resultant forces until a steady state is reach. The minimization procedure uses a greedy algorithm [67], [46], which will find the best solution by an iterative process(figure 6.10). There is no need to use a best tool for the minimization as the greedy algorithm rarely needy more then 10 iterations to find the minima.

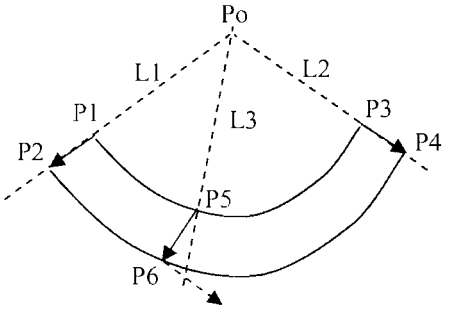

(a). Force one: Deflection force

Deviation between the coupled result and the expected orientation generates a deflection force at P6 which is shown as a dotted arrow.

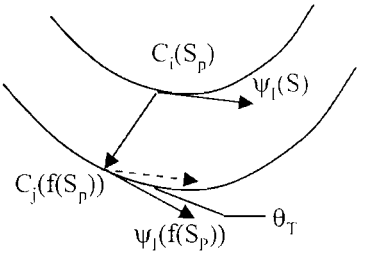

(b). Force two: Tangent alignment force

The angle θ_T defines the difference between the DDT's of the coupled points. This will generate the tangent alignment force at $C_j(f(S_p))$.

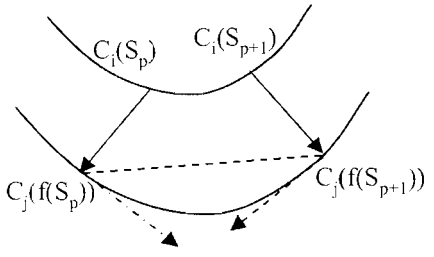

(c). Force three: Approximation error force

Large approximation error generate will approximation error force to pull the coupled points. These are shown as dotted arrows.

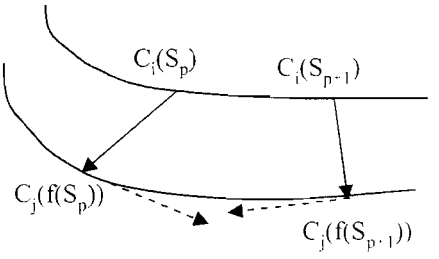

(d). Force four: Elasticity force

Stretching (compression) of active segment when coupled to passive segment creates elasticity forces to bring the coupled results closer to (further apart from) each other.

Figure 6.9: Forces-Driven correspondence matching

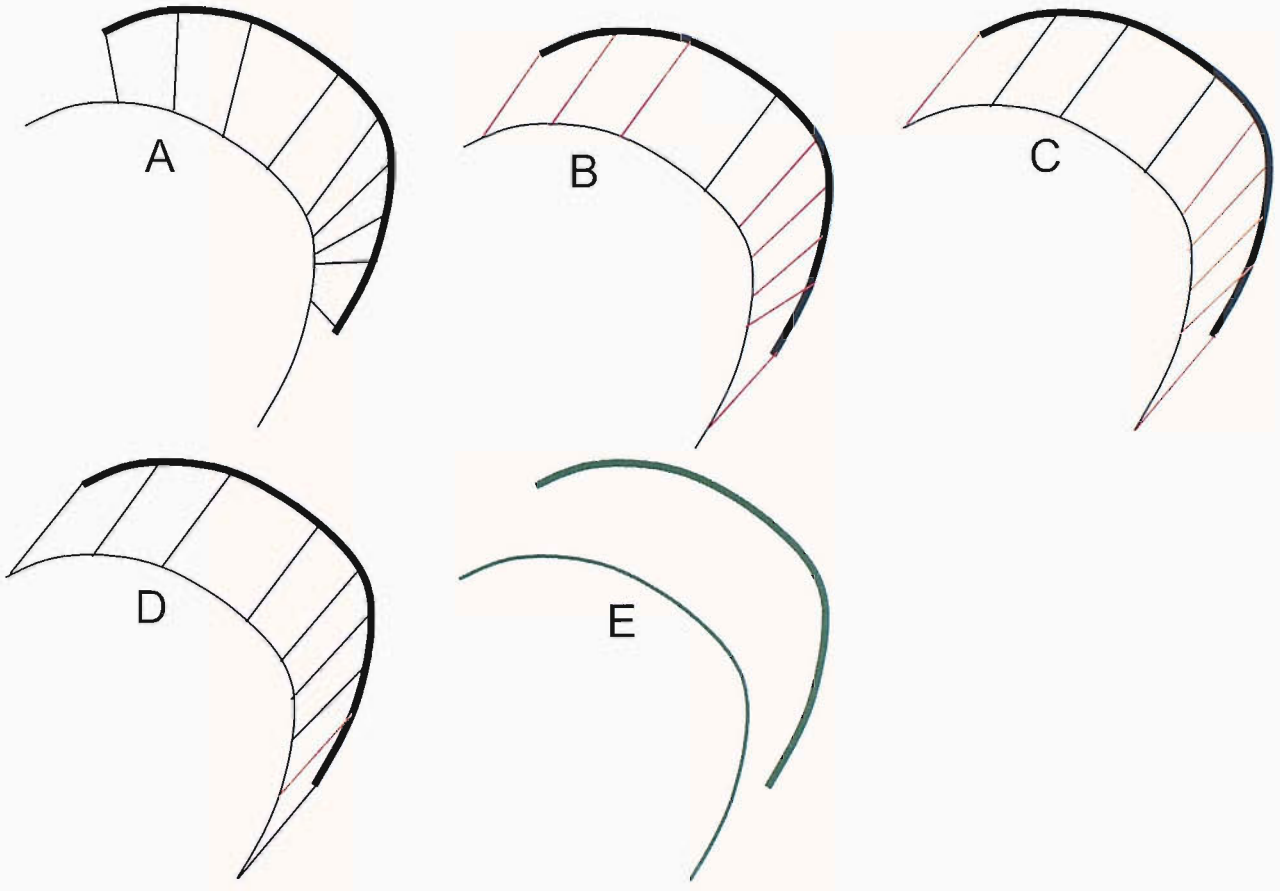

Figure 6.10: Example of search for perspective parallelism. (a)show the initial mapping of the salient point from the active curve (bold) and the passive curve. (b) show the mapping after 3 iterations; red sleepers indicate change during the iterations. (c)show the mapping after 6 iterations (d)show the mapping after 9 iterations (e)detection result with parallel section mark as green.

6.3.3 The algorithm

This section summarizes the algorithm.

1. *Decomposition into simple segments:*Measure the DDTs along the two curves and break the curves into simple segments

2. *Pre-scanning for possible coupling between simple segments:* Two simple segments (one from each curve) may be coupled if and only if their DDTs are equivalent at end points. In fact this process filters out a lot of combinations which otherwise would need to be tested. However, a one to one mapping is not guaranteed. Sometimes one simple segment can be coupled to more than one simple segment to

the other curve. Hence, in this step, candidate simple segment pairs for parallelism verification can be identified.

3. *Detail coupling and parallelism verification:* For each possible combination of simple segments coupled at step 2, identify the segment pairs that are parallel; two segments (one from each curve) are parallel if the coupling result along them satisfies one of the schemes described in the parallelism test.

4. *Reporting:* Keep the combination that gives the longest continuous parallel section. Report parallelism if the parallel section is longer than a certain threshold (in this study, 55% of the curve length).

Prescanning step

In order to achieve a successful prescanning, one must relax the DDT equivalent definition given by the equation 6.3.4 by allowing some deviation.

$$\langle Left(\psi_1)\rangle.\langle Left(\psi_2)\rangle \geq \cos(\varepsilon_{DDT}) \Leftrightarrow \psi_1 \triangleq \psi_2 \tag{6.3.13}$$

The threshold ε_{DDT} defines how much disruption is allowed. In this study ε_{DDT} has been set to 35^o. Experiences have shown that this value offers a disruption big enough not to miss some potential coupling but at the same time, small enough in order to eliminated every unrealistic combinations.

Location of the salient points

A large number of publications and techniques exist on polygonal approximation. A simple technique was used as the accuracy of the approximation is not crucial [16].

Parallelism report

The step four of the algorithm reports any parallelism, however, two verifications need to be done before any positive report can be allowed. After the force coupling phase, C_i and C_j has to pass the following test in order to be considered as parallel.

- For all P, the orientation from $C_i(S_p)$ to $C_i(S_{p+1})$ has to be similar to the orientation from $C_j(f(S_p))$ to $C_j(f(S_{p+1}))$.

  To make sure that the orientation described in this first property fall within the allowed limit, the definition in the prescanning (Equation 6.3.13) was used with the same threshold.

- Curve C_j has to be approximated by lines joining successive $C_j(f(S_p))$ with the same degree of accuracy as curve C_i is approximated by successive $C_i(S_p)$.
  In this second property, the error, of the approximated segment between $C_j(f(S_p))$ and $C_j(f(S_{p+1}))$ by a straight line, is measured. For all points in between $C_j(f(S_p))$ and $C_j(f(S_{p+1}))$, the maximum distance from the chord allowed is:

$$d(f(S_p))_{max} = errorThreshold \times \frac{chordLength_j(f(S_p), f(S_{p+1}))}{chordLength_i(S_p, S_{p+1})} \tag{6.3.14}$$

The value of $d(f(S_p))$ is then compared to $d(f(S_p))_{max}$ (see figure 6.11) to make sure that the condition is satisfied. The values of the errorThreshold is identical to the tolerance of approximation used in the polygonal approximation used to derived the salient point (In this study $errorThreshold = 0.4$).

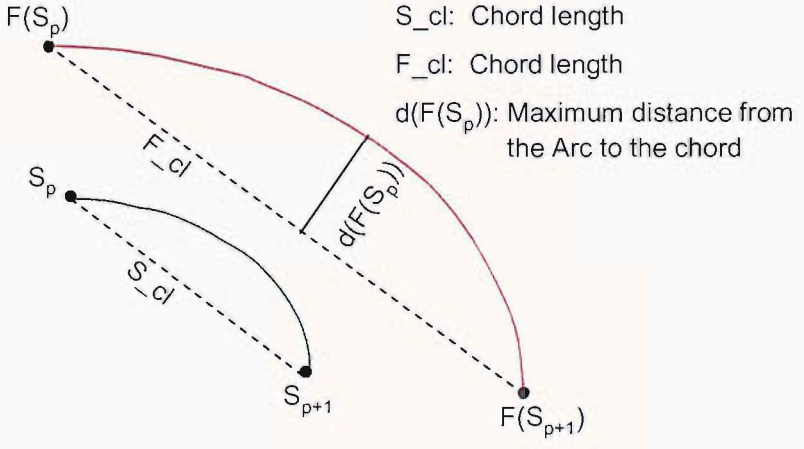

Figure 6.11: Illustration for the approximation role.

6.4 Results

Figure 6.13 shows the overall procedure applied to the image in order to achieve our goal: finding the edge from an internal wave signature. Results from this method can be seen in figure 6.14 for the image25 and figure 6.15 for the image0. In these two figures, the decomposition into simple segments is also presented, this is the initial step of the parallelism detection. The detection of the internal wave edge in the two images is good. Once again the detection is better for the image0 than for the other study case. This difference of detection can be explained simply by the fact that the signatures present in image0 are very strong and produce nice and clear edges. However when the edges can be traced in image25 the result is correct and gives a good appreciation of the extend of the wave. For very weak signatures however such as the ones in the right top corner, it has been impossible to find three edges parallel. The experience has shown that two parallels edges have been found but following our model criteria this is not enough to classify them as part of an internal wave signature.
Table 6.3 show the result of the classification. As before the total accuracy, the error of misclassification of both classes is calculated. The classification accuracy was calculated using the following simple approach:

- Around every pixels part of a selected edge, a window of 10×10 pixels is set to 100%,the rest to 0% (see figure 6.12).
- The image is then divided into sub-image as before and their respective probability calculated as follows:
  - 100% if the mean of this zone is superior to 50%
  - 0% otherwise.
- Then the confusion matrix can be calculated.

This translation from the edge extraction and classification to a sub-image representation offers a direct comparison with previous results. Looking at the result shows that the error for the miss-classification of the event zone is relatively high. This problem arises from the fact that the edge recognition technique is a lot stricter in the identification of a boundary of the internal wave than the human eye. But the results offer otherwise a very good classification: every zone classified as an internal wave really is an internal wave signature. So one can be very confident in the interpretation of the

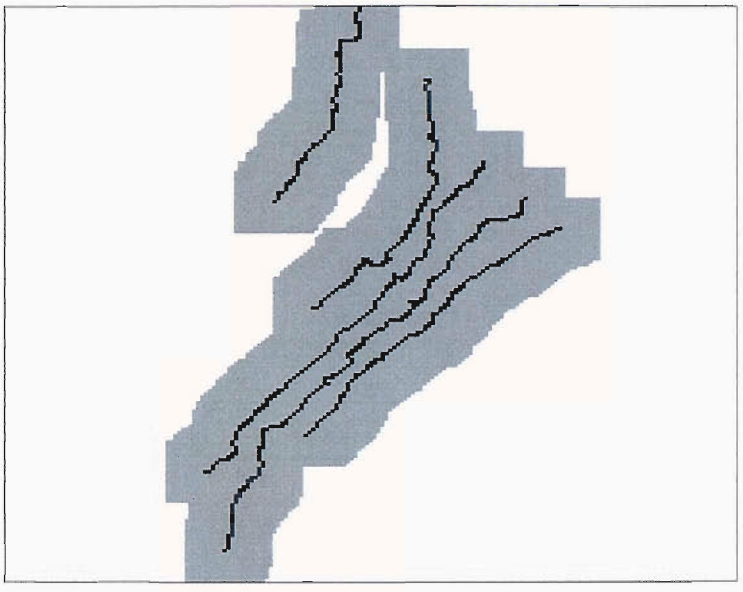

Figure 6.12: Example of the pixels selection. In black are the edges identified as part of an internals waves. In gray are the pixels selected using a 10×10 windows around each point of the edges.

result. This confidence is a lot higher than for the previous classification made during

Image 0

	Non-Evt	Event
Non-Evt	189	5
Event	4	27

96.0% of total accuracy
12.9% of error on event class
2.5% of error on non-event class

Image 25

	Non-Evt	Event
Non-Evt	161	5
Event	9	47

93.6% of total accuracy
16.0% of error on event class
3.0% of error on non-event class

Table 6.3: Confusion matrix and accuracy of the classification in percent

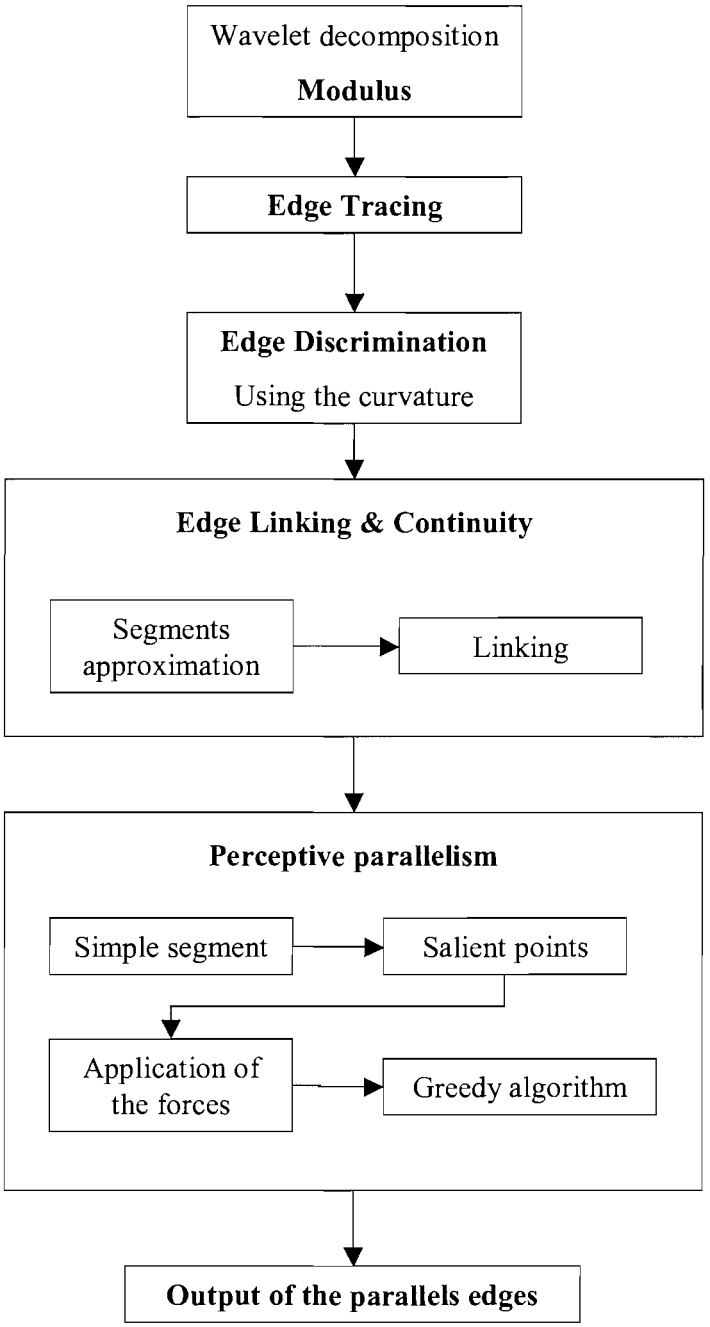

Figure 6.13: Overall procedure for the edge analysis

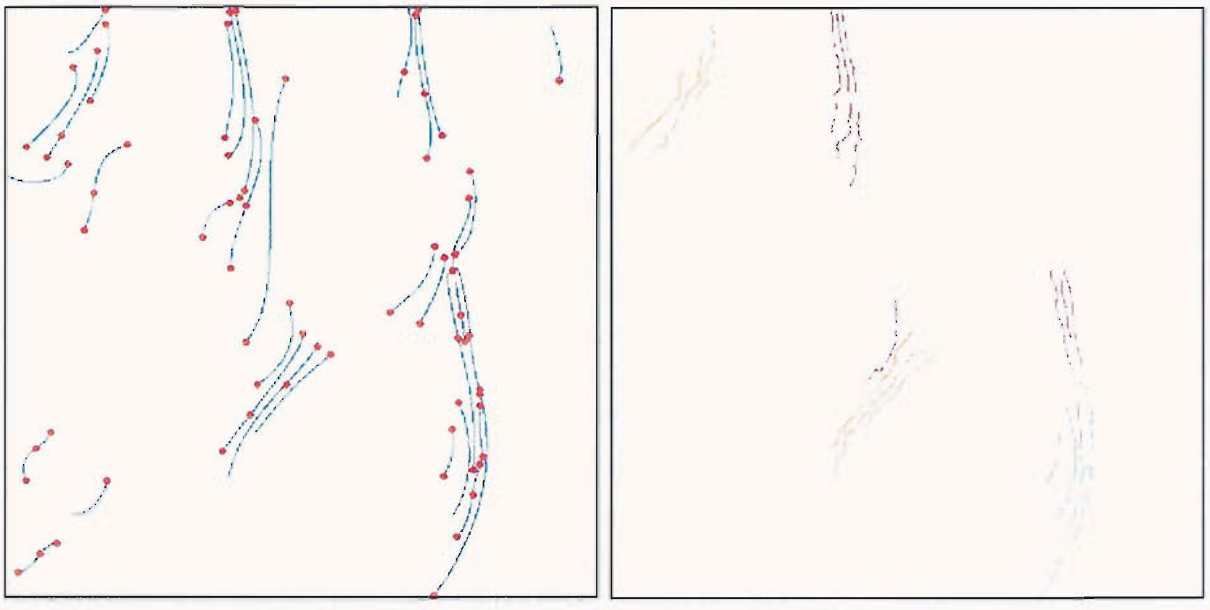

(a) Simple segments (b) Triplet of parallel edges

Figure 6.14: An example of applying the algorithm to the image 25. (a) show the totality of the simple segments. (b)Show the simple segment that are a least parallel

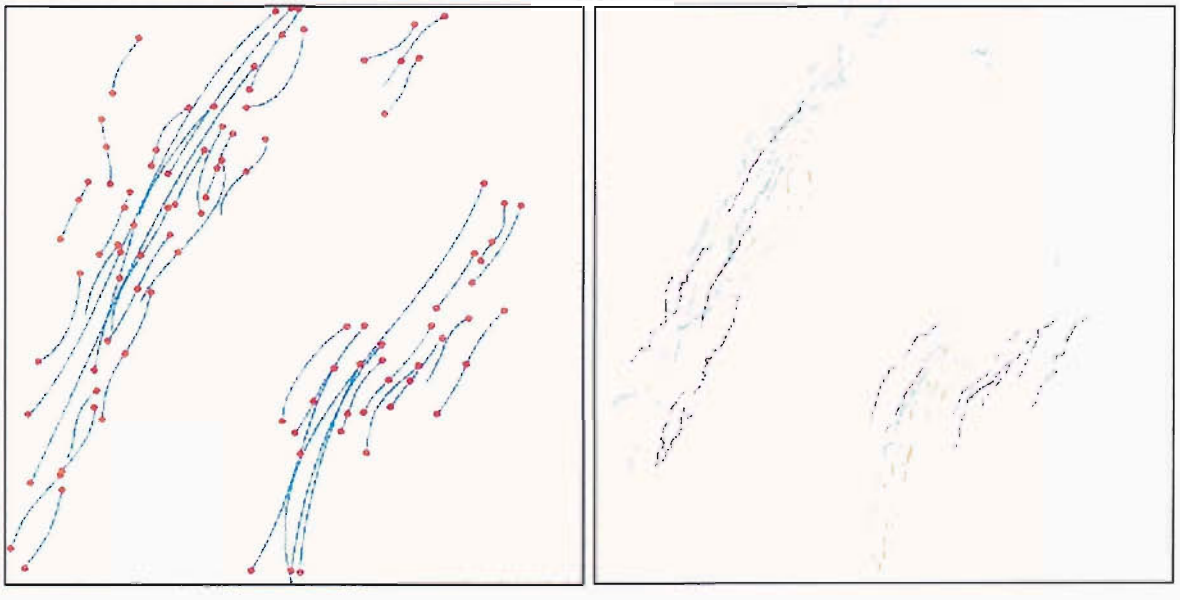

(a) Simple segments (b) Triplet of parallel edges

Figure 6.15: An example of applying the algorithm to the image 0. (a) show the totality of the simple segments. (b)Show the simple segment that are a least parallel to two other simple segment.

6.4.1 Analysis of the signature

Once there is confidence in the correct classification of an event class, the information given by the edge can be used to extract some primary characteristic of the internal wave itself.

Because every internal wave signature that been identified is made up of at least three edges it is very easy to calculate the mean curvature of the triplet and from it the wave direction of propagation. The propagation is oriented away from the centre of curvature. The curvature is calculated using the salient point of the edges and from it, the mean centre of curvature is derived by the projection of the vectors in image space and finding their intersection. This point and the set of points which represent the middle of each edge a line is interpolated. From this line and the horizontal (image axes) the angle of propagation can be inferred. Figure 6.16 shows the two case studies images with arrows representing the approximate sense of propagation.

From the same selected edge it is possible to find the wavelength of the solitons that compose the wave. By taking a transect along the line of propagation interpolated earlier on the original image, it is possible to extract the backscatter of the images across the internal wave [36]. The backscatter is then normalized by the mean backscatter of the image. From it a frequency representation of the transect is calculated using a wavelet decomposition. Figure 6.17 and 6.18 give two example of the profile with the wavelength of the internal wave for image25. The same can be see in figure 6.19 for the image0. The position of the transect can be see in figure 6.16. From these transect it is possible to comment on the type of signature. Here the signature is a $+/-$ signature as detailed in the first chapter and is the result of an hydrostatic interaction.

From the knowledge of the position of the internal wave's solitons it would be possible to make a deeper analysis of the wave if one had the tide time table, the mixed layer depth, or/and the bathymetri, etc... For example with more knowledge of the area it is possible to use the free homogeneous KdV equation, which describe the evolution of the wave profile to model the wave.

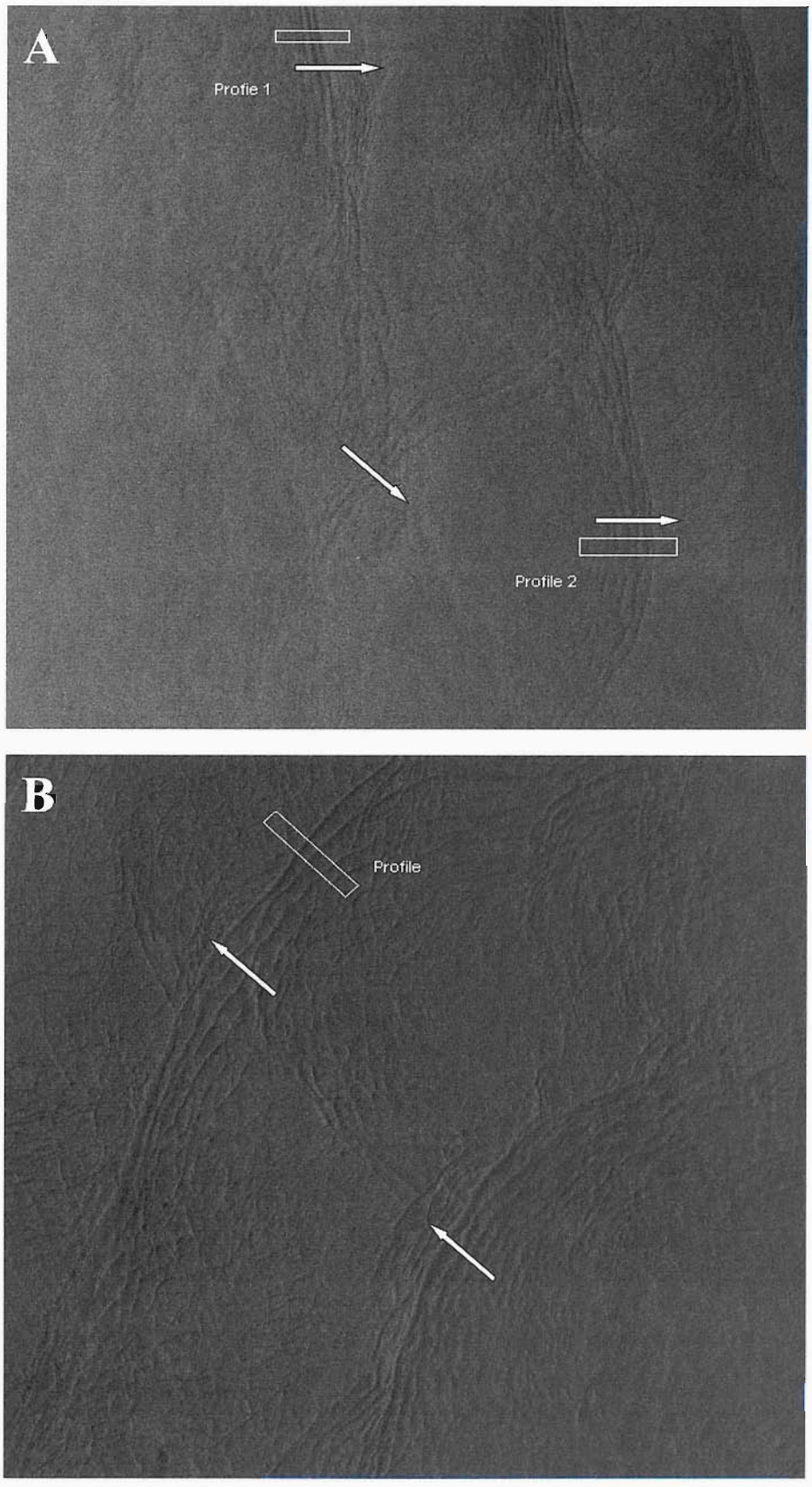

Figure 6.16: Position of the transect used and direction of propagation of the waves. (A)Image25. (B)Image0

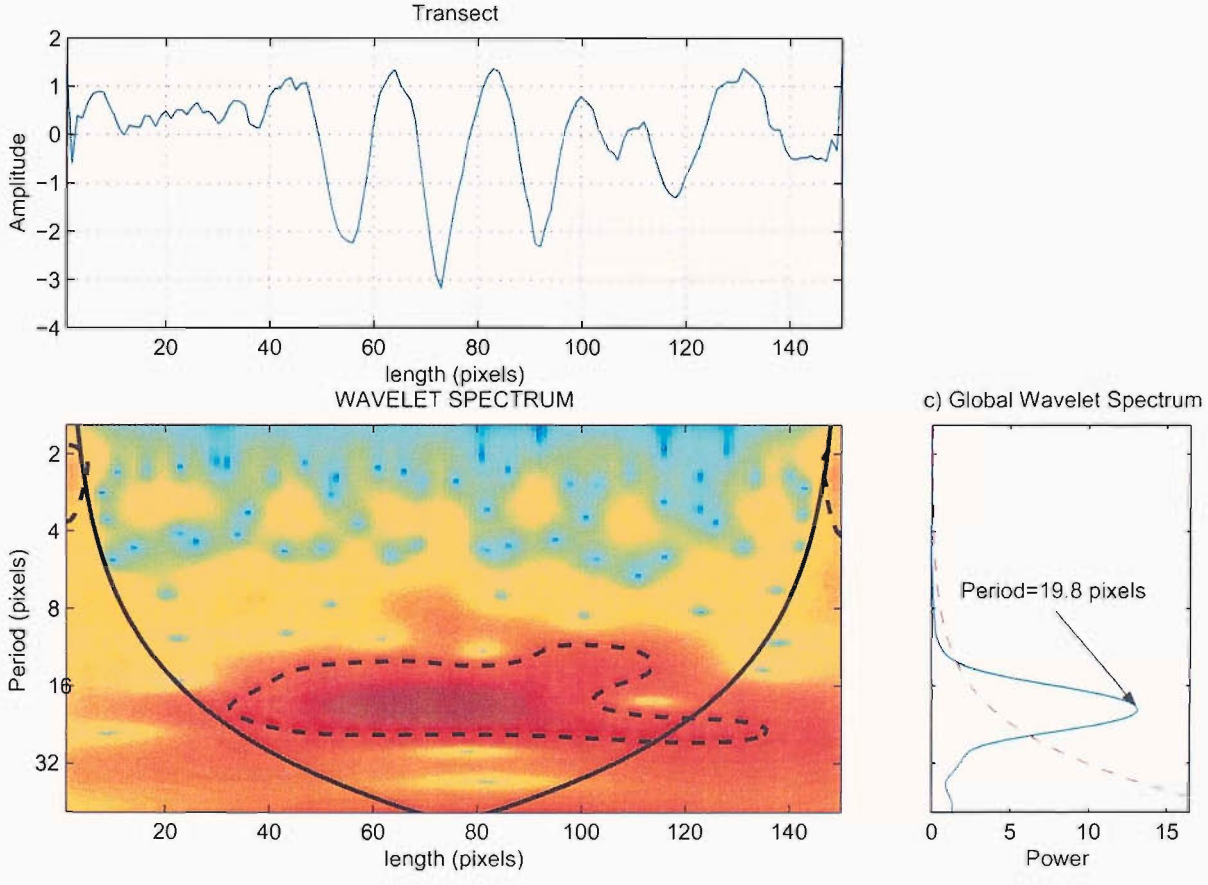

Figure 6.17: Spectrum using wavelet decomposition for the profile 1 of the image25. The dotted line represent the 95% level. Here the period is equal to 19.8 pixels which correspond a wavelength of $1.980Km$

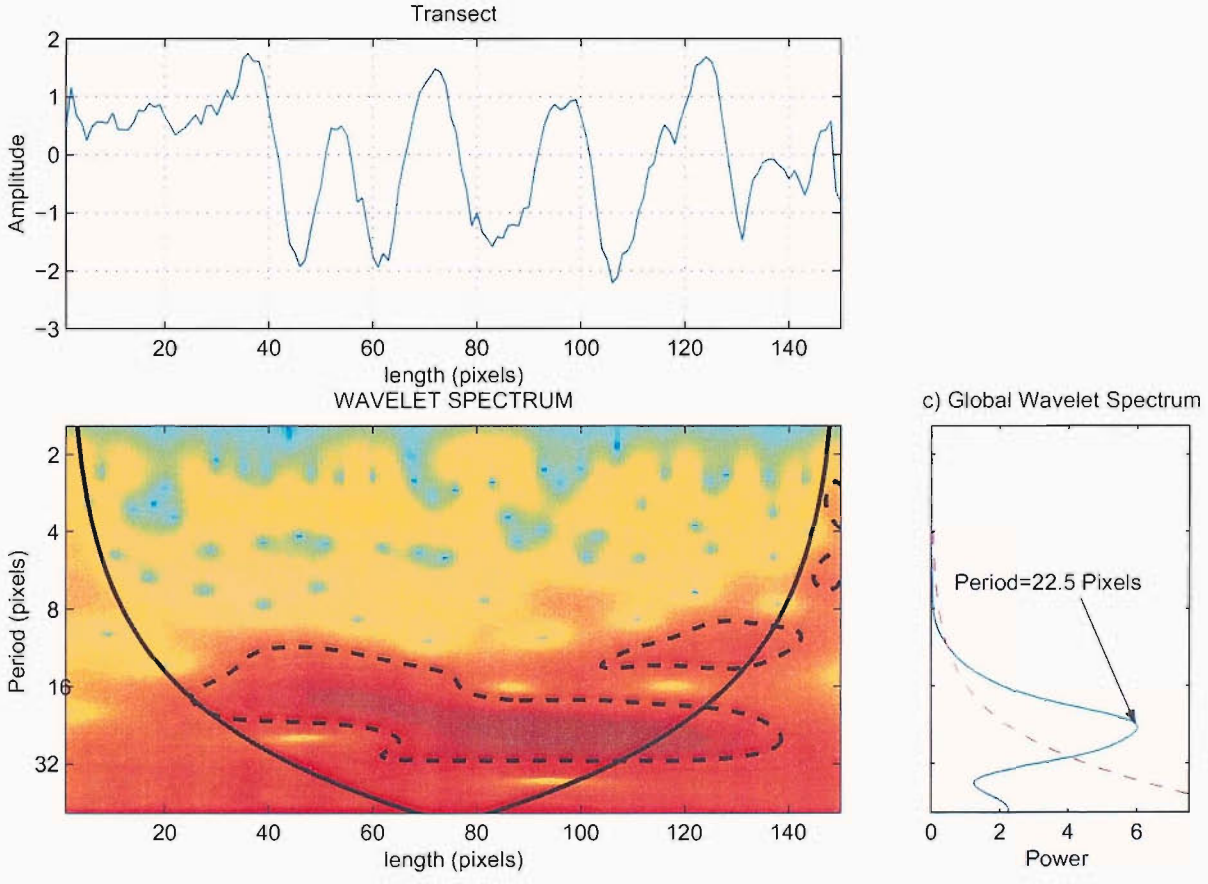

Figure 6.18: Spectrum using wavelet decomposition for the profile 2 of the image25. The dotted line represent the 95% level. Here the period is equal to 22.5 pixels which correspond a wavelength of $2.250Km$

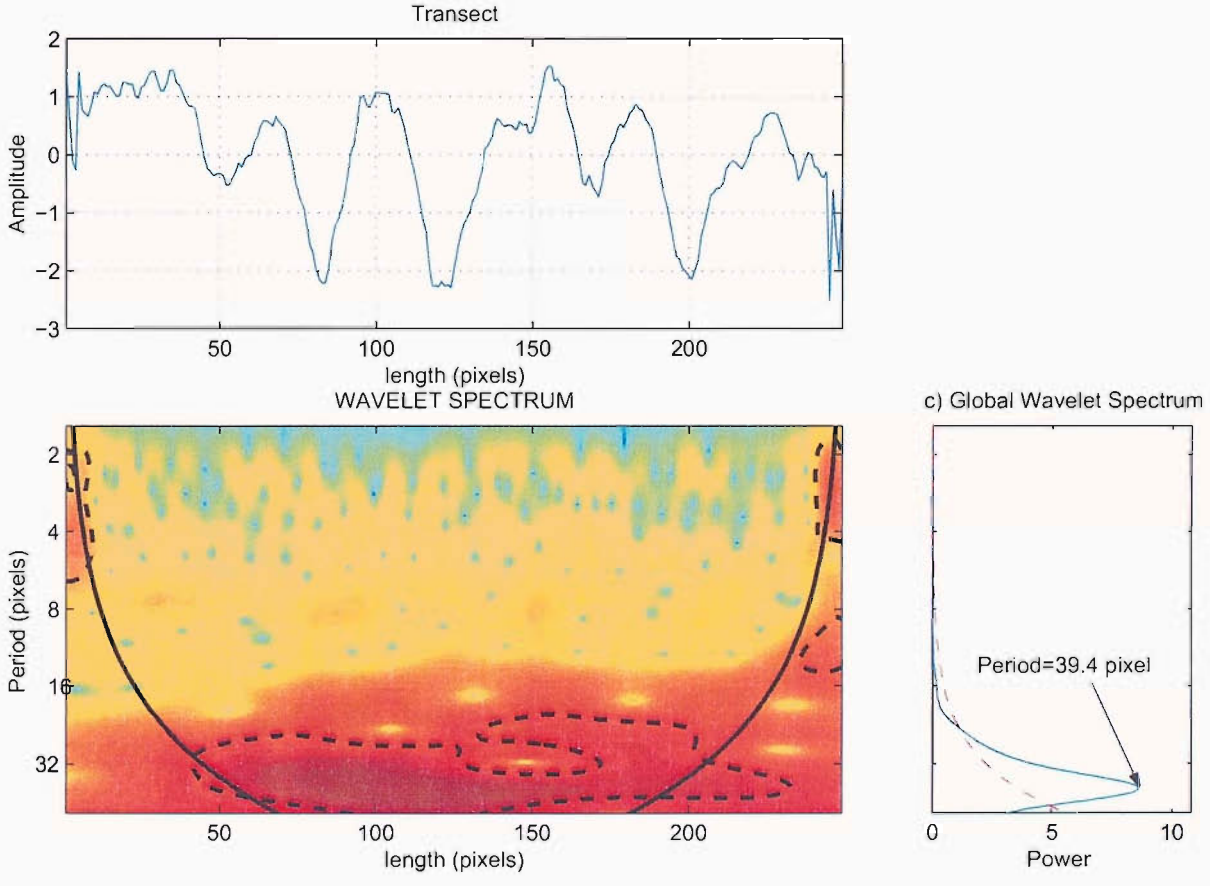

Figure 6.19: Spectrum using wavelet decomposition for the profile 1 of the image0. The dotted line represent the 95% level. Here the period is equal to 39.4 pixels which correspond a wavelength of $3.940Km$

6.5 Conclusion

We have shown using a totally different approach that the internal wave signature can be recognizable by studying the geometry of the edges present in the image. This approach provides good confidence level for the detection of internal wave, as it has a strong dependency on the number of edges needed and their position. From this technique we have shown that the knowledge of the position of the edge can be used to determine primary information about the wave, such as its wavelength and sense of propagation. Using the transect across the wave it is possible to comment on the type of signature as well.

Chapter 7

Applications of the Internal Wave recognition schemes

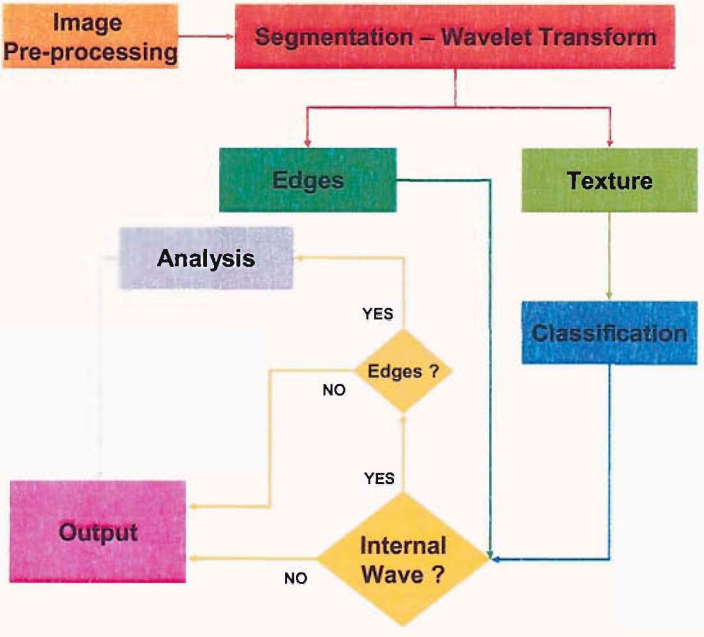

Figure 7.1: Diagram illustrating the layout of the processing

7.1 Introduction

The aim of this research was to move from a subjective manual detection of internal waves toward a computed interpretation of the grey scale level of the images. Such detection will ease the workload as well as decrease the cost of the processing by reducing the manpower. Furthermore the scheme presented in this work offers a first step towards providing an objective rather than a human interpretation of the SAR images. It does provide the possibility to characterise the different type of signatures. To do this, a

series of processing and classification systems have been developed.
The processing can be divided into two categories: the use of texture to make the discrimination and the analysis of the geometry of the edge found in the image (see table 7.1). Both categories use the output of the wavelet multi-resolution analysis technique to filter out the possible internal wave signature.

1. Textural analysis of the image.
   - Gray Level co-occurrence matrix
     Representation of the textures
   - Classifications:
     - PCA: Use the GLCM as input.
     - KNN: Use the statistical indexes as input.
       Do not need of any training.
     - MLP Use the statistical indexes as input.
       Need of any Training.
2. Geometric analysis of the edge found within the image.
   - Edge tracing technique:
     Using an hysteresis threshold.
   - Discrimination using the edge curvature and size
   - Parallelism technique

Table 7.1: Overview of the techniques used.

The optimization and parameterisation of the different step of each processes used have been explained in the previous chapters. It is however necessary to note that in the application of the scheme, the PCA classification will not be used. The reason is that this approach cannot be made fully automatic. The threshold required for the classification cannot be adjusted automatically. As one of the objectives of this work is to create an automatic recognition technique, this technique was not retained.

7.1.1 Characterization of the signature using texture

Before any classification scheme can be used, it is necessary to characterize the object to be classified in the simplest manner possible. In this work it has been proposed to do this using the Grey Level Co-occurrence matrix representation. From the GLCM,

statistical indexes can be derived, which represent the organization of the grey level in these regions. Using these indexes, six values can be used to characteristic an event i.e the presence of an internal wave signature or a non-event. This discrimination approach needed three values to be set, they are: the size of the studied zone, the number of grey levels, and the displacement used in the make up of the GLCM. This technique was presented in chapter 4 and the values retained were:

- The size of the studied zone: 64×64 pixels
- The number of colours: 32
- The displacement: $3 - 5$ pixels

7.1.2 The classifiers

Now that the Event, Non-event zone can be represented by six parameters, the need for a decision making tool is necessary. In chapter 5 three classifiers technique were presented: The PCA, the KNN and the MLP. It has been stated that the first of these three techniques will not be applied here, because of its incapacity to be automated.

KNN: The objective of the KNN is to find the k nearest neighbours of an unidentified test pattern within a hyper-sphere of predefined radius in order to determine its true class. The classification from a KNN is dependent on two things, excepting the set of known vectors: the length of the input vector and the number of neighbours used. To determine these parameters a series of tests for accuracy have been carried out using the two case studies (image0 and image25), for different setups. Along with the setup of the KNN different wavelet representations have also been tested.

- Length of the input vector: 3
- Number of neighbours used: 3
- Best wavelet representation: mXY

MLP: The MLP classifier uses a training set where all the classes are correctly represented to determine and learn the relationship between classes. The MLP, in this study uses the same training set as the KNN and as for the KNN some parameters in its construction need to be set. The first parameter is the architecture: i.e. the number of input nodes, layers and output nodes. The second important aspect of the

construction is the training. The MLP needs to determine a generalization rule to discriminate between classes. The training needs to be long enough to enable the learning process but not too long; otherwise the generalization is not sufficient. To perform the optimized construction a series of tests using different configurations and looking at the mean square error was made. It was necessary to perform the test to see which wavelet representations were producing the best classification. I was found that the best configuration was:

- Number of input nodes: 6
- Number hidden layer and nodes : $1 - 12$
- Number of output node: 1
- Best wavelet representation: XY

7.1.3 Geometric analysis approach

The geometrical analysis uses a totally different concept. Here, the edges present in the image, rather than the texture representation are investigated. The goal is to identify which edges are parts of an internal wave signature and which are not. The starting point was to apply an edge tracing technique using a hysteresis threshold on the second level modulus. Then a series of tests on the curvature and direction of the edge were performed to eliminate some and join others. When only significant edges were remaining a procedure to determine their mutual parallelism was applied. The last step was to retain only edges, which were parallel with at least two other edges. From here it was then possible to extract information from the edge such as the direction and wavelength of the internal wave signature.

7.2 Results of the application

In this part of the work, the above techniques are applied to several unseen images and the accuracy and the robustness of the classification are measured. The results from six images, enables the successes and the problems of the approaches in classifying internal wave signatures on SAR images to be illustrated.

The images: The images used here are named as images A to E. They like the two cases study, are made from a zone of 512×512 pixels selected from an original SAR image. Table 7.2 details the information of the original image from which the six image are coming from and figure 7.2 show their location on a bathymetric plot. Figure 7.3, 7.4, 7.5, 7.6, 7.7, 7.8 show the different images and their masks.

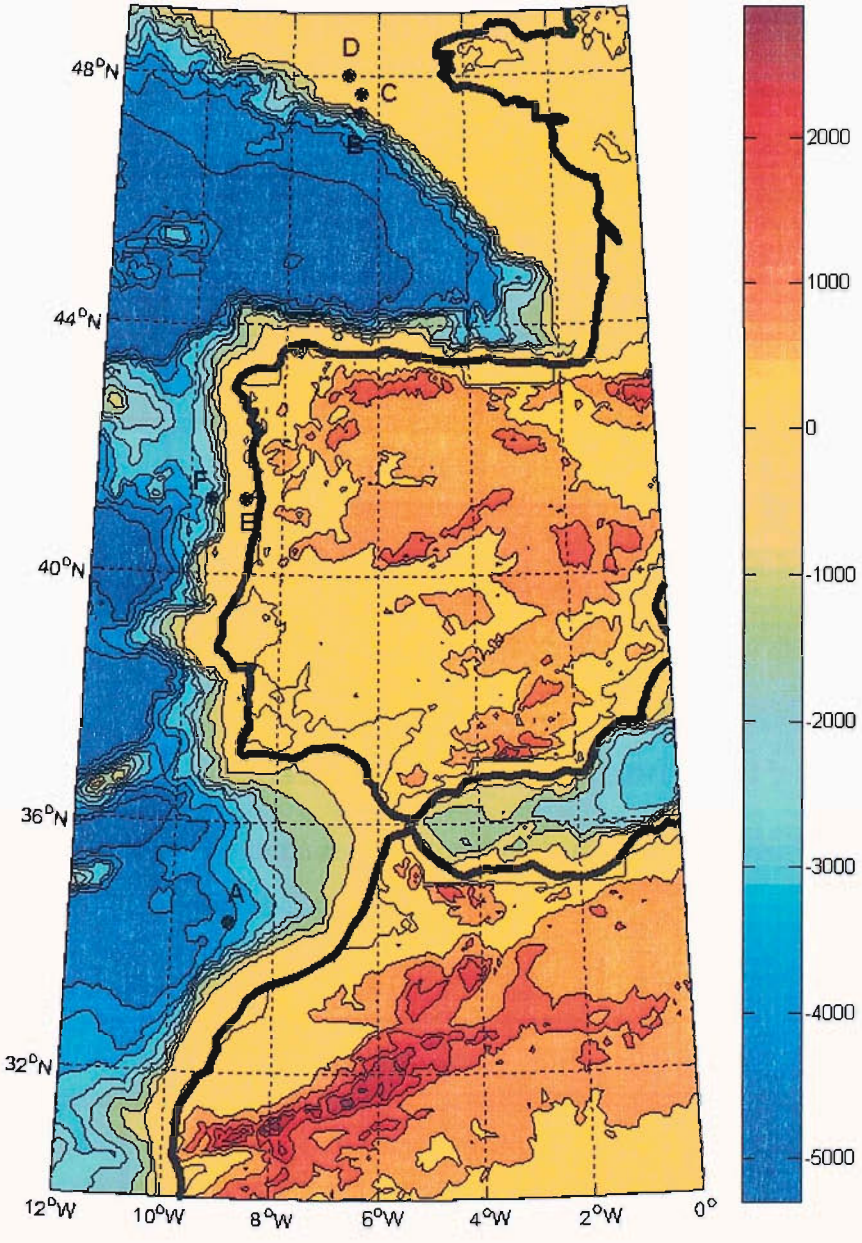

Figure 7.2: Bathymetry plot and location of the images

	Image A	Image B	Image C	Image D	Image E	Image F
Orbit	16594	27596	27596	2781	12194	11965
Frame	2853	0945	0945	2637	0819	0819
Lat	37.4	47.4	47.7	48	41.21	41.25
Long	351.1	353.3	353.6	353	-8.8	-9.56
Date	17-09-94	30-07-00	2-08-00	18-08-00	19-8-97	3-08-97
Time	11 :18	22:34	11 :20	11 :16	22:49	22 :52

Table 7.2: Information of the original images

7.2.1 The classifications using the KNN and MLP:

The classification uses the optimimum setup for the MLP and the KNN. The result can be seen in table 7.3. It is clear that the results are mixed.

	Image A		Image B		Image C		Image D		Image E		Image F	
	MLP	KNN	MLP	KNN	MLP	KNN	MLP	KNN	MLP	KNN	MLP	KNN
Total accuracy	81.7	80.8	75.6	76.8	81.3	80.4	76.0	72.4	86.2	85.3	82.2	82.2
Event error	13.5	21.6	19.5	31.7	0.0	0.0	20.9	25.5	0.0	4.3	14.6	19.5
N-Event error	19.1	18.6	25.5	21.1	20.6	21.6	24.7	28.0	15.3	15.8	18.4	17.4

Table 7.3: Accuracy of the KNN and MLP classification for the six images. The red value represent a good classification. The red values represent classification with a total accuracy above 80%, whereas the green for a total accuracy below 80%. See the corresponding confusion matrix in appendix C, figure C.1

Image A: This image come from an original SAR scene taken in late summer 1994, with a central coordinate equal to 37.4 degree north by 351.1 degree west. This places

the image in the Liberian region (offshore of Portugal). The time of the acquisition and the presence of internal wave coincide with the statistical study of Dokken [23]. The image can be seen in figure 7.3(b), and its mask[1] (figure 7.3(a)) show clearly the presence of the internal signature . Except for the internal wave signature the zone of study is quite featureless with a background of the backscatter almost uniform. The internal wave signature is orientated vertically with respect to the image axis.

The classification shows an accuracy of above 80% for both classifiers with a better performance of the MLP than the KNN. The difference of the two classification come from the missclassification of the events class, which is larger in the KNN result (21.6% compare to 13.5% for the MLP). This difference in accuracy comes from the definition of the internal waves representation used. In the case where the internal waves signatures are mainly oriented along one axes of the image, the XY representation and subsequently classification has a better accuracy on event class (see chapter 5), as each orientation are classified independently, and combined together to give an total classification. Because the KNN uses the mXY wavelet representation and the MLP the XY representation, it will be fair to say that the internal wave orientation is better understood by the second configuration. The classification can be seen in figure 7.4(b), 7.4(c) and 7.4(d)

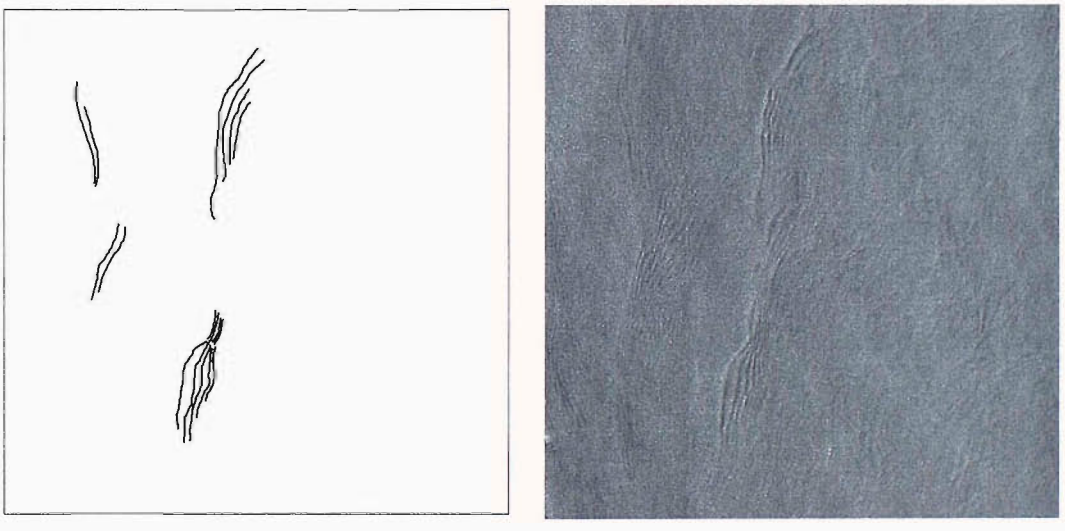

(a) Mask (b) Image

Figure 7.3: Image A

[1]The mask of a given scene shows a sketch of the internals waves signatures present in the scene.

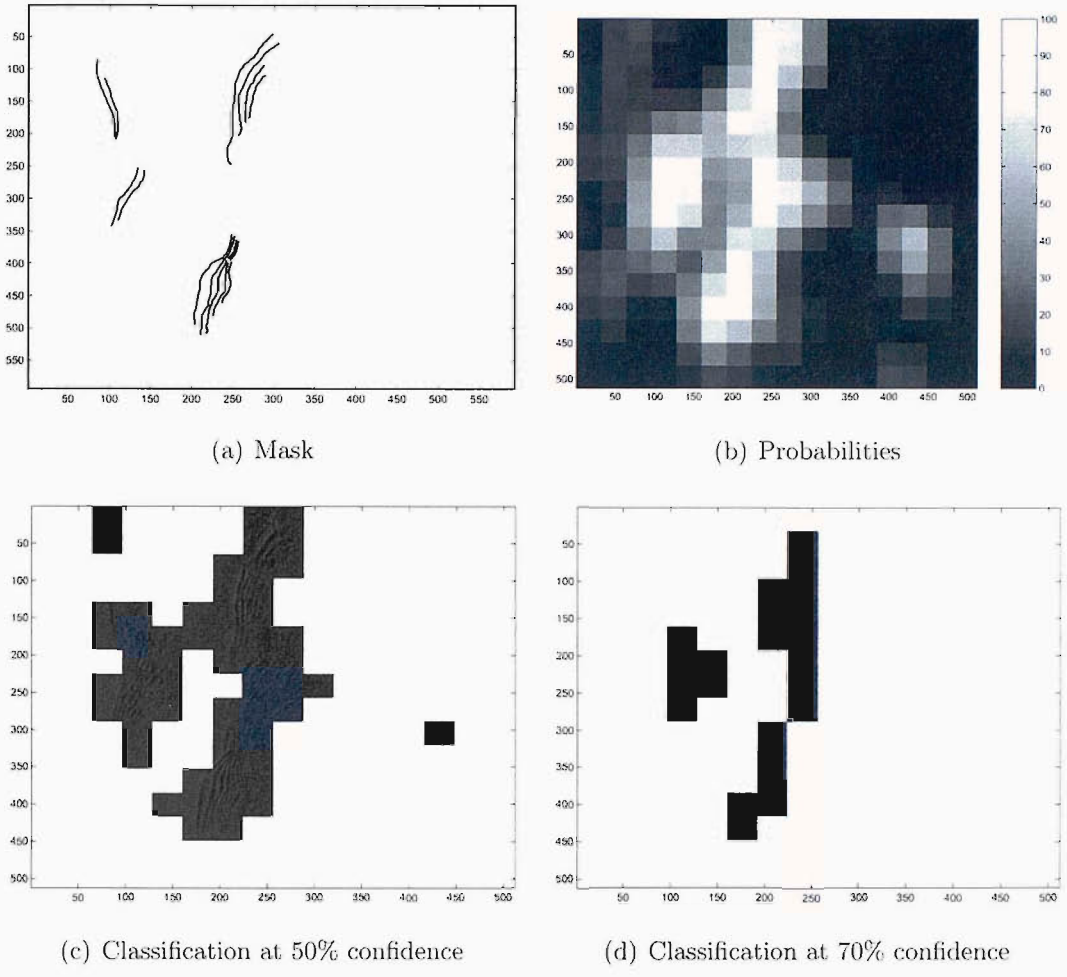

(a) Mask

(b) Probabilities

(c) Classification at 50% confidence

(d) Classification at 70% confidence

Figure 7.4: Image A classification using the MLP classifier. (a) Mask of the internal wave present (visual interpretation). (b) Map of percentage probability of internal wave presence in the image. (c)-(d) classification using two different threshold.

Image B: This image come from an original SAR scene taken in summer 2000, with a central coordinate equal to 47.4 degree north by 353.6 degree west. This places the image in the Bay of Biscay (offshore of France). The time of the acquisition and the presence of internal wave coincide with the statistical study of Dokken [23]. The image can be seen in figure 7.5(b), and its mask (figure 7.5(a)) show clearly the presence of the internal signature. In this case the internal wave signatures are complex and both vertically and horizontally oriented respect to the image axis. Some zone of interaction between the internal wave can be seen in the middle part of the image. In addition to the internal wave signature the backscatter from other region is complex as well. Large regions of rough surface can be seen. The cause of this roughness is not very clear. It can be linked to a high sea state, but there is no presence of swell. It may be the presence of a very strong dynamical process that occurs at a small scale, along with

attenuated internal wave signature. In such a case it is difficult to clearly define the boundary of the internal signature on part of the image.

The classification shows an accuracy of above 80% for both classifiers with a better performance of the KNN on none-event classes (25.54.6% compare to 21.19% for the KNN) whereas the MLP show a better accuracy for the event classes (21.6% compare to 13.5% for the MLP). The difference in accuracy for both event and none-event classes come from the complexity of the internal waves signatures in the images as well as the different configuration used. In the case of the XY representation, the classification is more sensitive to the variation of gray tone, but miss-classified to much zone with strong roughness, which are not due to internal wave signature, whereas in the case of the mXY classification, the sensibility over the gray tone is too much reduce, which decrease the accuracy for the event classes. In such image, the choice of the configuration and classifier used is totally dependant of the type of accuracy wanted. Depending on the type of application, one would prefer having a better accuracy for the event or the none-event.

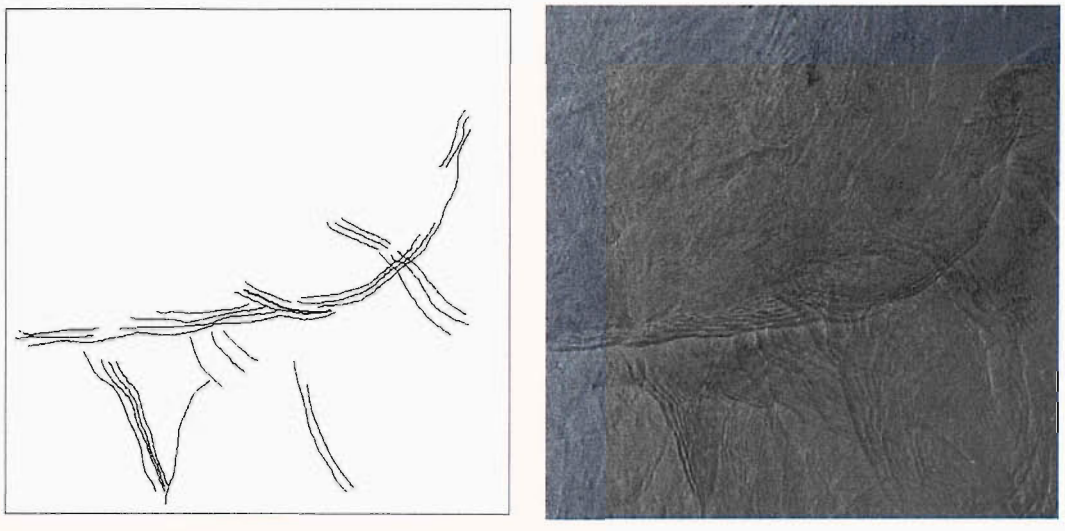

(a) Mask (b) Image

Figure 7.5: Image B

Image C: This image come from an original SAR scene taken in late summer 2000, with a central coordinate equal to 47.7 degree north by 353.6 degree west. This places the image in the Liberian region (offshore of Portugal). The time of the acquisition and the presence of internal wave coincide with the statistical study of Dokken [23]. The image can be seen in figure 7.6(a), and its mask (figure 7.6(b)) show clearly the

presence of the internal signature. Expect for the internal wave signature the zone of study is quite feature less with a background of the backscatter almost uniform. The internal wave signature is orientated diagonally respect to the image axis.
The classification shows an accuracy of above 80% for both classifiers with a marginally better performance of the KNN than the MLP. The difference of the two classification come from the miss-classification of the non-events class, which is larger in the MLP result (20.5% compare to 19.5% for the KNN). As before the XY representation, offer the best representation of the various internal wave orientations. In a case where the internal wave is diagonally oriented, both wavelet X- and Y-decomposition will have some of its representation. Taking the mean of these decompositions seems to reinforce the signal. It should be note that in this case the error for miss-classification of the event class is null. This result can be explained by the well defined boundary of the internal waves present in the images, a homogeneous background and a good representation in the training set.

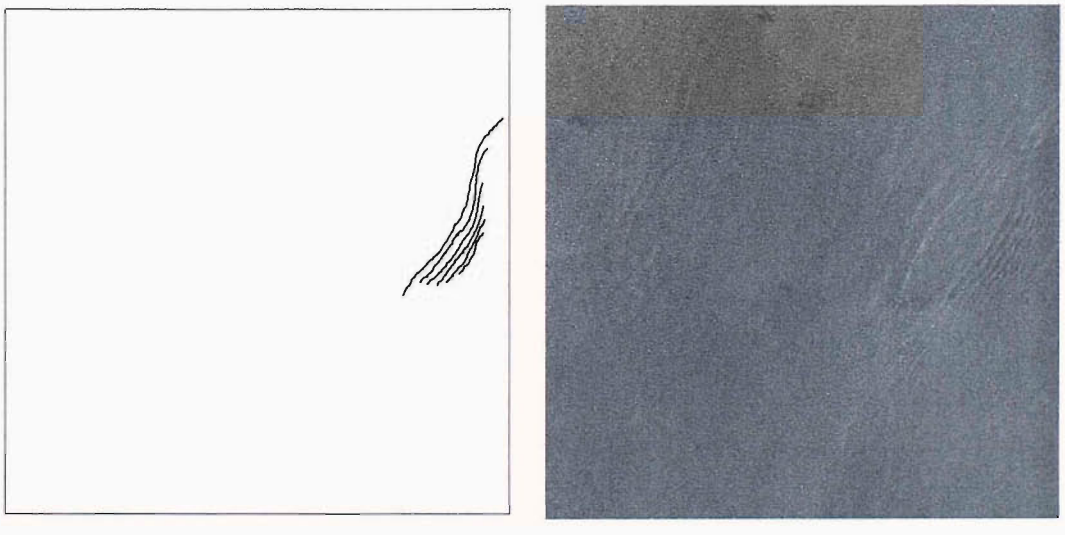

(a) Mask (b) Image

Figure 7.6: Image C

Image D: This image come from an original SAR scene taken in late summer 2000, with a central coordinate equal to 48 degree north by 353.3 degree west. This places the image in the north of Bay of Biscay (offshore of France). The image can be seen in figure 7.7(b), and its mask (figure 7.7(a)) show clearly the presence of the internal signature. In this case the internal wave signatures are complex and vertically oriented with respect to the image axis. Some zone of interaction between the internal waves

can be seen in the middle part of the image. Four internal waves signatures can be identified, three of them going from the left to the right, and the last one going from the right to the left which interacts with the first signature. In general the backscatter is complex as well. A large region of shadow wind can be seen in the bottom of the image. Again in such a case it is difficult on some part of the image to clearly define the boundary of the internal signature.

The classification shows an accuracy of below 80% for both classifiers with a better performance of the MLP than the KNN. In this case the large difference in accuracy of the classifications come from the miss-classification of the events and the non-event class, which is larger in the KNN result (25.5% compare to 20.9% for the MLP for the event class and 28% compare to 24.7% for the MLP for the non-event class). Both wavelet representations give a bad result.

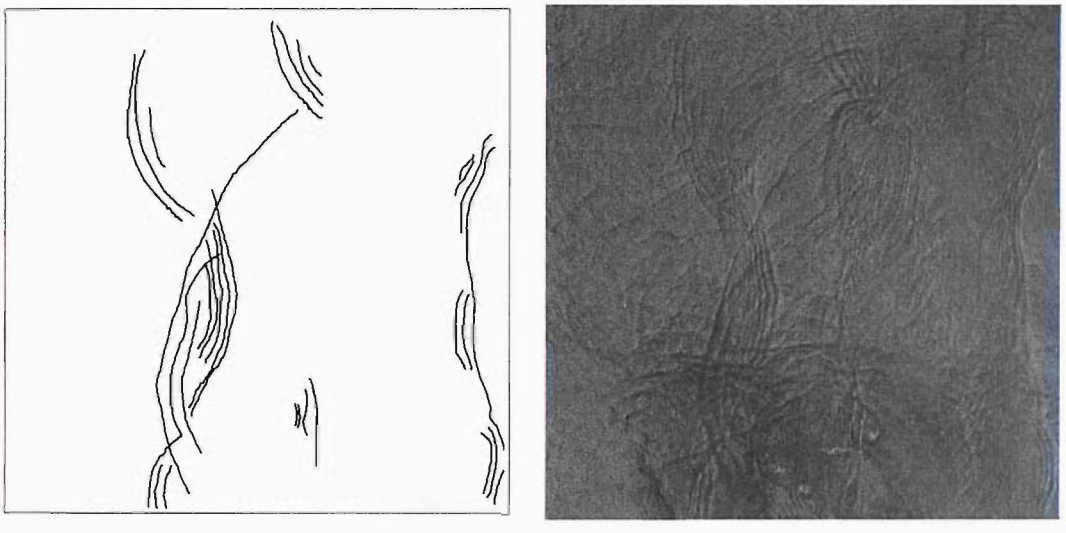

(a) Mask (b) Image

Figure 7.7: Image D

Image E: This image come from an original SAR scene taken in August 1997, with a central coordinatê equal to 41.2 degree north by -8.8 degree west. This places the image in the Liberian region (offshore of Portugal). The image can be seen in figure7.8(a), and its mask (figure 7.8(b)) show clearly the presence of one internal signature which is vertical oriented respect to the image axis. Expect from the internal wave signature the zone of study is quit feature less, dominated by shadow wind, with a background of the backscatter almost uniform.

The classification show an accuracy of above 80% for both classifier with a better

performance of the MLP than the KNN. The large difference of the two classification come from the miss-classification of the non-events class, which is larger in the KNN result (20.1% compare to 15% for the MLP). The error of miss-classification equal to not for the event class and the uniform background and the strong presence of the signature can explain the good classification. It is in this case easy to determine the boundary of the wave. The orientation of the wave is better suited to the XY wavelet configuration rather than the mXY. The wave being vertically oriented does not present any signal for the Y-decomposition and therefore alter negatively it presence when the mean of the two decompositions are made. The classification can be seen in figure 7.9(b), 7.9(c) and 7.9(d)

(a) Mask

(b) Image

Figure 7.8: Image E

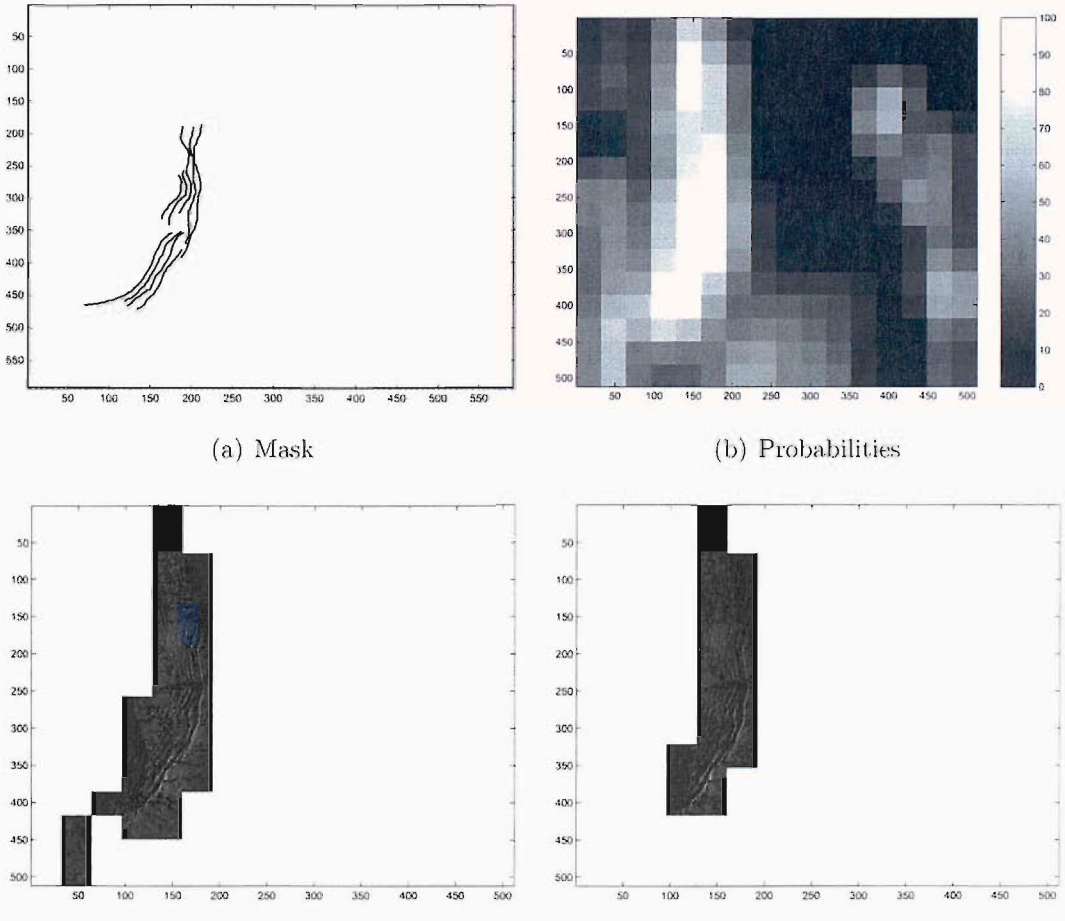

(a) Mask

(b) Probabilities

(c) Classification at 50% confidence

(d) Classification at 70% confidence

Figure 7.9: Image E classification using the MLP classifier. (a) Mask of the internal wave present (visual interpretation). (b) Map of percentage probability of internal wave presence in the image. (c)-(d) classification using two different threshold.

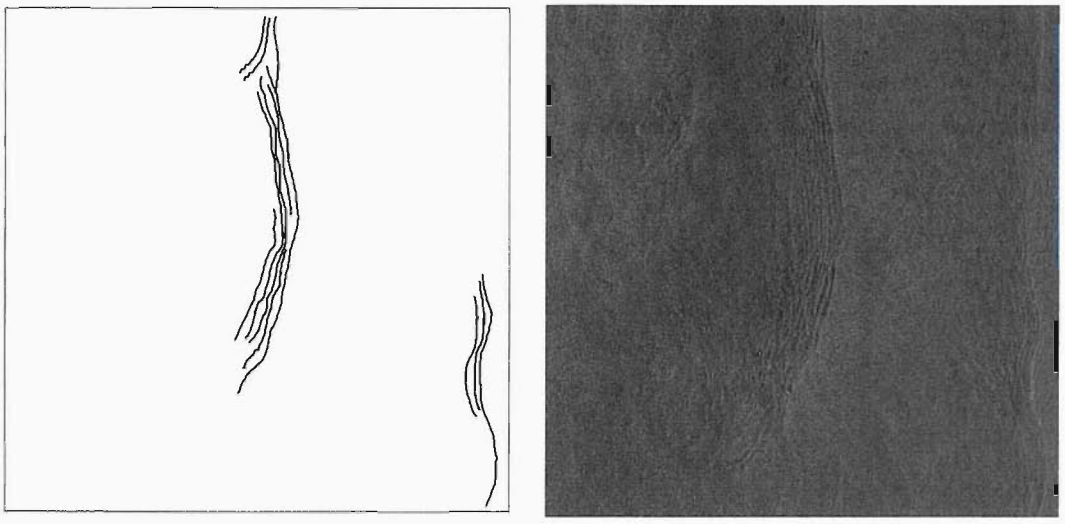

(a) Mask (b) Image

Figure 7.10: Image F

Image F: This image come from an original SAR scene taken in August 1997, with a central coordinate equal to 41.2 degree north by −9.5 degree west. This places the image in the Liberian region (offshore of Portugal). This image is very close to the previous case. The image can be seen in figure 7.10(a), and its mask (figure 7.10(b)) show clearly the presence of two internal signatures which are vertical oriented respect to the image axis. Expect from the internal wave signature the zone of study is quit feature less, with a background of the backscatter almost uniform. This image is also very similar for the study case image25.

The classification show an accuracy of above 80% for both classifier with a better performance of the MLP than the KNN. The large difference of the two classification come from the miss-classification of the events class, which is larger in the KNN result (24.4% compare to 15.2% for the MLP). It is in this case easy to determine the boundary of the wave. The orientation of the wave is better suited to the XY wavelet configuration rather than the mXY. The wave being vertically oriented does not present any signal for the Y-decomposition and therefore alter negatively it presence when the mean of the two decompositions are made.

Conclusion

In this section two different classifiers with their own configurations have been applied to different SAR images to illustrate their potential to generate accurate recognition. The classifications produce by the MLP are in general more accurate than the ones from

the KNN. But the MLP like the KNN fails to give correct classification when complex features and/or busy background are present in the image. This failure could be partly overcome by using a larger training set.

7.2.2 Edge detections and parallelism study

In this part of the application chapter, a totally different approach has been taken, by looking at the edge present in the images. The method is detailed in chapter 6 and an overview of the processing can be seen in table 6.13. The probability of occurrence of internal wave signature are calculated using the same simple approach as described earlier, and can be seen in table 7.4. A visualization of the selected edges can be seen for the image $A-B-C-D-E-F$ in figures 7.11(b),7.12(b),7.13(b), 7.14(b), 7.15(b) and 7.16(b) respectively.

The total accuracy (table 7.4) show a net improvement compared to the previous classification shown in table 7.3. This difference can be attributed to the low error on the miss-classification of the non-events. However, despite these good results the error on miss-classification of the event class is higher that previously. This error is the result of very strict roles in the determination of the internal wave's signature. The edge detection technique produces much narrower boundary than the other classification, which increase the confidence level on event classification.

As before the complexity of the classified image is an important factor. The simpler the feature within the image, the more the classification gives a good result. The strength of the signature is important as well. The more the internal wave is strongly represented in the image the more chance there is of detecting it. These problem can be identified by comparing the result of the image E or F (figure 7.15(b) and 7.16(b)) to the other image (figure 7.11(b),7.12(b),7.13(b),7.14(b)).

	Image A	Image B	Image C	Image D	Image E	Image F
Total accuracy	88.5	83.1	95	79	97	93.3
Event error	40	57.8	30	69.1	25.2	25.1
N-Event error	7	8.15	3.2	12.6	0	1.8

Table 7.4: Accuracy of the edge detection

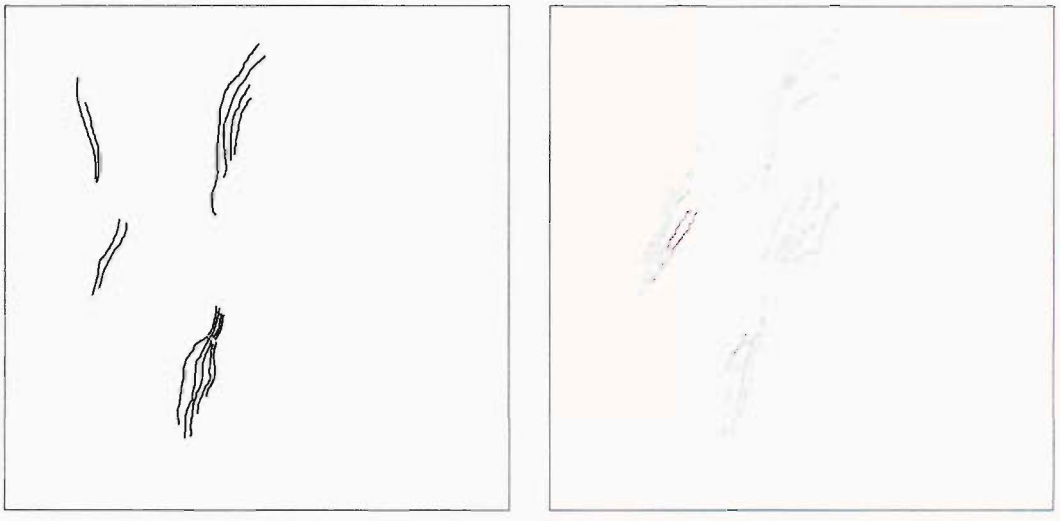

(a) Mask (b) Edges

Figure 7.11: edge selection for image A

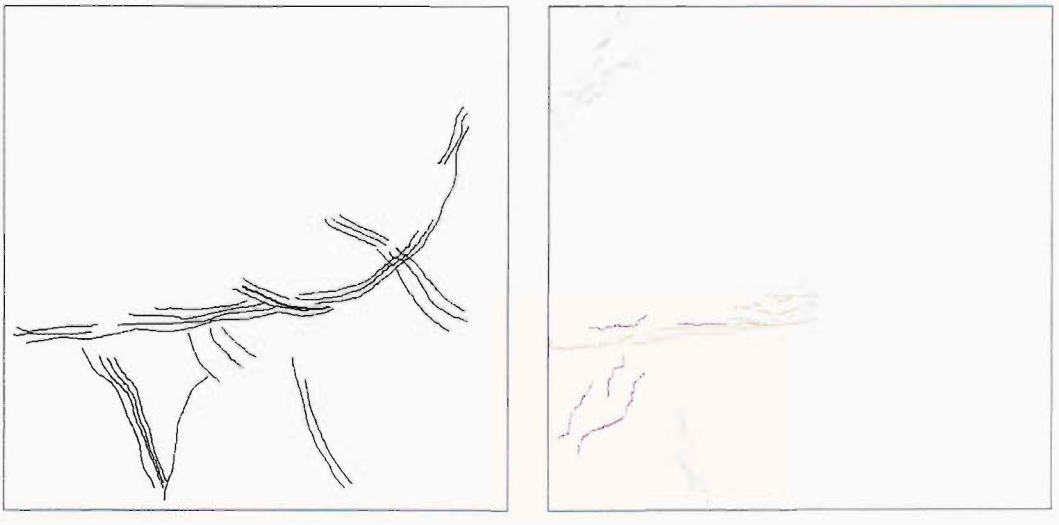

(a) Mask (b) Edges

Figure 7.12: Edge selection for image B

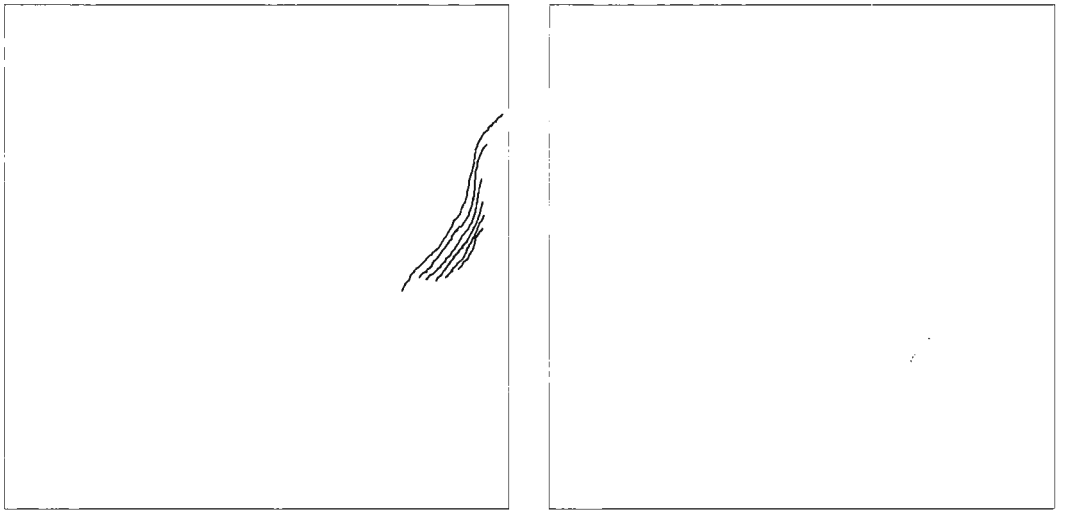

(a) Mask (b) Edges

Figure 7.13: Edge selection for image C

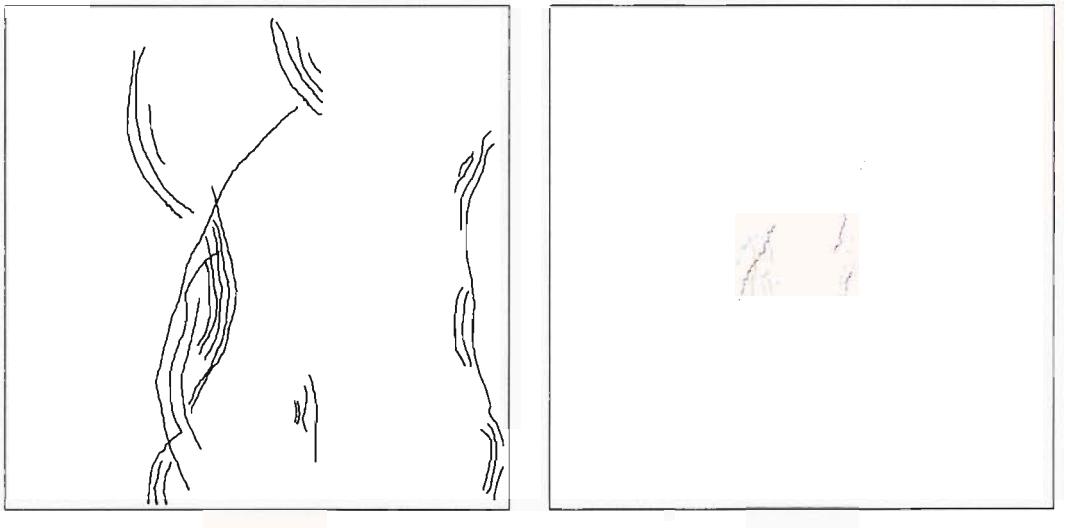

(a) Mask (b) Edges

Figure 7.14: Edge selection for image D

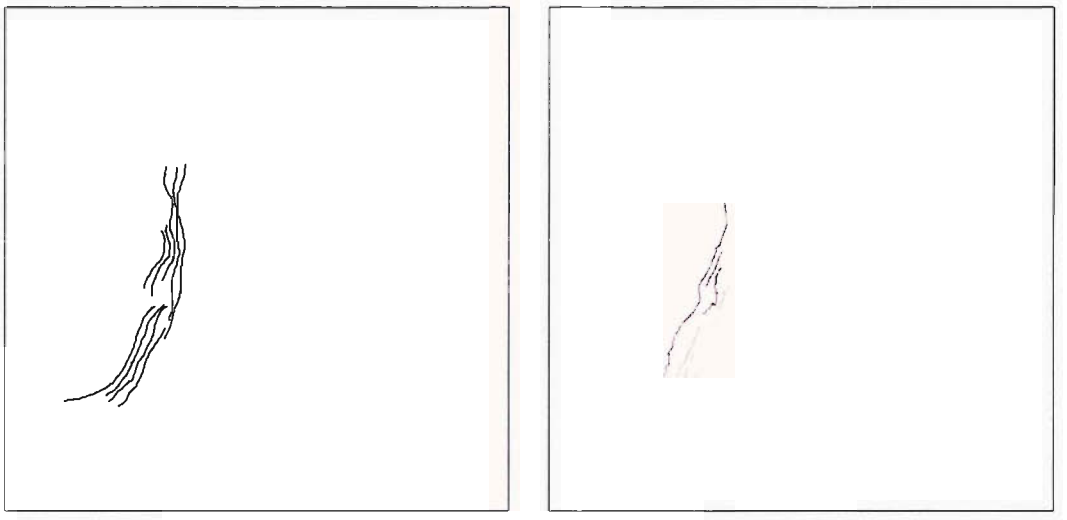

(a) Mask (b) Edges

Figure 7.15: Edge selection for image E

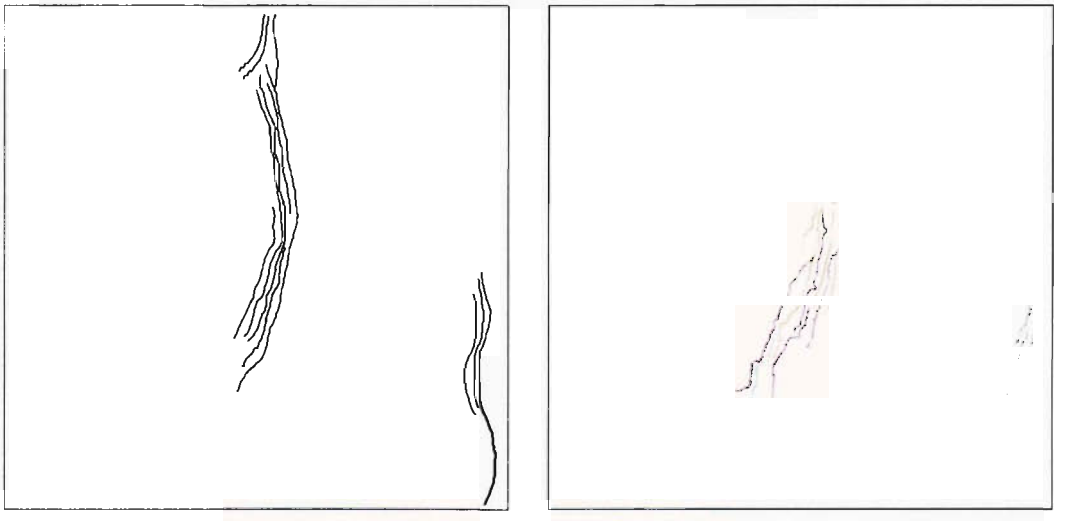

(a) Mask (b) Edges

Figure 7.16: Edge selection for image F

Determination of the direction and the wavelength

The edge detection technique allows a more detailed recognition of possible internal wave signatures. This method detects the presence of the internal wave by looking at the possible edges produced by the waves. Therefore it is possible, using the location and characteristics of this edge to derive primary information about the detected wave. The approach to this analysis was detailed in chapter 6. Two examples of the internal wave detected signature are shown.

Figure 7.17 and 7.19, show the position of the transect used for the determination of the wavelength of the wave packet for image A and E respectively. The wavelet power spectrum of these transect are illustrated in figure 7.18 and 7.20. The wave packet have respectively a wavelength of $2.49Km$ and $2.26Km$. But the study normalizes backscatter, so it is possible to identify type of processes responsible for the signature. In these two examples the mechanism is identical and identified as the hydrostatic interaction between the internal wave and the surface wave. The backscatter transect offers the possibility to measure the extent of the wave packet, which is the length of the section of the transect where the significant wavelength is represented in the wavelet spectrum. It is for these cases approximately equal to $16Km$ and $15Km$.

The knowledge of the edges that make up the internal wave signature can be used to determine the direction of the wave. This can be seen from figure 7.17 and 7.19 where an arrow represent the approximate direction of the wave calculated using the curvature of the edge.

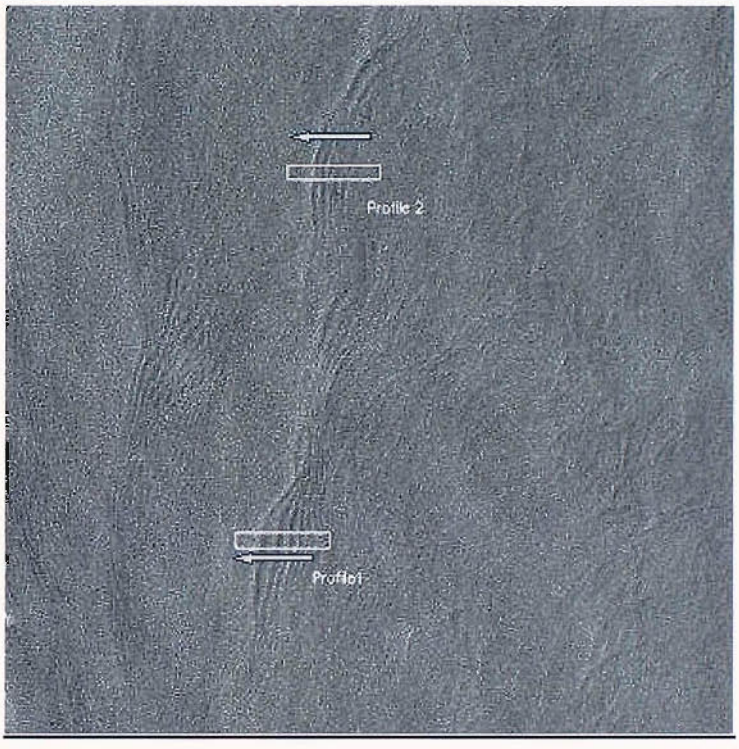

Figure 7.17: Profile and direction for image A

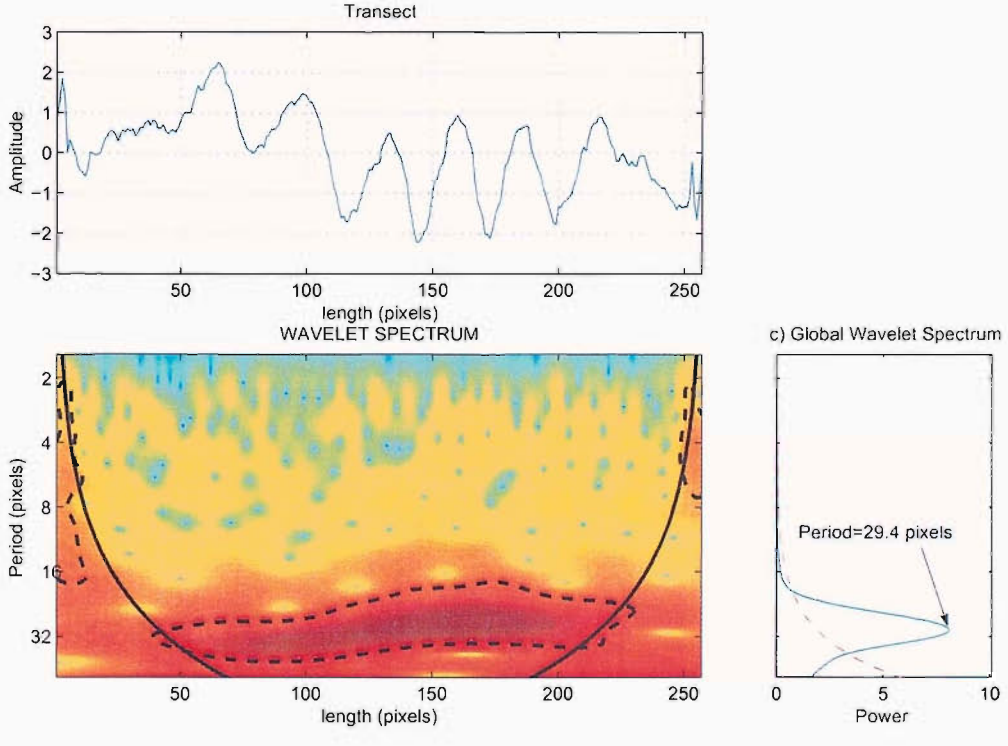

Figure 7.18: Spectrum using wavelet decomposition for the profile 1 of the image$A$. The dotted line represent the 95% level. Here the period is equal to 24.9 pixels which correspond a wavelength of $2.490Km$.The angle of propagation is equal to 178.6^o and 181.1^o

Figure 7.19: Profile and direction for image E

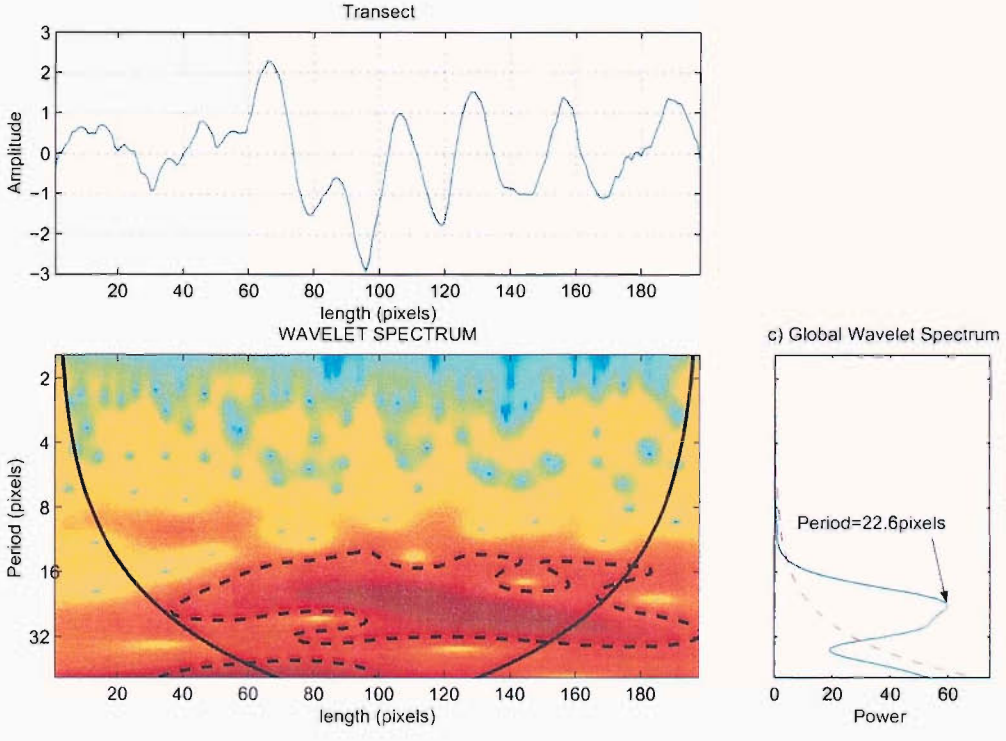

Figure 7.20: Spectrum using wavelet decomposition for the profile 1 of the image$E$. The dotted line represent the 95% level. Here the period is equal to 22.6 pixels which correspond a wavelength of $2.260Km$. The angle of propagation is equal to 321.3^o

7.3 Conclusion

In this chapter, six practical applications of the different classifications used have been described. The overall result offers a good representation of the success and failure of the different classification.

The classifications produce by the MLP are in general more accurate than the ones from the KNN. But the failure of the correct classification of image B and D have the same cause for both classifiers. These two images have complex features. These complex feature create two problems: it is difficult to produce a fair manual classification with a correct delimitation of the internal waves signature boundaries. The second problem is that both classifiers use a textural representation of the zone, and it is possible that this representation does not discriminate enough between event and non-event zone for such images.

The classification using the edge geometry produced the best results. This recognition scheme give a very high confidence level about the detect signature but the contrast between the internal signature and the background should be high enough to be able to trace the edges. This approach enables a mapping of the edge which allows an analysis of the wave packet. An analysis of the coherent length, wavelength, direction of propagation and type of signature inferred using the position of the edges has been made.

Chapter 8

Summary

8.1 Introduction

The importance of understanding and predicting internal waves for both the offshore engineering and the oceanographic sciences is not matched by our ability to correctly model such phenomena, primary because of a lack of information. The low number of processed satellite scenes does not offer enough information to improve dramatically our understanding and forecasting abilities. In response to these limitations, this research has focused on the development of an automatic detection and analysis scheme for internal wave signatures in SAR images. No automatic method for the recognition of oceanic features exists, therefore, the major novelty of the research lies in the automatic extraction and analysis of internal wave signature from SAR imagery. This new detection technique has the potential to reduce the cost and manpower required for the processing of satellite images for oceanographic purposes and provides an objective technique that will assist analysis and understanding of internal waves

The development of automatic methods to classify features within satellite imagery and to quantify their characteristics has relied on pattern recognition techniques. The difficulties in this problem were linked to the variant nature of the parameters of the signature produced by the wave in SAR imagery e.g. their length, orientation, strength, and local shape variation.To tackle these difficulties, two main approaches have been studied. A recognition technique based on texture has been developed in three parts: the segmentation, the characterization and the classification. The segmentation is produced using a multiscale edge detection, with a wavelet transform implemented filter. Statistical indices, derived from the GLCMs of the energy coefficient, offer a characterization relatively independent of target variation. The information contained in the GLCM and statistical indices are used to discriminate between two classes (event and

non-event), using a PCA technique, two different KNN classifiers and a MLP. The PCA classification technique used the GLCM directly, while the KNN and MLP classifiers are fed with statistical indices. The second approach is based on the edge geometry found in the images using a multiscale edge detection. This approach searches for internal wave signatures represented by at least three edges parallel to each other. Figure 8.1 shows the overall steps presented in this thesis.

The recognition techniques were applied to two SAR images (the image0 and image25). The image0 shows a strong well defined internal waves signature, with orientation along the diagonal of the scene. The image25 is the opposite, the signature of the 2 major internal waves present are weaker, and vertical with respect to the scene orientation. These two cases were chosen because they represent the two limits in the internal wave's signature range and provide a good test for the method proposed. Once each technique has been tuned, a series of unseen images are classified to offer quantitative accuracy of the different setups.

8.2 The Results

In the pre-processing section the issue about the strength and the orientation of the wave has been raised. A weak vertically or horizontally oriented wave is not detected with the same strength by the x and y decomposition. This discrimination shows up in the expression of the modulus event when corrections are applied. The left side internal wave signature present in image25 is a good example of such problem. As its detection is weak, its GLCM and the derived indices do not really show the signature. This cascading problem reduces the chance of a good classification.

The GLCM derived from the energy coefficient were calculated using different distances d. The statistical indices derived from these GLCM show that small values of d offer a better representation of the texture, independent of the decomposition scale and gray scale used.

In this work different recognition tools have been used. General trends in the classification for all the classification tools show that the shape and strength of the internal wave's signature is important. A strong and diagonally oriented signature is easily recognized over the background. However for vertically or horizontally orientated wave, which are weakly characterized by the GLCM and consequently by the statistical indices, the classification produced poor results.

Choice of the configuration and tuning:

PCA technique: The discrimination between classes was done by maximising the difference between the presence of internal waves (event) and the non-presence of internal waves (non-event). The results presented for each individual study show, the total accuracy in percent, the percentage of the misclassification of the non-event and the misclassification event. The accuracy offered by this classification is reasonable, but dependent on a particular threshold. The threshold needed to optimize the classification is very variable, which makes generalization of the technique difficult. In the presented results, the threshold was set at zero to offer comparative results, but in many cases this was not the best solution to perform the most accurate classification.
KNN technique: Two KNN techniques were first evaluated, a traditional KNN and a weighted KNN, using a range of values of k ($k = 2, 5, 7, 9$ and 11). The results presented for each individual cases show, the total accuracy, the percentage of the misclassification of the non-event and the misclassification event. The accuracy of the method is more reliable, as this method does not need any threshold, so it offers the chance to perform a generalization of the result. The weighted KNN has been chosen for its better performance than the normal KNN. After this initial choice the KNN was tuned to improve the configuration using a larger training set. The best configuration found was:

- Length of the input vector: 3
- Number of neighbours used: 3
- Best wavelet representation: mXY

MLP technique: The MLP in the study uses the same training set as the KNN. Evaluation procedures were designed to determine the different parameters, and the optimum architecture of the MLP, i.e. input node, layers and output node, as well as length of the training. The second important aspect of the construction of the MLP is the training. The best parameterisation found for the MLP is:

- Number of input nodes: 6
- Number hidden layer and nodes : $1 - 12$
- Number of output node: 1

- Best wavelet representation: XY

Edge analysis technique: The geometrical analysis uses a totally different concept. The goal is to identify which edges are parts of an internal wave signature and which are not. The starting point was to apply an edge tracing technique using a hysteresis threshold to the second level modulus of the wavelet decomposition. Then a series of tests on the curvature and direction of the edge were performed to eliminate some and join others. When only significant edges were remaining a procedure to determine their mutual parallelism was applied. The last step was to retain only edges, which were parallel with at least two other edges. From here it was then possible to extract information from the edge such as the direction and wavelength of the internal wave signature.

Application of the different techniques:

These approaches have been applied to different SAR images to illustrate its potential to generate accurate recognition. The classifications produce by the MLP are in general more accurate than the ones from the KNN. But the MLP like the KNN fails to give correct classification when complex features and/or busy background are present in the image.

The classification using the edge geometry produced the best results. This recognition scheme gives a very high confidence level about the detected signature but it requires the ratio between the internal signature and the background to be high enough to be able to trace the edges. This approach produced a mapping of the edge which allows an analysis of the wave packet. The demonstration of the wavelength, direction of propagation and type of signature inferred using the position of the edges have been made.

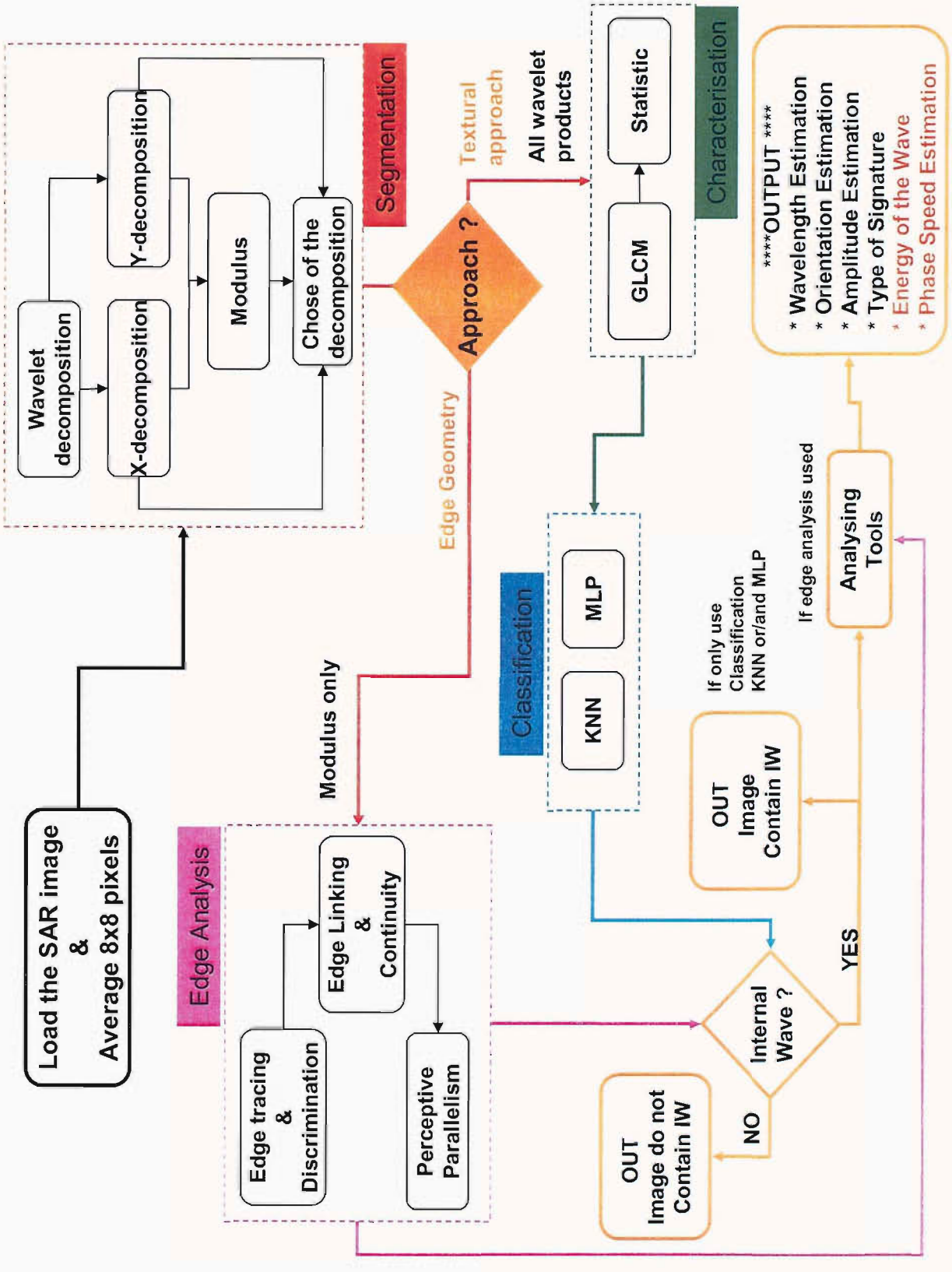

Figure 8.1: The different steps of this study. The red font text (*Energy of the wave* and *Phase speed estimation*) are potential characteristic which could be derived.

8.3 Future works

Results presented in this work have demonstrated that the combination of either textural analysis with classifier or edge geometry analysis can provide the recognition of internal wave signatures with a satisfactory accuracy. However a lot of ground needs to be covered before any operational recognition tool can be produced.

This work has laid the foundation towards a more accurate and operational system. One of the most obvious improvements will be to use both main approaches and combine them into a single system. Such a system will not be very different from the one proposed in this work. Instead of having an independent decision made from each of the approaches, a single test could be made incorporating the information from both approaches (Edge analysis and Texture classification). Another easy improvement can be made by having a larger and more representative training set. The extension of the training set could be made manually by adding other scenes. Information from the time of the year and the location of the scene to be classified can be used in order to select the relevant training set. One can construct a series of training sets with respect to period of the year or/and place. These different training set will be more representative of the internal waves present in the area as the similarity between internal waves from the same place is important. Another improvement would be to add further external information to the system such as wind, bathymetry, sea state, etc when available. In adding this information the system could recognize for example that in summer or late summer the likelihood of the formation of internal waves is much greater than in winter. For example the effect of the wind direction on the internal wave signature [7] can be introduced and hence improved the classification. In additional information could also increase the number of parameters inferred from the internal wave. By knowing the bathymetry it is possible to obtain an approximation of the mixed-layer depth [52].

Improvement can be made in a more fundamental manner, by a modifying of the approach. It has been shown that the edge analysis technique was a lot more reliable than the textural approach; therefore it seems logical to concentrate more effort on that technique. The approach used to find and infer the information of edges within the images is very simple (It was part of the attraction of the method), however in a very clustered image it has some limitations. A better system to trace and link edges could be developed in order to distinguish between real feature edges and artifacts due to a high sea state. Then each edge found could be used in an algorithm which will

calculate the wave propagation and therefore find the other edge. Such an approach could be implemented using either an active contour technique or an hopfield neural network. The active contour technique needs boundary conditions to be specified (zone of research, initial state) which could not be successfully stated. However this approach could be pursued by using an hopfield neural network as it shows potential in recognizing changes in features with time ([17] and [18]). This work begins the process of analysing the classified signature by demonstrating the retrieval of the orientation, wavelength, etc... It will be possible to used this information in an internal wave model using for example the KDV theory (Kroteweg-de Vries equation) [48] [5] [6] [61].

8.4 Conclusion

The importance and need for information about internal waves has been discussed in the introduction as well as at the start of this chapter. Despite its importance for both the oceanographic and engineering world, very few direct measurements are available and our understanding about their implications in the general ocean circulation is poor. This work was motivated by the requirement to offer an answer to the lack of information available about internal waves observed by satellite. It presents a new framework to classify very large numbers of SAR images in order to identify possible internal wave signatures and a means to infer primary information about the waves. The frame work is based on two approaches: a textural and edge parallelism analysis. It has been shown that both techniques can identify successfully the internal wave signature in SAR image. A greater success has been achieved using the edge parallelism technique. The determination of the type of signature and the wavelength of the internal wave has been demonstrated. Such a framework or an improved version could be used to create a global map of internal waves using archives from ERS 1-2 RadarSat and Envisat. Such a data set could be very useful for oceanographer and modellers alike in order to better understand and quantify the importance of the internal wave in the mixing needed to warm up and advect deep sea water to the surface. This database could also be of great use for the engineering community, for example in the design of offshore platforms and in the submarine communication.

The demand for internal wave information is so great that the European Space Agency (ESA) has recently renewed its interest about it (personal discussion with Gordon Campbell from ESA-ESRIN) and future projects are planned like a global internal

waves climatology for 2005 with the Office of Naval Research (ONR). This work will be a suitable candidate for such a project as part of a fully automatic system for internal wave analysis using remote sensing technology.

The major point of this research is that whilst there is plenty of imagery available, there are very few techniques that can automatically identify and categorise the internal waves. A unique combination of techniques described in this thesis including neural network, texture discrimination and the analysis of edges' geometry have been shown to have great potential to successfully identify and categorize internal waves.

Appendix A

Dyadic wavelet transform

The dyadic wavelet transform of $f \in L^2(\Re)$ is defined by equation(A.0.1) [41].

$$Wf(u, 2^j) = \int_{-\infty}^{+\infty} f(t) \frac{1}{\sqrt{2^j}} \times \psi\left(\frac{t-u}{2^j}\right) dt \tag{A.0.1}$$

A discrete diadic wavelet transform can be computed with a filter bank algorithm if the wavelet is approximately designed. The synthesis of these dyadic wavelets is similar to the construction of orthogonal wavelet bases.

Let h and g be a pair of finite impulse response filters. Set h as a low-pass filter with transfer function satisfying $\hat{h}(0) = \sqrt{2}$. A scaling function is construct with its Fourier transform describe in equation A.0.2

$$\begin{aligned} \hat{\phi}(w) &= \prod_{p=1}^{+\infty} \frac{\hat{h}(2^{-p}w)}{\sqrt{2}} \\ &= \frac{1}{\sqrt{2}} \hat{h}\left(\frac{w}{2}\right) \hat{\phi}\left(\frac{w}{2}\right) \end{aligned} \tag{A.0.2}$$

The corresponding wavelet ψ has a fourier transform defined by:

$$\hat{\psi}(w) = \frac{1}{\sqrt{2}} \hat{g}\left(\frac{w}{2}\right) \hat{\phi}\left(\frac{w}{2}\right) \tag{A.0.3}$$

As h and g have a finite number of non-zero coefficient, both ϕ and ψ have a compact support [41]. The number of vanishing moments of ψ is equal to the number of zeros of $\hat{\psi}(w)$ at $w = 0$. Since $\hat{\phi}(0) = 1$, (A.0.3) implies that is is also equal to the number of zeros of $\hat{g}(w)$ at $w = 0$.

A.1 Reconstruction Wavelets

Reconstruction wavelet are calculated with a pair of finite impulse response dual filter $\tilde{h}$ and $\tilde{g}$.

$$\begin{aligned}\hat{\tilde{\phi}}(w) &= \prod_{p=1}^{+\infty} \frac{\hat{\tilde{h}}(2^{-p}w)}{\sqrt{2}} \\ &= \frac{1}{\sqrt{2}} \hat{\tilde{h}}\left(\frac{w}{2}\right) \hat{\tilde{\phi}}\left(\frac{w}{2}\right)\end{aligned} \tag{A.1.1}$$

$$\hat{\tilde{\psi}}(w) = \frac{1}{\sqrt{2}} \hat{\tilde{g}}\left(\frac{w}{2}\right) \hat{\tilde{\phi}}\left(\frac{w}{2}\right) \tag{A.1.2}$$

A.2 Spline Dyadic Wavelet

A box spline of degree m is a translation of $m+1$ convolution of $1_{[0,1]}$ with itself. It is centered at $t = \frac{1}{2}$ if m is even and at $t = 0$ if m is odd. Its Fourier transform is:

$$\hat{\phi}(w) = e^{-i\frac{\epsilon w}{2}} \left(\frac{\sin\frac{w}{2}}{\frac{w}{2}}\right)^{m+1} \qquad \text{with} \qquad \epsilon = \begin{cases} 1 & \text{if } m \text{ is even} \\ 0 & \text{if } m \text{ is odd} \end{cases} \tag{A.2.1}$$

So

$$\hat{h}(w) = \sqrt{2}\frac{\phi(\hat{2}w)}{\phi(\hat{w})} = \sqrt{2} e^{-i\frac{\epsilon w}{2}} \left(\cos\frac{w}{2}\right)^{m+1} \tag{A.2.2}$$

One construct a wavelet that has one vanishing moment by choosing $\hat{g}(w) = O(w)$ inthe neighborhood of $w = 0$:

$$\hat{g}(w) = -i\sqrt{2} e^{-i\frac{\epsilon w}{2}} \sin\frac{w}{2} \tag{A.2.3}$$

The Fourier transform of the resulting wavelet is:

$$\begin{aligned}\hat{\psi}(w) &= \frac{1}{\sqrt{2}} \hat{g}\left(\frac{w}{2}\right) \hat{\phi}\left(\frac{w}{2}\right) \\ &= \frac{-iw}{4} e^{\frac{-iw-\epsilon}{4}} \left(\frac{\sin\frac{w}{4}}{\frac{w}{4}}\right)^{m+2}\end{aligned} \tag{A.2.4}$$

Figure A.1, shows the resulting quadratic splines ϕ and ψ. To design dual scaling function $\tilde{\phi}$ and wavelet $\tilde{\psi}$, one choose $\hat{\tilde{h}} = \hat{h}$. Consequently $\phi = \hat{\phi}$ and the reconstruction condition implies that:

$$\begin{aligned}\hat{\tilde{g}}(w) &= \frac{2 - \left|\hat{h}(w)\right|^2}{\hat{g}^*(w)} \\ &= -i\sqrt{2} e^{-i\frac{w}{2}} \sin\frac{w}{2} \sum_{n=0}^{m} \left(\cos\frac{w}{2}\right)^{2n}\end{aligned} \tag{A.2.5}$$

Figure A.2 gives the corresponding filter for m=2.

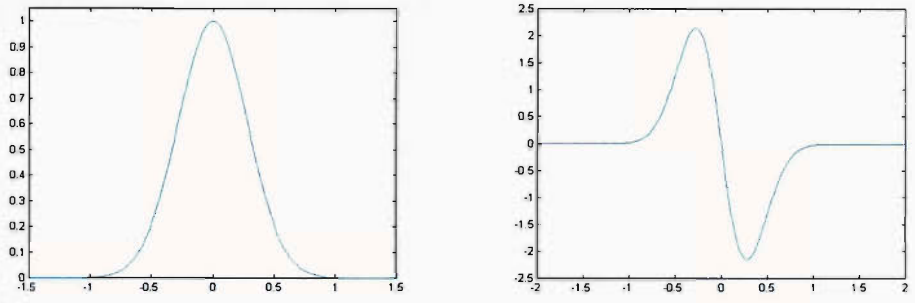

(a) θ (b) ψ

Figure A.1: Quadratic spline wavelet and scaling function

n	$h[n]/\sqrt{2}$	$\tilde{h}[n]/\sqrt{2}$	$g[n]/\sqrt{2}$	$\tilde{g}[n]/\sqrt{2}$
-2				-0.03125
-1	0.125	0.125		-0.6875
0	0.375	0.375	-0.5	-0.6875
1	0.375	0.375	0.5	0.6875
2	0.125	0.125		0.6875
3				0.03125

Figure A.2: Coefficients of the filter computed from their transform function (see Appendix A.1 for detail)

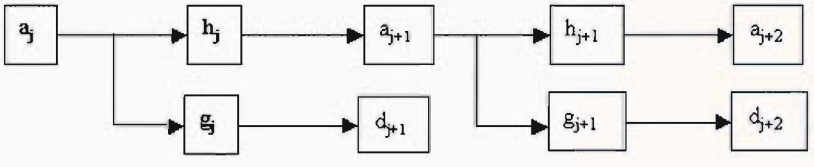

Figure A.3: Cascading convolution

A.3 "Algorithme à trous"

Suppose that the scaling function and the wavelets ϕ, ψ, $\tilde{\phi}$ and $\tilde{\psi}$ are designed with the filter h, g, $\tilde{h}$ and $\tilde{g}$. A fast dyadic wavelet transform is calculated with a filter bank called in French the *algorithme à trous*. It is similar to a fast biorthogonal wavelet transform, without subsampling. It is computed from a_o (initial image) by a cascading convolution for $0 \leq j < J$, as illustrated in figure A.3. It is similar to a fast biorthogonal wavelet transform, without subsampling [58].

Sample values of the original discrete image $a_0[n, m]$ are written as weighted averages of a function f with the kernel $\phi(x)\phi(y)$:

$$a_0[n, m] = \langle f(x, y), \phi(x - n)\phi(y - m) \rangle$$

For any $j \geq 0$, one denote:

$$a_j[n, m] = \langle f(x, y), \phi_{2^j}(x - n)\phi_{2^j}(y - m) \rangle$$

The discret wavelet coefficients are:

$$d_j^1 = W^1 f(n, m, 2^j) \quad , \quad d_j^2 = W^2 f(n, m, 2^j)$$

A separable filter is written:

$$xy[n, m] = x[n]y[m]$$

$\delta[n]$ denote the Dirac. A filter $k[n]$ is dilated to make the filter $k_j[n]$, by inserting $2^j - 1$ zeros (trous) between each sample. One can then prove that for any $j \geq 0$:

$$a_{j+1}[n, m] = a_j \star \bar{h}_j \bar{h}_j[n, m],$$

$$d_{j+1}^1[n, m] = a_j \star \bar{g}_j \delta[n, m],$$

$$d_{j+1}^2[n, m] = a_j \star \delta \bar{g}_j[n, m].$$

Appendix B

EigenGLCMs

Let the training set of GLCMs be $\Gamma_1, \Gamma_2, \Gamma_3, ..., \Gamma_M$. The average matrix of the set is defined by (B.0.1). Each GLCM differ from the average by the vector $\phi_i = \Gamma_i + \psi$. This set of very large vectors is then subject to PCA, which seek a set of M orthogonal vectors (u_n), which best describes the distribution of the data.

$$\psi = \frac{1}{M} \sum_{n=1}^{M} \Gamma_m \tag{B.0.1}$$

The K_{th} vector u_k is chosen in the way describe by (B.0.2) reach a maximum, subject to (B.0.3).

$$\lambda_r = \frac{1}{M} \sum_{n=1}^{M} \left(u_k^T \times \phi_n\right)^2 \tag{B.0.2}$$

$$u_l^T u_k = \begin{cases} 1 & \text{if } l = k \\ 0 & \text{if otherwise} \end{cases} \tag{B.0.3}$$

The vector u_k and the scalar λ_k are eigenvectors and eigenvalues of the covariance matrix defined by (B.0.4). Where the matrix $A = [\phi_1, \phi_2, .., \phi_M]$. The matrix C is very large (NxN). To determine its eigenvectors and eigenvalues is an intractable task; We need dimensionality simplification.

$$\begin{aligned} C &= \frac{1}{M} \sum_{n=1}^{M} \phi_n \phi_n^T \\ &= AA^T \end{aligned} \tag{B.0.4}$$

If the number of data points in the matrix space is less than the dimension of space (ie: $M < N^2$), there will be only $M - 1$ meaningful eigenvectors, rather than N^2. The N^2 is solved by first solving the eigenvectors of an MxM matrix, and then taking

approximate linear combination of the matrix ϕ_i. Consider the eigenvectors V_i of AA^T (B.0.5). From which we see that AV_i are the eigenvectors of $A^TA = C$.

$$A^TAV_i = u_iV_i \tag{B.0.5}$$

Multiplying both side by A:

$$AA^TAV_i = Au_iV_i$$

We construct the MxM matrix $L = A^TA$, where $L_{m,n} = \phi_n\phi_n^T$, and find M eigenvectors, V_i and L. These vectors determine a linear combination of the M training set GLCMs to form the eigenGLCMs u_i (B.0.6).

$$u_i = \sum_{n=1}^{M} V_{l,k}\phi_k \qquad l = 1, 2, ..., M \tag{B.0.6}$$

Appendix C

Confusion matrix

Image A				Image B				Image C			
MLP		KNN		MLP		KNN		MLP		KNN	
152	36	**153**	35	**137**	47	**145**	39	**162**	42	**160**	44
5	**32**	8	**29**	8	**33**	13	**28**	0	**21**	0	**21**

Image D				Image E				Image F			
MLP		KNN		MLP		MLP		KNN		MLP	
137	46	**131**	**137**	46	**131**	**137**	46	**131**	**137**	46	**131**
9	**34**	11	9	**34**	11	9	**34**	11	9	**34**	11

The colour code of the confusion matrix corresponds is as follow:

None-event correctly classified
None-event misclassified
Event correctly classified
Event misclassified

Figure C.1: Confusion matrix used to derived the values in table 7.3

Bibliography

[1] W. Alpers, *Theory of radar imaging of internal waves*, Nature **314** (1985), 245–247.

[2] J.R Apel, *Principles of ocean physics*, Academic press, 1999.

[3] J.R. Apel, H.M. Byrne, J.R Proni, and R. Seller, *A study of oceanic internal waves using satellite imagery and ship data*, Remote Sensing of Environment **5** (1976), 125–135.

[4] J.R. Apel, R.F. Gasparovic, D.R. Thompson, and B.L. Gotwols, *Signatures of surface wave/internal wave interactions: experiment and theory*, Dynamics of Atmospheres and Oceans **12** (1988), 89–106.

[5] J.R. Apel and J.I. Gonzalez, *Nonlinear features of internal waves off* Baja California *as observed from the* SEASAT *imaging radar*, Journal Geophysical Research **88** (1983), no. C7, 4459–4466.

[6] J.R. Apel, D.R. Thompson, D.G. Tilley, and P.V. Dyke, *Hydrodynamics and radar signatures of internal solitons in the* Andaman Sea, John Hopkins APL Technical Digest **6** (1986), no. 4, 330–337.

[7] I.B. Araujo, J.C.B. Da Silva, S.A. Ermakov, and I.S. Robinson, *On the role of wind direction in* ERS SAR *signatures of internal waves on the* Iberian shelf, Global Atmosphere and Ocean Systems **8** (2002), no. 4, 269–281.

[8] R.L. Bankert, *Cloud classification of* AVHRR *imagery in maritime regions using a probabilistic neural network*, Journal of Applied Meteorology **33** (1994), 909–918.

[9] D.G. Barber, T.N. Papakyriakou, and E.F. LeDrew., *On the relationship between energy fluxes, dielectric properties, and microwave scattering over snow covered first-year sea ice during the spring transition period*, Journal of Geophysical Research **99** (1994), no. C11, 22401–22411.

[10] J.A Benediktson, P.H Swain, and O.K. Esrouy, *Conjugate-gradient neural network in classification of multisource and very-high-dimensional remote sensing data.*, International Journal of Remote Sensing **14** (1993), 2883–2903.

[11] C.M. Bishop, *Neural networks for pattern recognition*, Oxford: Clarendon Press, 1995.

[12] P. Blondel, *Segmentation of the* Mid-Atlantic Ridge *south of the* Azores, *based on acoustic classification of* TOBI *data*, Tectonic, Magmatic, Hydrothermal and Biological Segmentation of Mid-Ocean Ridge **118** (1996), 17–28, London: Geophysical Society.

[13] J. Canny, *A computational approach to edge detection*, IEEE Transactions on Pattern Analysis and Machine Intelligence **8** (1986), 679–698.

[14] Chen and D.W. Tsay, *Neural classification of* SPOT *imagery through integration of intensity and fractal information*, International Journal of Remote Sensing **18** (1997), 763–783.

[15] L. D. Cohen, *On active contour models and balloons*, Compute Vision, Graphics and Images Processing: Images Understanding **53** (1991), no. 2, 211–218.

[16] L. F. Costa and R. M. Cesar, *Shape analysis and classification: Theory and practice*, CRC press, 2001.

[17] S. Cote and A.R.L. Tatnall, *A neural network-based method for tracking features from satellite sensor images*, International Journal of Remote Sensing **16** (1995), 3695–3701.

[18] ———, *The hopfield neural network as a tool for feature tracking and recognition from satellite sensor images*, International Journal of Remote Sensing **30** (1997), 871–885.

[19] J.C. Da Silva, S.A. Ermakov, and I.S. Robinson, *Role of surface films in* ERS SAR *signatures of internal waves on the shelf. 1. short-period internal waves*, Journal of Geophysical Research **103** (1998), no. C4, 8009–8031.

[20] ———, *Role of surface films in* ERS SAR *signatures of internal waves on the shelf. 3. mode transition*, Journal of Geophysical Research **105** (2000), no. C10, 24089–24104.

[21] C. Daul, P. Graebling, and E. Hirsch, *From the Hough transform to a new approach for the detection and approximation of elliptical arcs*, Computer vision and Image Understanding **72** (1998), no. 3, 215–236.

[22] J.E Dayhoff, *Neural networks architecture*, New York: Van Nostrand Reinhold, 1990.

[23] S.T. Dokken, *Identification and characterization of internal waves in SAR images along the coast of Norway*, Geophysical Research Letters **28** (2001), no. 14, 2803–2806.

[24] A.N. Esgiar, B.S. Sharif, R.N.G. Naguib, M.K. Bennett, and A. Murray, *Texture descriptions and classification for pathological analysis of cancerous colonic mucosa*, IEEE Proc. Int. Conf. on Image Processing and its Applications **1** (1999), 335–338.

[25] G.M. Foody and M.K. Arora, *An evolution of some factor affecting the accuracy of classification by an artificial neural network*, International Journal of Remote Sensing **18** (1997), 799–810.

[26] L.L. Fu and B. Holt, *Internal waves in the Gulf of California: Observations from a spaceborne radar*, Journal of Geophysical Research - Oceans **89** (1984), no. C2, 2053–2060.

[27] A. Ganachaud and C. Wunsch, *Improved estimates of global ocean circulation, heat transport and mixing from hydrographic data*, Nature **408** (2000), 453–456.

[28] R.M. Haralick, *On a texture-context features extraction algorithm for remotely sensed imagery*, Proceedings of the IEEE Computer Society Conference on Decision and Control (Gainesville, FL) (1971), 650–657.

[29] R.M. Haralick, K. Shanmugam, and Its'hak Dinsten, *Texture features for image classification*, IEEE Transactions on Systems, Man, and Cybernetics **3** (1973), no. 6, 610–621.

[30] R. Hecht-Nelson, *Kolmogorov's mapping neural network experience theorem*, IEEE first International conference on Neural Network, San Diago, III-11 III-14 (1987).

[31] J. Illingworth and J. Kittler, *A survey of the Hough transform*, Computer Vision, Graphics and Images Processing **44** (1988), 87–116.

[32] H.S Ip and W.H. Wong, *Detecting perceptually parallel curves: Criteria and force-driven optimization*, Computer Vision and Image Understanding **68** (1996), 190–208.

[33] D.R.G. Jeans and T.J. Sherwin, *The variability of strongly non-linear solitary internal waves observed during an upwelling season on the* Portuguese *shelf*, Continental Shelf Research **21** (2001), 18551878.

[34] B. Julesz, *Visual pattern discrimination*, IEEE Transactions on Information Theory **8** (1962), no. 2, 84–92.

[35] C.W. Kang, *Extraction of straight line segment using rotation transform: Generalized* Hough *transform*, Pattern Recognition **24** (1991), no. 7, 633.

[36] H. Laur, P.Bally, and P. Meadows, ERS SAR *calibration - derivation of the backscatter coefficient in* ESA ERS SAR *pri products*, ESA Documentation ES-TN-RS-PM-HL09 Issues 2 Rev. 5b.

[37] J. Lee, S.K. Sengupta R.C. Weger, and R.M. Welch, *A neural network approach to cloud classification*, IEEE Transactions on Geoscience and Remote Sensing **28** (1990), 846–855.

[38] A.K. Liu, C.Y. Peng, and S.Y.S. Chang, *Wavelet analysis of satellite images for coastal watch*, IEEE Transactions on Geoscience and Remote Sensing **22** (1997), no. 1, 9–17.

[39] M. Makynen and M. Hallikainen, *C-band backscattering signatures of* Baltic *sea ice*, Proceeding of the IGARSS98 (1998), 983985.

[40] S. Mallat, *A theory for multiresolution signal decomposition: The wavelet representation*, IEEE Transactions on Pattern Analysis and Machine Intelligence **7** (1989), 674–693.

[41] S. Mallat, *A tour of signal processing*, Academic Press, 1999.

[42] S. Manabe and R.J. Stouffer, *Two stable equilibria of a coupled ocean-atmosphere model*, Journal of Climate **1** (1988), 841–866.

[43] R. Mohan and R. Nevatia, *Perceptual organization for scene segmentation and description*, IEEE Transactions on Pattern Analysis and Machine Intelligence **14** (1992), 616–635.

[44] W. Monk and C. Wunsch, *Abyssal recipes* II*: energetics of tidal and wind mixing*, Deep-Sea Research I **45** (1998), 1976–2009.

[45] A. Niedermeier, E. Romaneeßen, and S. Lehner, *Detection of coastlines in sar images using wavelet methods*, IEEE Transaction on Geoscience and Remote Sensing **38, number** = (2000).

[46] M. Nixon and A. Aguardo, *Feature extraction and image processing*, Newnes, 2002.

[47] A.R. Osborne and TI Burch, *Internal solitons in the* Andaman Sea, Science **208** (1980), no. 4443, 451–460.

[48] L.A. Ostrovsky, *How to describe strong internal waves in coastal areas*, IOS/WHOI/ONR Internal Solitary Wave Workshop - Victoria, B.C., Canada (October 27-29, 1998).

[49] G.S Pankiewicz, *Neural network classification of convective air masses for a flood forecasting system*, International Journal of Remote Sensing **18** (1997), 887–898.

[50] J.D Paolo and R.A Schowengerdt, *A review and analysis of backpropagation neural networks for classification of remotely sensed multispectral imagery*, International Journal of Remote Sensing **16** (1995), 3033–3038.

[51] O.M. Phillips, *The dynamics of the upper ocean - 2nd edition*, Cambridge University Press, 1977.

[52] D.L. Porter and DR Thompson, *Continental shelf parameters inferred from* SAR *internal wave observations*, Journal of Atmospheric and Oceanic Technology **16** (1999), 475–487.

[53] T. Ranchin and L. Wald, *The wavelet transform for the analysis of remotely sensed images*, International Journal of Remote Sensing **14** (1993), no. 3, 615–619.

[54] I.S. Robinson, *Satellite oceanography: an introduction for oceanographers and remote-sensing scientist*, John Wiley and Sons, 1994.

[55] J.A. Rodenas and R. Garello, *Wavelet analysis in* SAR *ocean image profiles for internal wave detection and wavelength estimation*, IEEE Transactions on Geoscience and Remote Sensing **35** (1997), 933–345.

[56] J.A Rodenas and R. Garello, *Internal wave detection and location in* SAR *images using wavelet transform*, IEEE Transactions on Geoscience and Remote Sensing **36** (1998), 1494–1507.

[57] D.E Rumelhart, G. E. Hinton, and R.J. Williams, *Learning internal representation by error propagation: Parallel-distributed processing. exploration in the microstructures of recognition*, D.E. Rumelhart and J.L. McLellend - Cambridge, MA:MIT press - Vol 1, 318-362, 1990.

[58] M.J. Shensa, *The discrete wavelet transform: Wedding the á trous and mallat algorithms*, IEEE Transactions on Signal Processing **40** (1992), no. 10, 2464–2482.

[59] M.E. Shokr, *Evaluation of second-order texture parameters for sea ice classification from radar images*, Journal of Geophysical Research **96** (1991), no. C6, 10,625–10,640.

[60] K.K. Simhadri, S.S. Iyengar, R.J. Holyer, M. Lybanon, and J.M. Zachary, *Wavelet-based feature extraction from oceanographic images*, IEEE Transactions on Geoscience and Remote Sensing **36** (1998), no. 3, 767–777.

[61] J. Small, Z. Hallock, G. Pvey, and J.C. Scott, *Observations of large amplitude internal waves at the* Malin *shelf edge during* SESAME *1995*, Continental Shelf Research **19** (1999), no. 11, 1389–1436.

[62] F. Talu and Y. Tatar, *A new edge tracing method developed for object recognition*, IJCI Proceedings of Intl. XII. Turkish Symposium on Artificial Intelligence and Neural Networks **1** (2003), no. 1, 280–282.

[63] S. Theodorodis and K. Koutroumbas, *Pattern recognition*, Academic Press, 1999.

[64] M. Tomczak, *http://www.es.flinders.edu.au/~mattom/introoc/newstart.html*, (2000).

[65] V.R. Tovinkere, M. Penaloza, A. Logar, A. Lee, R.C Weger, T.A Berendes, and R.M Welch, *An intercomparison of artificial-intelligence approaches for polar scene identification*, Journal of Geophysical Research **98** (1993), no. D3, 5001–5016.

[66] M. Unser, *Sum and difference histograms for texture classification*, IEEE Transactions on Pattern Analysis and Machine Intelligence **8** (1986), 118–125.

[67] D.J. Williams and M. Shah, *A fast algorithm for active contours and curvature estimation*, Computer Vision, Graphics, Image Processing **55** (1992), 14–26.

[68] J.M. Wrigth, *Detection of ocean waves by microwave radar; the modulation of short gravity-capillary waves*, Boundary Layer Meteorology **13** (1978), 87–105.

[69] C. Xu and L. Prince, *Snakes, shapes, and gradient vector flow*, IEEE Transaction on Image Processing **7** (1998), 359–370.